The Dissertation Committee for Matthew William Anderson
certifies that this is the approved version of the following dissertation:

Constrained Evolution in Numerical Relativity

Committee:

_____

Richard Matzner, Supervisor

_____

Philip Morrison

_____

Austin Gleeson

_____

Lawrence Shepley

_____

Paul Shapiro

Constrained Evolution in Numerical Relativity

by

Matthew William Anderson, B.S.

Dissertation

Presented to the Faculty of the Graduate School of

The University of Texas at Austin

in Partial Fulfillment

of the Requirements

for the Degree of

Doctor of Philosophy

The University of Texas at Austin

August 2004

Acknowledgments

MATTHEW WILLIAM ANDERSON

The University of Texas at Austin

August 2004

Constrained Evolution in Numerical Relativity

Publication No. _____

Matthew William Anderson, Ph.D.

The University of Texas at Austin, 2004

Supervisor: Richard Matzner

The strongest potential source of gravitational radiation for current and future detectors is the merger of binary black holes. Full numerical simulation of such mergers can provide realistic signal predictions and enhance the probability of detection. Numerical simulation of the Einstein equations, however, is fraught with difficulty. Stability even in static test cases of single black holes has proven elusive. Common to unstable simulations is the growth of constraint violations. This work examines the effect of controlling the growth of constraint violations by solving the constraints periodically during a simulation, an approach called *constrained evolution*.

The effects of constrained evolution are contrasted with the results of *unconstrained evolution*, evolution where the constraints are not solved during the course of a simulation. Two different formulations of the Einstein equations are examined: the standard ADM formulation and the generalized Frittelli-Reula formulation. In most cases constrained evolution vastly improves the stability of a simulation at minimal computational cost when compared with unconstrained evolution. However, in the more demanding test cases examined, constrained evolution fails to

produce simulations with long-term stability in spite of producing improvements in simulation lifetime when compared with unconstrained evolution.

Constrained evolution is also examined in conjunction with a wide variety of promising numerical techniques, including mesh refinement and overlapping Cartesian and spherical computational grids. Constrained evolution in boosted black hole spacetimes is investigated using overlapping grids. Constrained evolution proves to be central to the host of innovations required in carrying out such intensive simulations.

Table of Contents

List of Tables

List of Figures

xvii

Chapter 1

Introduction

Major experimental initiatives currently underway to further test Einstein's theory of relativity have opened the prospect of directly observing for the first time the gravitational radiation from astrophysical sources such as binary black hole and neutron star mergers. These experimental initiatives include the LIGO detectors in the United States, the VIRGO detector in Italy, the TAMA detector in Japan, and GEO 600 detector in Germany, among others. Realistic signal prediction via numerical simulation of the Einstein equations enhances the probability of detection in these instruments and provides insight into the dynamics of strong field sources of gravity.

Numerical simulation of the Einstein equations, however, has proven to be very difficult. For successful gravitational wave extraction in a data set, the simulation must be stable for very long times and have computational domains large enough to include the radiation zone. Most full simulations fail in both of these criteria. While available computational resources consistently improve, stability problems in solving the Einstein equations continue to plague even the simplest static test problems.

The Einstein equations consist of coupled hyperbolic-elliptic partial differ-

ential equations. The elliptic equations are constraints on the initial data which analytically remain statisfied under the action of the dynamical equations. But this is not the case numerically. Unstable simulations generally experience a growth of constraint violations prior to losing convergence and going unstable. Controlling these constraint violations during evolutions of black hole spacetimes is the focus of this work.

The numerical simulation of black hole spacetimes will be examined solely. Two different formulations of the Einstein equations are employed in the various simulations for comparison: the standard Arnowitt-Deser-Misner (ADM) formulation and the generalized Frittelli-Reula formulation. These are introduced in chapter 2. Minor modifications of the ADM equations, accomplished by subtracting constraint terms from the evolution equations, are also presented. They are introduced in chapter 5. Chapter 3 presents the background necessary for solving the constraint equations. The myriad numerical methods used in this work are introduced in chapter 4.

Results from numerical simulations dominate all chapters after chapter 4. Two different approaches towards the constraint equations are examined: unconstrained evolution, where the constraint violations that appear during a simulation are merely monitored; and constrained evolution, where the constraint violations are actively controlled via periodic elliptic solves. Chapter 5 is devoted to unconstrained evolution, while chapter 6 addresses constrained evolution. Constrained evolution reappears in each subsequent chapter as other numerical techniques are investigated: mesh refinement in chapter 7 and overlapping grids in chapter 8.

While the vast majority of results presented only examine static, nonrotating black holes, boosted single black hole spacetimes using overlapping grids are presented in chapter 8.

The conventions and notations used are summarized here:

- Geometric units: $G = 1$, $c = 1$.

- Metric signature $(-, +, +, +)$.

- Greek indices $(\alpha, \beta, \gamma, \cdots)$ range over 0,1,2,3.

- Latin indices $(i, j, k, \cdots)$ range over 1,2,3.

- Bold face symbol: a tensor, e.g. $\mathbf{G}$.

- Lorentz transformation matrix: $\Lambda_\beta{}^\alpha$.

- Symmetrization operator: ( ) e.g. $V_{(ij)} = \frac{1}{2!}\left(V_{ij} + V_{ji}\right)$.

- Covariant derivative operator: ∇. Also used in standard physics equations, e.g. curl, Laplacian, divergence.

- Lie derivative: $\pounds$.

Chapter 2

Background

Gravity, as described by the Einstein equations, constitutes an ideal candidate for numerical simulation. Brute force computation cuts the Gordian knot of unyielding equations and provides solutions to otherwise intractable problems. Setting up the Einstein equations as a Cauchy problem is fundamental to solving the system through numerical simulation. This chapter reviews the fundamental ideas of the $3+1$ decomposition of the Einstein equations and introduces constrained evolution as a strategy for numerical work. The standard ADM formulation of the Einstein equations is presented first, followed by a brief discussion of issues regarding the well-posedness of the ADM equations. The generalized Frittelli-Reula formulation of the Einstein equations is then presented. Kerr-Schild coordinates are subsequently introduced along with a brief discussion of their utility. Finally, measure definitions helpful to numerical work in quantifying error are introduced.

2.1 The Einstein Equations

Gravity in the Newtonian limit is represented by a potential which satisfies

$$\nabla^2 \phi = 4\pi\rho, \tag{2.1}$$

where ϕ is the gravitational potential, and ρ is the mass density. The potential generates an acceleration, $\tilde{\mathbf{g}}$,

$$\tilde{\mathbf{g}} = -\nabla\phi. \tag{2.2}$$

This description has proven to be extremely successful in describing systems with velocities small compared to that of light and with weak gravitational fields. But there are some immediately evident problems: it is not invariant under a Lorentz transformation; gravity propagates infinitely fast in this description.

A simple generalization of the Newtonian potential to correct this problem is accomplished by replacing the ∇^2 operator with the Lorentz invariant d'Alembertian operator:

$$\Box\phi = 4\pi\rho_0 \tag{2.3}$$
$$\Box = -\frac{\partial^2}{\partial t^2} + \nabla^2, \tag{2.4}$$

where ρ_0 is now the rest mass density of the system. This description of gravity is Lorentz invariant, but the gravitational acceleration is determined by the rest mass density of the system, violating the observed equivalence between gravitational and inertial mass.

Abandoning scalar gravity for a tensorial description of gravity defined on a differential manifold provides the solution to these problems. The gravitational potential, ϕ is replaced by ten independent components of the metric tensor, $\mathbf{g}$, which describe gravity as curvature in spacetime. The new gravitational potential is the metric tensor.

The Einstein equations relate tensors involving second derivatives of the metric tensor to the energy-momentum tensor:

$$\mathbf{G} = 8\pi\mathbf{T}, \tag{2.5}$$

5

where **G** is the Einstein tensor and **T** is the energy-momentum tensor. The energy-momentum tensor describes the matter distribution of a system and is the generalization of the ρ term in Newtonian gravity. The vacuum Einstein equations,

$$\mathbf{G} = \mathbf{0} \tag{2.6}$$

are the equations appropriate to black hole physics and are treated exclusively in this dissertation.

The Einstein tensor is a symmetric tensor defined in terms of the 4-D Ricci tensor $R_{\mu\nu}$, the metric tensor $g_{\mu\nu}$, and the Ricci scalar R:

$$G_{\mu\nu} = R_{\mu\nu} - \frac{1}{2}g_{\mu\nu}R, \tag{2.7}$$

where μ, ν run from $0 \dots 3$. The Ricci tensor is formed from the Riemann-Christoffel tensor, $R_{\lambda\mu\nu\kappa}$:

$$R_{\mu\nu} = g^{\eta\sigma} R_{\sigma\mu\eta\nu}. \tag{2.8}$$

To reduce the computational complexity involved in evaluating the 3-D Riemann-Christoffel tensor, the following form is used which does not require any derivatives of the Christoffel symbols, Γ^i_{jk} [1]:

$$
R_{ijkl} = \frac{1}{2}\left[\frac{\partial^2 g_{ik}}{\partial x^l \partial x^j} - \frac{\partial^2 g_{jk}}{\partial x^l \partial x^i} - \frac{\partial^2 g_{il}}{\partial x^k \partial x^j} + \frac{\partial^2 g_{jl}}{\partial x^k \partial x^i}\right] \\
+ g_{mn}\left[\Gamma^m_{ki}\Gamma^n_{jl} - \Gamma^m_{li}\Gamma^n_{jk}\right], \tag{2.9}
$$

where i,j,k,l,m,n run from $1 \dots 3$.

The Riemann-Christoffel tensor has differential symmetries called the Bianchi identities,

$$R_{\alpha\delta\beta\gamma;\nu} + R_{\alpha\delta\nu\beta;\gamma} + R_{\alpha\delta\gamma\nu;\beta} = 0, \tag{2.10}$$

which imply that the Einstein tensor has vanishing divergence

$$G^\mu{}_{\nu;\mu} = 0. \tag{2.11}$$

Four of the Einstein equations (Eq. 2.6) consist of constraint equations, expressed here without source terms,

$$G_{0\mu} = 0. \tag{2.12}$$

The remaining six relations

$$G_{ij} = 0 \tag{2.13}$$

are evolution equations. Analytically, under the action of the evolution equations the constraint equations remain satisfied.

There is an analogue of this in the Maxwell equations [2][3]. The constraints

$$\nabla \cdot \mathbf{E} = 0 \tag{2.14}$$

$$\nabla \cdot \mathbf{B} = 0 \tag{2.15}$$

are analytically maintained under the action of the source-free evolution equations

$$\dot{\mathbf{B}} = -\nabla \times \mathbf{E} \tag{2.16}$$

$$\dot{\mathbf{E}} = \nabla \times \mathbf{B}. \tag{2.17}$$

The Einstein equations form a constrained hyperbolic system. Numerical solution of the Einstein equations usually consists of solving the constraint equations initially for a particular data set, then evolving that data set while monitoring the constraint violations during evolution. Such an approach is called *unconstrained evolution* and comprises the vast majority of all simulations solving the Einstein equations. There is a drawback to this approach, however. Unconstrained evolutions are particularly susceptible to constraint violating modes which can cause a simulation to go unstable. Such modes would not arise with infinitely accurate evolution schemes, but round-off and truncation errors are inherent to numerical work. Constraint violations are certain to appear during the course of an evolution as a result of these errors.

Extensive efforts have been made to control the growth of constraint violations during numerical simulation. In magnetohydrodynamics, the Evans-Hawley constrained transport method ensures that the constraints in electromagnetism are satisfied to machine precision in numerical simulation by placing vector and scalar quantities at staggered locations on a computational grid [4]. However, unlike the situation in electromagnetism, where a discrete simplectic calculus can be written which assures conservation of a discretized version of the constraints, there appears to be no equivalent formulation for general relativity that conserves discretized versions of the gravitational constraints[5].

Growing constraint violations suggest re-solving the constraint equations during an evolution. This approach is called *constrained evolution*. Constrained evolution is not specific to any particular choice of coordinates or formulation of the Einstein equations. It is a general method which can control the growth of the constraint violations arising from round-off and truncation errors during a simulation. Solving the full Einstein equations, both evolution and constraint, aims to solve one of the major stability problems in evolving black hole spacetimes.

2.2   The Initial Value Problem and ADM

The initial value problem is crucial to numerical simulation of strong field gravitational sources using general relativity. The initial value problem seeks to construct the metric tensor for all future time using a supplied initial metric tensor and its first time derivatives. The simulations presented in this thesis follow the $3+1$ approach to this problem. In the $3+1$ approach, spacetime is decomposed into a series of space-like hypersurfaces, or slices, defined at each instant of time. Specifying the metric tensor and its first time derivatives on a space-like hypersurface enables the calculation of all derivatives of the space-space components, $g_{ij,\mu}$, via some numerical approximation. Solving the Einstein equations then consists of evolving the spatial

components of the metric tensor, g_{ij}, by constructing future slices from current and past slices.

Several formulations of the Einstein equations exist which evolve spacelike 3-surfaces in time. The simplest and most commonly used formulation historically is that developed by Arnowitt, Deser, and Misner (ADM) [6]. The standard ADM $3 + 1$ form of the spacetime metric is:

$$ds^2 = -\alpha^2 dt^2 + g_{ij}(dx^i + \beta^i dt)(dx^j + \beta^j dt). \qquad (2.18)$$

To arrive at this, the general 4-metric is split into spatial and temporal parts:

$$g_{\mu\nu} = \left[\begin{array}{c|c} g_{00} & g_{0i} \\ \hline & \\ g_{i0} & g_{ij} \end{array} \right], \qquad (2.19)$$

where the purely spatial part of the 4-metric, g_{ij}, is the 3-metric that is evolved in the ADM formulation. The time parts of the 4-metric are defined by the lapse function, α, and shift vector, β^i:

$$g_{00} = -(\alpha^2 - \beta^i \beta_i) \qquad (2.20)$$

$$g_{0i} = \beta_i. \qquad (2.21)$$

(In Eq. (2.20)–(2.21) and henceforth, spatial indices are raised and lowered with the 3-metric g_{ij} and its 3-dimensional inverse g^{ij}.) The lapse function and shift vector determine the time evolution of the coordinates of the system. They relate the coordinates on slices at different times. See Figure 2.1. As the Einstein equations are valid in any coordinate system, the choice of lapse and shift constitutes a gauge choice. For numerical purposes, some gauges are better than others.

The momentum of the 3-metric is the extrinsic curvature tensor, K_{ij}. This tensor describes the embedding of the various slices in spacetime. The metric and

9
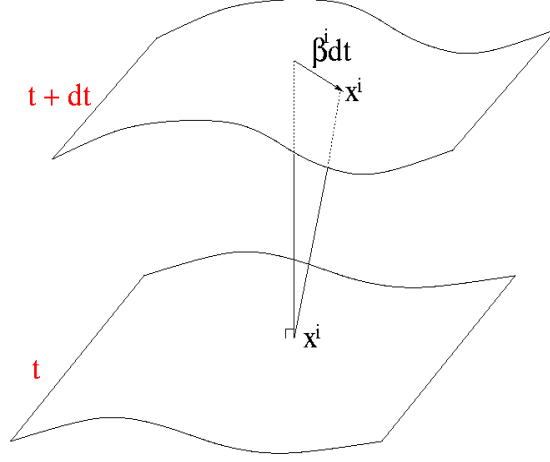
Figure 2.1: The lapse function α and shift vector β^i describe the time evolution of the coordinates. Spatial coordinate x^i on slice at time t is shifted from the normal by value $\beta^i dt$ on slice at time $t + dt$. The proper time elapsed between slice t and $t + dt$ is αdt.

extrinsic curvature tensor are the dynamic variables in the formulation. The evolution equations are written in terms of the 3-metric tensor, extrinsic curvature tensor, and the gauge choice of lapse function and shift vector. The 3-Ricci tensor, R_{ij}, contains first and second spatial derivatives of the 3-metric. The evolution equations are:

$$\partial_t g_{ij} = -2\alpha K_{ij} + \pounds_\beta g_{ij} \tag{2.22}$$

$$\partial_t K_{ij} = -\nabla_i \nabla_j \alpha + \alpha(R_{ij} - 2K_{ik}K^k_{\ j} + KK_{ij}) + \pounds_\beta K_{ij} \tag{2.23}$$

where

$$\pounds_\beta g_{ij} = \beta^k g_{ij,k} + g_{kj}\beta^k_{\ ,i} + g_{ik}\beta^k_{\ ,j} \tag{2.24}$$

$$\pounds_\beta K_{ij} = \beta^k K_{ij,k} + K_{kj}\beta^k_{\ ,i} + K_{ik}\beta^k_{\ ,j}. \tag{2.25}$$

The constraint equations are written only in terms of the 3-metric and extrinsic curvature tensors. The 3-Ricci scalar, R, contains first and second spatial derivatives

10

of the 3-metric. The constraints are independent of the choice of coordinates and are consequently independent of the lapse function and shift vector. The Hamiltonian and momentum constraint equations are, respectively:

$$0 = \frac{1}{2}\left(R - K_{ij}K^{ij} + K^2\right) \tag{2.26}$$

$$0 = \nabla_j K^{ij} - \nabla^i K. \tag{2.27}$$

The Bianchi identities ensure that if the metric and extrinsic curvature satisfy the constraint equations initially, they will remain satisfied under the action of the evolution equations for all time. As the constraint equations are never quite satisfied in a numerical simulation, it is helpful to define terms for the Hamiltonian and momentum constraint violations as a way to measure how well the constraint equations are satisfied in an evolution:

$$C^0 = \frac{1}{2}\left(R - K_{ij}K^{ij} + K^2\right) \tag{2.28}$$

$$C^i = \nabla_j K^{ij} - \nabla^i K. \tag{2.29}$$

2.3   Well-Posedness

The concept of a well-posed problem, introduced in 1902 by Hardamard [7], is generally understood to satisfy three criteria:

- a solution to the problem exists (existence)

- the solution is unique (uniqueness)

- the solution depends continuously on the problem data (stability).

A more restrictive definition of well-posedness for the Cauchy problem is the following [8]:

A system of partial differential equations is called well-posed if there exist constants
K and α independent of the data that satisfy

$$|u\left(\cdot,t\right)| < Ke^{\alpha t}|u\left(\cdot,0\right)| \tag{2.30}$$

for all $t \geq 0$.

As attempts to numerically solve ill-posed problems will result in unusuable solutions, it is crucial examine this issue closely.

Hyperbolicity is closely related to well-posedness for the Cauchy problem. Hyperbolicity is a condition in the matrix of spatial derivatives A in the first-order system

$$\dot{u} = Au + B(u). \tag{2.31}$$

If all eigenvalues of A are real and A has a complete set of eigenvectors, the system is strongly hyperbolic. If all the eigenvalues of A are real but A does not have a complete set of eigenvectors, the system is weakly hyperbolic. Kreiss and Busenhart [8] have shown equivalence between strong hyperbolicity and the stronger definition of well-posedness, Eq. (2.30). Weakly hyperbolic systems, however, fail to meet the stronger well-posedness criteria in Eq. (2.30).

A major criticism of the ADM formulation is that the evolution equations are not provably well-posed (the set of equations is only weakly hyperbolic), except under very specific conditions, namely the use of a densitized lapse and constraint subtraction [9]. However, remarkably stable and convergent results have been obtained with the ADM evolution equations modified by subtracting constraints from the right hand side of the $\dot{K}$ equations (Eq. (2.23)) in three dimensional simulations of isolated black holes. Several have reported stable unconstrained evolutions by slightly modifying the ADM evolution equations [10].

The question of well-posedness when solving the full ADM equations, both constraint and evolution, is yet unclear. However, numerical experiments presented

here suggest that at the very least, constrained evolution is better conditioned than unconstrained evolution.

While a principal motivation in using the ADM equations is the small number of dynamic variables (12) and the simplicity of the formulation, concerns about well-posedness suggest examining a first-order, strongly hyperbolic formulation of the ADM equations. Theorems about the well-posedness of such formulations exist, provided the system has "nearly" constant coefficients [11].

2.4 Generalized Frittelli-Reula

One of the simplest hyperbolic formulations of the ADM equations is based on the work of Frittelli and Reula [12] and later generalized by Hern and Stewart [13]. New dynamic variables related to first derivatives of the metric are introduced, resulting in 30 dynamic variables. Further, the entire system is written in a flux conservative form. Another advantage of the system is the ability to recover the evolution equations for other formulations by varying three parameters: η, γ, and Θ. This section will state the formulation and necessary equations for numerical implementation. A more complete discussion and development can be found in Hern's thesis [13], which is the source for the equations in this section.

The generalized Frittelli-Reula (GFR) formulation uses the same definition for the metric tensor as the ADM formulation. The extrinsic curvature, however, is modified slightly. To avoid confusion in notation, the GFR dynamic variables will be listed as h^{ij}, P^{ij}, and $M^{ij}{}_k$ and the ADM dynamic variables as g_{ij} and K_{ij}. The lapse and shift in GFR will be N and N^i while for ADM it will remain α and β^i. The relationships between the ADM and GFR variables are:

$$h^{ij} = g^{ij} \tag{2.32}$$

$$P^{ij} = K^{ij} - h^{ij}K \tag{2.33}$$

$$M^{ij}{}_k = \frac{1}{2}\left(\partial_k h^{ij} - h^{ij}h_{mn}\partial_k h^{mn}\right). \tag{2.34}$$

Terms involving the constraints are explicitly subtracted from the right hand sides of the $\dot{P}^{ij}$ and $\dot{M}^{ij}{}_k$ expressions via the η and γ parameters:

$$\partial_t M^{ij}{}_k = (\ldots) - \left(\eta N \delta^i{}_k C^j + \eta N \delta^j{}_k C^i\right) \tag{2.35}$$

$$\partial_t P^{ij} = (\ldots) + 2\gamma N h^{ij} C^0, \tag{2.36}$$

where C^0 is the Hamiltonian constraint and C^i is the momentum constraint.

One additional constraint results from the definition of the $M^{ij}{}_k$ variables:

$$\partial_n M^{ij}{}_k + M_n M^{ij}{}_k = \partial_k M^{ij}{}_n + M_k M^{ij}{}_n. \tag{2.37}$$

The extent to which this constraint is incorporated in the evolution equations is controlled via the Θ parameter; a choice of $\Theta = 0$ does not incorporate this constraint at all.

By varying these parameters, the first-order ADM evolution equations can be recovered as well as strongly hyperbolic forms of the evolution equations. Of particular interest are those parameter choices which are strongly hyperbolic and have physically realistic characteristic speeds. This leads to two conditions on the choice of η, γ, and Θ:

$$\Theta = 1 - \frac{1}{3\eta}, \quad \gamma = \frac{9\eta - 2}{12\eta - 3}, \quad \text{for } \eta \in \mathbb{R}\backslash\{0, \frac{1}{4}\}. \tag{2.38}$$

Simulations presented later will principally explore parameter choices which are strongly hyperbolic. A few simulations will explore first-order ADM and other weakly hyperbolic parameter choices. To recover the first-order ADM evolution equations, η and γ are chosen to be zero with Θ arbitrary. The first-order ADM equations are not the same as the standard ADM equations, Eq. (2.22) and (2.23). The standard ADM equations are first-order only in time; they use second spatial derivatives of the metric in calculating the Ricci tensor. In contrast, the first-order

14

ADM equations are first-order both in time and space; consequently, they have more dynamic variables than do the standard ADM equations.

The GFR formulation densitizes the lapse, N, by using a slicing density Q. The lapse is determined from the slicing density and the determinant of the evolved metric:

$$N = Q\sqrt{\det h_{ij}}. \tag{2.39}$$

The slicing density Q is not a dynamic variable nor determined by one. It is specified by the coordinates in which one chooses to perform the simulation. For the results in this thesis, Q is selected to give the Kerr-Schild lapse at the start of a simulation. The concepts behind a densitized lapse are discussed further in section 4.8.

The source-free evolution equations for the GFR formulation are:

$$\partial_t h^{ij} - \partial_n(N^n h^{ij}) = N(2P^{ij} - Ph^{ij}) - 2N^{(i,j)} - h^{ij}N^n{}_{,n}, \tag{2.40}$$

$$\partial_t M^{ij}{}_k + \partial_n(2N\eta\delta_k^{(i}P^{j)n} - N\delta_k^n P^{ij} - N^n M^{ij}{}_k) \tag{2.41}$$
$$= N\left(P^{ij}M_k - PM^{ij}{}_k - 2\eta\delta_k^{(i}\left[P^{j)n}M_n - \frac{1}{2}PM^{j)} - Q_{,n}Q^{-1}P^{j)n}\right.\right.$$
$$\left.\left. + M_{nm}{}^{j)}P^{nm} - 2M^{j)m}{}_n P_m{}^n\right]\right)$$
$$- 2N^{(i}{}_{,n}M^{j)n}{}_k + N^m{}_{,k}M^{ij}{}_m - N^n{}_{,n}M^{ij}{}_k + h^{ij}N^n{}_{,nk} - N^{(i,j)}{}_k,$$

$$\partial_t P^{ij} + \partial_n\left(2N\left(1-\Theta\right)h^{n(i}M^{j)k}{}_k\right. \tag{2.42}$$
$$\left. + 2N\Theta M^{n(ij)} - NM^{ijn} + 2\left(\gamma-1\right)Nh^{ij}M^{nk}{}_k - N^n P^{ij}\right)$$
$$= N\left(4M^n{}_k{}^{(i}M^{j)}{}_n{}^k - M^k{}_n{}^i M^n{}_k{}^j - 2M^i{}_k{}^n M^{jk}{}_n\right.$$
$$+ \frac{3}{2}M^{ij}{}_k M^k - 3(1-\Theta)M^{(i}M^{j)n}{}_n + \frac{1}{2}M^i M^j + 4(1-\Theta)M^{in}{}_n M^{jk}{}_k$$
$$+ 2(2\Theta - 1)M^{ik}{}_n M^{jn}{}_k - 3\Theta M_k M^{k(ij)} + 4(\gamma-1)M^{ij}{}_k M^{kn}{}_n - Q^{,ij}Q^{-1}$$
$$- 2(1-\Theta)\left[Q_{,k}Q^{-1}M^{k(ij)} - Q^{,(i}Q^{-1}M^{j)n}{}_n\right]$$
$$\left. + h^{ij}\left[Q_{,k}{}^k Q^{-1} + \gamma(2Q_{,k}Q^{-1}M^{kn}{}_n + \frac{1}{2}P^2 - P_n{}^k P_k{}^n)\right.\right.$$

15

$$+2(\gamma - 1)(M^{km}{}_n M_k{}^n{}_m - \frac{3}{2} M_k M^{kn}{}_n + \frac{1}{4} M_k M^k - \frac{1}{2} M^k{}_n{}^m M_k{}^n{}_m) \Big]$$

$$+ 2 P_k{}^i P^{kj} - \frac{3}{2} P P^{ij}\Big) - 2 P^{k(i} N^{j)}{}_{,k} - P^{ij} N^k{}_{,k}.$$

Unlike the standard ADM equations, all derivatives in this system are first-order. The large number of variables increases the memory requirements of a simulation using GFR, but avoiding the need to calculate mixed derivatives greatly simplifies the implementation of the system. A comparison between first-order ADM and standard ADM, examined in section 5.3, shows a distinct advantage to using first-order in time, second-order in space systems.

2.5 Kerr-Schild Coordinates

Kerr-Schild coordinates [14] are particularly well suited for numerical evolution because the 3-metric for a single black hole is simply a function added to the flat space 3-metric:

$$g_{ij} = \delta_{ij} + 2H l_i l_j, \tag{2.43}$$

where H is a scalar function of the coordinates and l_i is the spatial part of a null vector l_μ, given below. The full Kerr-Schild metric follows the same pattern:

$$ds^2 = \eta_{\mu\nu} dx^\mu dx^\nu + 2H l_\mu l_\nu dx^\mu dx^\nu. \tag{2.44}$$

For a black hole with spin a and mass m, the scalar function H and null vector l_μ become:

$$H = \frac{mr}{r^2 + a^2 \cos^2 \theta} \tag{2.45}$$

$$l_\mu = \left(1, \frac{rx + ay}{r^2 + a^2}, \frac{ry - ax}{r^2 + a^2}, \frac{z}{r}\right), \tag{2.46}$$

where

$$z = r \cos \theta \tag{2.47}$$

16

$$r^2 = \frac{1}{2}(\rho^2 - a^2) + \sqrt{\frac{1}{4}(\rho^2 - a^2)^2 + a^2 z^2} \qquad (2.48)$$

$$\rho = \sqrt{x^2 + y^2 + z^2}. \qquad (2.49)$$

Kerr-Schild coordinates are also helpful in developing reasonable approximations to multiple black hole spacetimes with arbitrary boosts and spin axes. Approximations to multiple black hole spacetimes can be created by summing the $2H l_\mu l_\nu$ contribution for each black hole in the system. This approximation, called superposition, will be discussed in section 4.9.

All the simulations presented herein use Kerr-Schild coordinates. Kerr-Schild data for a non-spinning black hole in spherical and Cartesian coordinates are found in appendix B.

2.6   Discrete Measure Definitions

Directly monitoring the violation of the constraints and field values at each point across a simulation grid for each timestep in a simulation is impractical. Three definitions are used in reducing an array of values to a single number for monitoring the behavior across the grid of a simulation. These are the max-norm, l_2-norm, and rms-norm. The max-norm is the component of the array with the largest absolute value. The l_2-norm is the square root of the sum of the squares of each point in the array:

$$l_2(\mathbf{x}) = \sqrt{\sum_{i=0}^{N} (x^i)^2}. \qquad (2.50)$$

The rms-norm is the l_2-norm divided by the square root of the number of points in the array:

$$rms(\mathbf{x}) = \frac{l_2(\mathbf{x})}{\sqrt{N}}. \qquad (2.51)$$

These measures will be used throughout this thesis.

Chapter 3

Constraint Solving

The time-time component (G_{00}) and time-space components (G_{0i}) of the Einstein tensor are constraints. The constraints, called the Hamiltonian and momentum constraints, remain satisfied under the action of the evolution equations provided that the data satisfy the constraints initially and the evolution equations are solved exactly. In numerical efforts to solve the Einstein equations, neither of these conditions is satisfied. Further, constraint violations contribute to numerical instabilities in solving the Einstein equations. Methods to solve the constraint equations are required for successful simulations of the Einstein equations.

This chapter discusses the York and Piran method for solving the constraint equations. Techniques appropriate to preparing initial data for simulations and conducting constrained evolution are also discussed.

3.1   The Conformal Transverse-Traceless Decomposition

The York and Piran method for solving the constraints [3], known as the conformal transverse-traceless decomposition, converts the constraint equations into elliptic equations for four potentials, ϕ and w^i. Other methods for solving the constraints

include the physical transverse-traceless decomposition [15] and the conformal thin sandwich decomposition [16]. A discussion of these can be found in Bonning et. al.[17]. The conformal transverse-traceless method will be used exclusively here.

An initial guess for the fields g_{ij} and K_{ij} is required to solve the constraints. The potentials appearing in the elliptic equations of the conformal transverse-traceless decomposition relate trial fields, indicated by an overhead tilde, to the solved fields. The trace of the extrinsic curvature, $K = K^i_{\ i}$, is left unchanged by this method ($K = \tilde{K}$); only the trace free parts of the extrinsic curvature,

$$A_{ij} = K_{ij} - \frac{1}{3}g_{ij}K \tag{3.1}$$

are modified by the four potentials. The relations between the four potentials, trial fields, and solved fields are:

$$g_{ij} = \phi^4 \tilde{g}_{ij}, \tag{3.2}$$
$$A^{ij} = \phi^{-10}(\tilde{A}^{ij} + (\tilde{lw})^{ij}), \tag{3.3}$$

where

$$(\tilde{lw})^{ij} \equiv \tilde{\nabla}^i w^j + \tilde{\nabla}^j w^i - \frac{2}{3}\tilde{g}^{ij}\tilde{\nabla}_k w^k. \tag{3.4}$$

The equations for the potentials are:

$$\tilde{\nabla}^2 \phi = (1/8)\left[\tilde{R}\phi + \frac{2}{3}\tilde{K}^2\phi^5 - \right.$$
$$\left. \phi^{-7}\left(\tilde{A}^{ij} + (\tilde{lw})^{ij}\right)\left(\tilde{A}_{ij} + (\tilde{lw})_{ij}\right)\right], \tag{3.5}$$
$$\tilde{\nabla}_j(\tilde{lw})^{ij} = \frac{2}{3}\tilde{g}^{ij}\phi^6\tilde{\nabla}_j\tilde{K} - \tilde{\nabla}_j\tilde{A}^{ij}. \tag{3.6}$$

For boundary conditions, the potentials are either set to trivial values ($\phi = 1$, $w^i = 0$) or a Robin condition [17] [18] is applied. Due to the excision techniques employed to handle the singularity, black hole simulations require both inner and outer boundary conditions. Unless noted, all results presented use Dirichlet boundary conditions with the potentials set to trivial values at both boundaries when

19

solving the constraint equations. More discussion of boundary conditions can be found in section 4.10.

3.2 Constraint Solving Analytic Solutions

Most examples of constraint solving using the York and Piran method deal with creating valid binary black hole initial data. In such cases the trial metric and extrinsic curvature are usually analytic functions, constructed via superposition (see section 4.9) or some other gridless technique thereby supplying highly accurate or even analytic derivative expressions of the trial fields. Few examples exist of solving the constraints for an analytic solution of the Einstein equations defined on a grid. Since the solution is exact, the constraints would be satisfied to machine round-off error were it not for the truncation error present in constraint evaluation.

Consider the following example of an isolated Schwarzschild black hole using Kerr-Schild coordinates in 1-D/spherical symmetry. Constraint violations, C^0 and C^r, for the analytic solution are presented at three resolutions. See Figures 3.1 and 3.2. In the lower resolution case of Figure 3.1, the constraint violation actually increases after a constraint solve. However, as the elliptic solve tolerance is tightened, the violation approaches an asymptotic solution. For finer discretization, constraint solving decreases the constraint violations even for rather loose elliptic solve tolerances but quickly reaches an asymptotic value. For resolutions of 5 points/M or higher, the constraint solver produces essentially the same constraint violation as the unsolved fields, regardless of the elliptic solve tolerance. The constraint solver is limited by the truncation error from differencing the potentials, ϕ and w^i. But in addition, the level of constraint violation is affected by the truncation error from differencing the trial fields, $\tilde{g}_{ij}$ and $\tilde{A}_{ij}$.
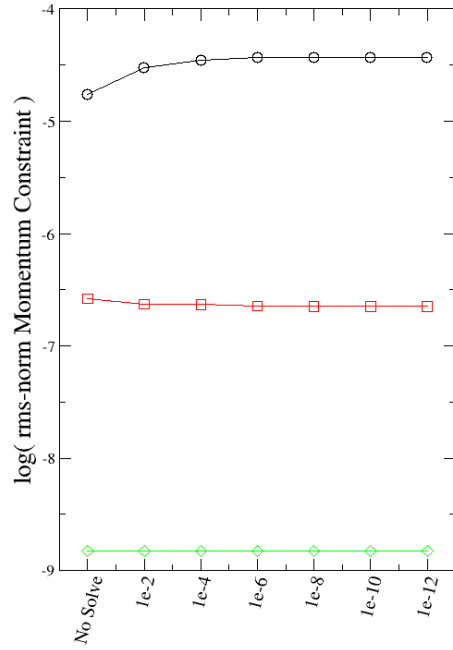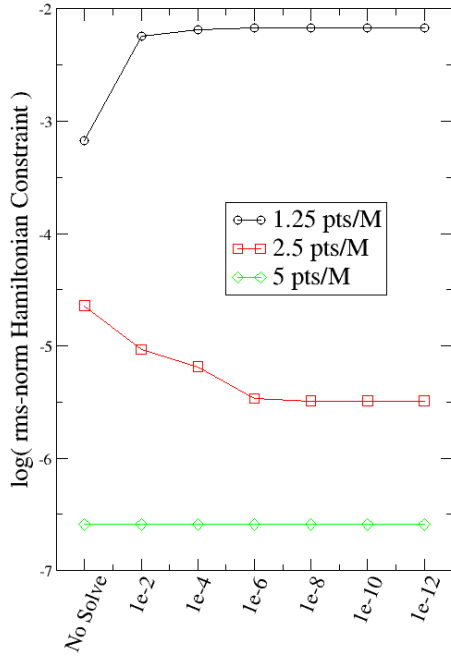
Figure 3.1: The log of the rms-norm for the Hamiltonian constraint violation is shown here for the analytic solution of an isolated Schwarzschild black hole in Kerr-Schild coordinates specified on a grid with a resolution of 1.25, 2.5, or 5 points/M. Truncation error in derivatives of the potentials as well as in the trial fields limits the level to which the constraints can be solved.

Figure 3.2: The log of the rms-norm of the momentum constraint violation for the same data sets as is Figure 3.1.

21

Chapter 4

Numerical Methods

A crucial component to any numerical work is the choice of numerical methods. For large simulations, two issues dominate the choice: efficiency and accuracy. This chapter will summarize the numerical methods chosen and implemented in the black hole codes and explain at the algorithm level how they work. Code performance results as well as code verification strategies will also be discussed.

4.1   The Finite Difference Approximation

The finite difference approach consists of using Taylor Series expansions to replace a partial differential equation with an algebraic equation on a computational grid, called the discretized form of the equation. Solving the discretized partial differential equation then consists of a finite series of basic floating point operations which can be performed with considerable speed on a computer.

The finite difference approach approximates a continuum expression using the Taylor Series expansion. By taking Taylor Series expansions about a point, a discrete approximation to the derivative at that point can be obtained:

$$f(x + h) \ \ = \ \ f(x) + h\frac{df}{dx}|_x + \frac{h^2}{2}\frac{d^2f}{dx^2}|_x + \frac{h^3}{6}\frac{d^3f}{dx^3}|_x + \cdots \qquad (4.1)$$

$$f(x - h) = f(x) - h\frac{df}{dx}\Big|_x + \frac{h^2}{2}\frac{d^2f}{dx^2}\Big|_x - \frac{h^3}{6}\frac{d^3f}{dx^3}\Big|_x + \cdots \qquad (4.2)$$

$$\frac{df}{dx} = \frac{f(x+h) - f(x-h)}{2\,h} - \frac{1}{6}f'''(\zeta)h^2, \qquad (4.3)$$

where $x - h \leq \zeta \leq x + h$ and h is the grid spacing. The discrete approximation differs from the continuum expression by a truncation error related to the computational grid spacing and the higher derivatives of the function being differentiated. A numerical solution to the discretized equation converges to the exact solution as the grid spacing asymptotically approaches zero.

Convergence in a numerical solution is a critical part of code verification. An early example addressing convergence of an approximate solution with the finite difference approach is Courant, Friedrichs and Lewy in 1928 [19] [20]. This principle affects all the simulations presented in this thesis: no single numerical simulation can claim to solve a differential equation. Several numerical simulations at differing resolutions are required to demonstrate convergence and establish a solution. This point will be addressed further in section 4.11.

All spatial finite differences used in the black hole codes are fourth order, meaning they have a truncation error proportional to h^4. A complete listing of the finite difference stencils used in the codes is found in appendix A.

When not near the hole, the spatial finite difference stencil most frequently used is centered fourth order. However, the advection terms requiring finite differencing in the ADM equations, underlined in Eq. 4.4–4.5,

$$\pounds_\beta g_{ij} = \beta^k \underline{\partial_k g_{ij}} + g_{kj}\partial_i \beta^k + g_{ik}\partial_j \beta^k \qquad (4.4)$$

$$\pounds_\beta K_{ij} = \beta^k \underline{\partial_k K_{ij}} + K_{kj}\partial_i \beta^k + K_{ik}\partial_j \beta^k, \qquad (4.5)$$

are differenced using stencils that are biased in the direction of the shift vector field, β^i, throughout the computational domain. See Figure 4.1. Advection terms in the GFR equations are treated similarly. The gauge derivatives are not finite differenced because they are given analytically (see section 4.8).
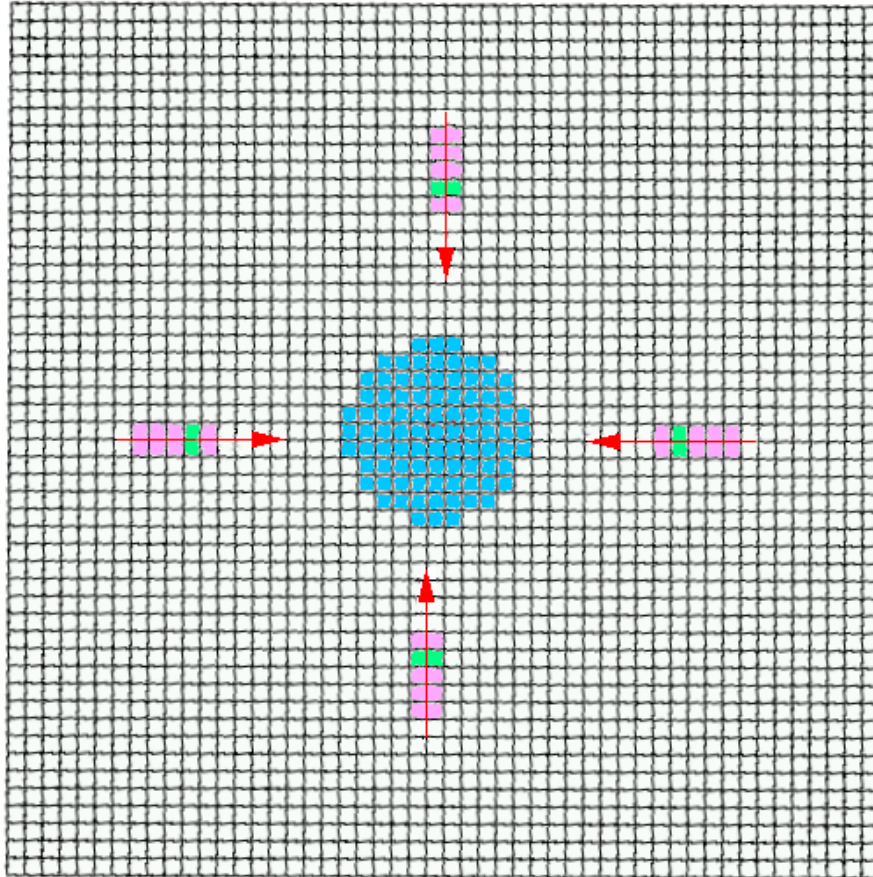
Figure 4.1: Example of skewed stencils for finite differencing transport terms. This is a 2-D slice from the 3-D grid structure for an isolated black hole simulation. The blue region in the center indicates the location of the black hole. The red arrows show the direction of the advection flow, $-\beta^i$. To find the finite difference approximation for transport terms located in the green cells, the stencil, consisting of the purple cells, is skewed towards the source of the advection flow.

Schemes that use differencing stencils skewed in the direction of the advection flow source are common when evolving advective equations [21]. The transport properties of advective equations are more easily modelled when the differencing stencils reflect those properties.

Finding a stable finite differencing scheme for an evolution can be challenging. Many options exist for approximating the spatial derivatives that appear in the ADM evolution equations. I performed extensive experiments in one and three dimensions which varied the type and order of spatial derivatives in the ADM equations. The tests used iterative Crank-Nicholson to evolve an isolated Schwarzschild black hole in spherical symmetry. The results gave two clear guidelines for differencing the ADM equations:

- the advection terms must be one-sided differenced

- the second derivatives of the metric in the Ricci tensor must be centered differenced.

See Figure 4.2. These results are exactly what would be expected for differencing an advection equation or a wave equation.

4.2   Adams-Moulton

The numerical method chosen to solve the evolution portion of the Einstein equations is Adams-Moulton as implemented in the PVODE package of the SUNDIALS suite [22] [23] [24]. Adams-Moulton is a predictor-corrector method for solving the initial value problem:

$$\dot{y} = f(t, y) \tag{4.6}$$

$$y(t_0) = y_0. \tag{4.7}$$
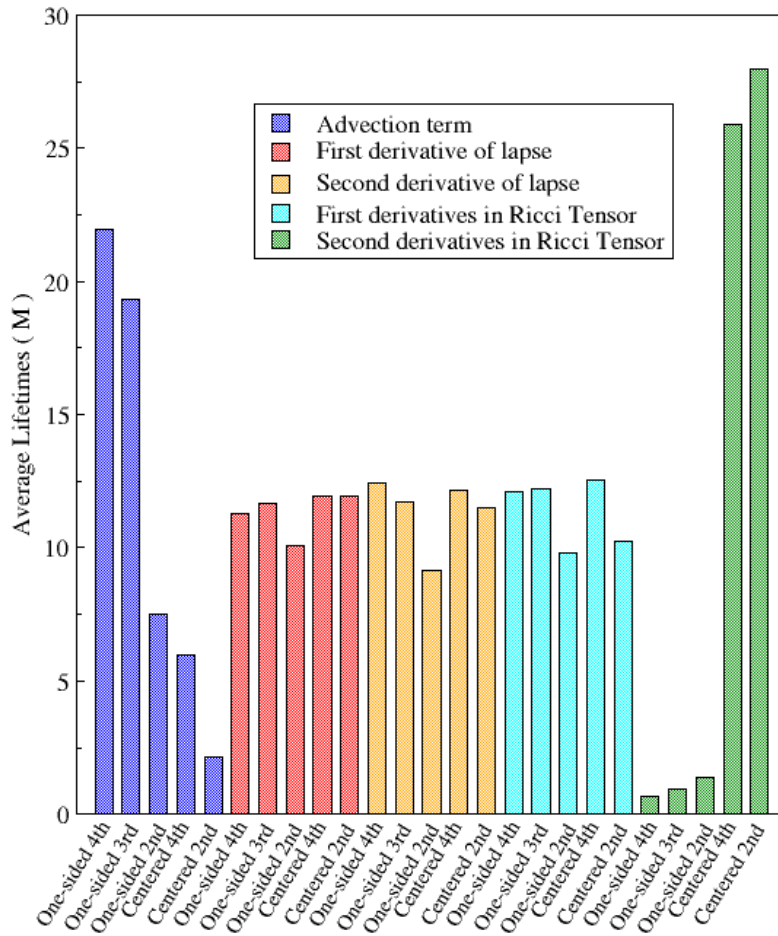
Figure 4.2: Results from simulations in spherical symmetry using iterative Crank Nicholson for the time evolution. Various combinations of finite differencing choices were attempted for the spatial derivatives required in the ADM equations. The finite difference stencils were either one-sided or centered. The order of the stencils varied from second to fourth order. These results indicate only two guidelines for finite differencing the ADM evolution equations: the advection terms must be one-sided differenced and the second derivatives of the metric in the Ricci tensor must be centered differenced.

26

For efficiency, the method was implemented by the SUNDIALS team in a variable-order, variable-stepsize form.

The Adams-Moulton predictor-corrector method originates from the approach where Eq. (4.6) is integrated on both sides and the integral replaced with a quadrature formula:

$$y(t) - y(t_0) = \int_{t_0}^{t} f(\tau, y(\tau))d\tau \tag{4.8}$$

$$y(t) \approx y(t_i) + \sum_{j=0}^{k} A_j f(t_j, y(t_j)), \tag{4.9}$$

where $t_i \leq t_0 < t_1 < \cdots < t_k \leq t$; A_j are the appropriate quadrature coefficients. This approach requires more than the initial value, y_0, to get started. For simple problems, the predictor values could be provided by a standard method such as Runge-Kutta. For a more complicated approach, an interpolation formula employing points that are outside the integration interval can be used as the predictor step. This approach is named Adams-Bashforth. The Adams-Moulton method uses for a predictor Adams-Bashforth and for a corrector a quadrature formula. The predictor is explicit and the corrector is implicit.

As an example, consider the 5th order Adams-Bashforth formula [25] with time discretization Δt:

$$\int_{i}^{t_{i+1}} \dot{y}(\tau)d\tau =$$
$$\frac{\Delta t}{24}[55\dot{y}(t_i) - 59\dot{y}(t_{i-1}) \quad + \quad 37\dot{y}(t_{i-2}) - 9\dot{y}(t_{i-3})] + \frac{251(\Delta t)^5}{720}\dot{y}^v. \tag{4.10}$$

Because all the points needed to estimate the integral are either at the boundary of or immediately outside of the integration interval, Eq. (4.10) can be used to predict the solution at time t_{i+1}. The subsequent corrector step is made implicit by including the predicted solution at time t_{i+1} in a quadrature formula:

$$y_{i+1}^* = y_i + \frac{\Delta t}{24}[55\dot{y}_i - 59\dot{y}_{i-1} + 37\dot{y}_{i-2} - 9\dot{y}_{i-3}] \tag{4.11}$$

27

$$y_{i+1} \quad = \quad y_i + \frac{\Delta t}{24}[\dot{y}_{i-2} - 5\dot{y}_{i-1} + 19\dot{y}_i + 9\dot{y}_{i+1}^*], \tag{4.12}$$

where $\dot{y}_{i+1}^* = f(t_{i+1}, y_{i+1}^*)$ and $\dot{y}_i = f(t_i, y(t_i))$.

The general Adams-Moulton formula is

$$\sum_{i=0}^{1} \alpha_{n,i} y_{n-i} + \Delta t_n \sum_{i=0}^{q-1} \beta_{n,i} \dot{y}_{n-i} = 0. \tag{4.13}$$

The timestep is $\Delta t_n = t_n - t_{n-1}$; y_n is the numerical approximation to the solution of $y(t_n)$ as just discussed. Coefficients $\alpha_{n,i}$ and $\beta_{n,i}$ are determined by the order of integration, the timestep history, and normalization $\alpha_{n,0} = -1$. Variable q is the order of integration.

4.3 Inexact Newton-Krylov

Solving the ADM constraint equations (Eq. (2.26)–(2.27)) requires solving a boundary value problem as discussed in section 3.1. Since the discretized form of the governing equations (Eqs. (3.5–3.6)) gives a set of nonlinear algebraic equations, Newton-like methods provide the simplest way to solve the system. The problem can be stated as follows: Given n unknowns with n real valued functions,

$$\mathbf{F}(\mathbf{x}) = \begin{bmatrix} f_1(\mathbf{x}) \\ f_2(\mathbf{x}) \\ \vdots \\ f_n(\mathbf{x}) \end{bmatrix} \tag{4.14}$$

where $\mathbf{x} = (x_1, x_2, \ldots, x_n)$, a vector $\mathbf{s} = (s_1, s_2, \ldots, s_n)$ is sought so that

$$\mathbf{F}(\mathbf{s}) = \mathbf{0}. \tag{4.15}$$

Newton's method for solving Eq. (4.15) involves iterating an initial guess, $\mathbf{x_0}$:

$$\mathbf{x}_{n+1} = \mathbf{x}_n - J(\mathbf{x}_n)^{-1} \mathbf{F}(\mathbf{x}_n), \tag{4.16}$$

where $J(\mathbf{x}_n)$ is the Jacobian of $\mathbf{F}$ at $\mathbf{x}_n$.

Newton's method for several variables, Eq. (4.16), now only requires the solution of a system of linear equations at each iteration. Further, the iterations can proceed until the solution meets a user specified error tolerance. Newton's method has quadratic convergence provided that the Jacobian is nonsingular [26].

Among the many options to solve a set of linear algebraic equations are direct solvers such as L-U decomposition, super L-U decomposition, or Gaussian elimination and indirect solvers such as successive over-relaxation, multigrid, and Krylov subspace methods including conjugate gradient and the Generalized Minimum RESidual method (GMRES). Indirect solvers, based on iterative methods, require an initial guess and are generally faster for the large, sparse matrices that result from finite difference operations on a grid [27].

Because iterative methods such as conjugate gradient have worked well before in constrained evolutions of magnetohydrodynamics codes [28], the Generalized Minimum RESidual method (GMRES) was selected to solve the linear systems appearing as part of Newton's method. The approach was originally implemented using the nonlinear solver tools in the PETSc toolkit [29] [30] [31], a widely used parallel toolkit maintained by Argonne National Laboratory. It has subsequently been reimplemented using KINSOL [32], part of the SUNDIALS suite [24].

4.4   Structured Adaptive Mesh Refinement

Numerical simulation of binary black hole mergers requires very large domain simulations to achieve realistic signal prediction. However, most of the large gradients in the metric that require high resolution to simulate occur in just a small fraction of the total computational domain. Maintaining a high resolution across the entire domain when it is only needed over a small volume is expensive both in terms of processor and memory requirements. Structured mesh refinement alleviates this
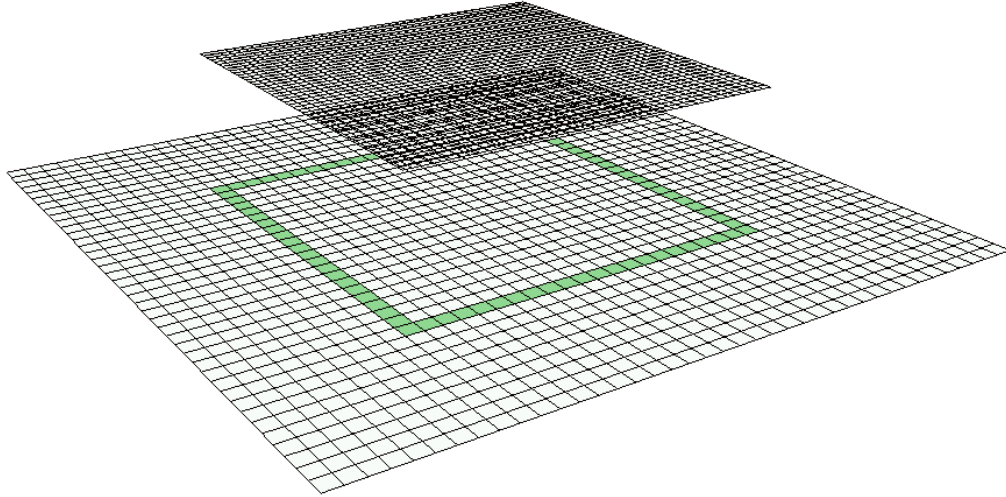
Figure 4.3: Example of nested grids. This is a 2-D slice of the grid structure from a 3-D simulation employing mesh refinement. The fine local mesh is raised slightly above the coarse global mesh to reveal the overlap region between the two levels, indicated by the green square.

problem by creating a finer spatial grid where needed that overlaps the global coarse grid. See Figure 4.3. This results in a hierarchy of nested levels which are subsequently divided into patches of data for parallel computation. The mesh refined examples in this dissertation use the SAMRAI toolkit [33] [34] [35], maintained by Lawrence Livermore National Laboratory, to handle the parallelism and data management.

To solve the governing equations on a refined grid and obtain solutions that are consistent with the unigrid case, interpolation between the various grid levels is necessary. When using cell-centered grids, as is the case for this dissertation, interpolation both to higher and lower resolutions is necessary. In the refinement step, interpolation on the coarser grid level provides the required ghostzones for the finer grid level. See Figure 4.4. These ghostzones enable the finite differencing
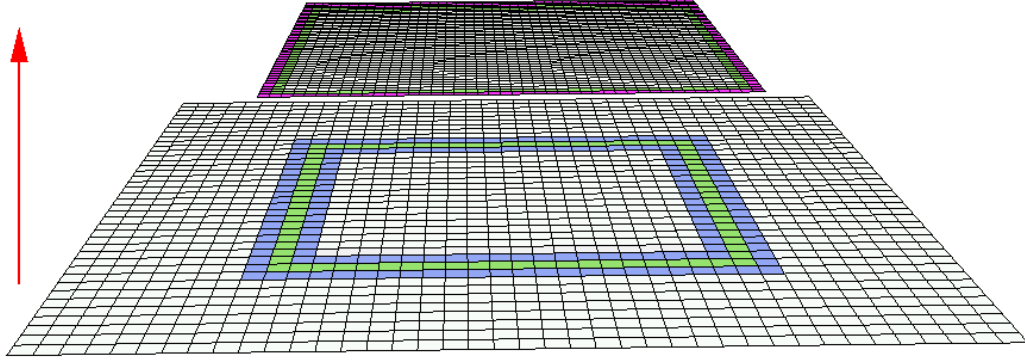
Figure 4.4: Refinement step interpolation. The coarse and fine meshes are color coded to indicate how the refinement step interpolation proceeds. The green squares indicate the overlap region between the two levels. The arrow indicates the level where the interpolated values are copied to. The fine local mesh is displayed with one ghostzone, colored purple, which is filled with interpolated values from the coarse mesh points, colored blue and green.

necessary on the finer grid level to calculate the residual of the discretized equations. In the coarsening step, interpolation on the finer grid level fills in values on the coarser grid level where the finer and coarser levels overlap. The interpolated values from the fine grid level provide solution values to the coarser grid at points interior to a sphere contained inside the overlap region of the two levels. See Figure 4.5.

For the refinement step, fourth order Lagrangian interpolation is used. For the coarsening step, cubic spline interpolation with natural boundary conditions is used. Natural boundary conditions set the second derivative at the boundaries of the interpolation function over the data points to zero. Spline routines from the gnu scientific library were employed in the coarsening interpolation [36] [37].
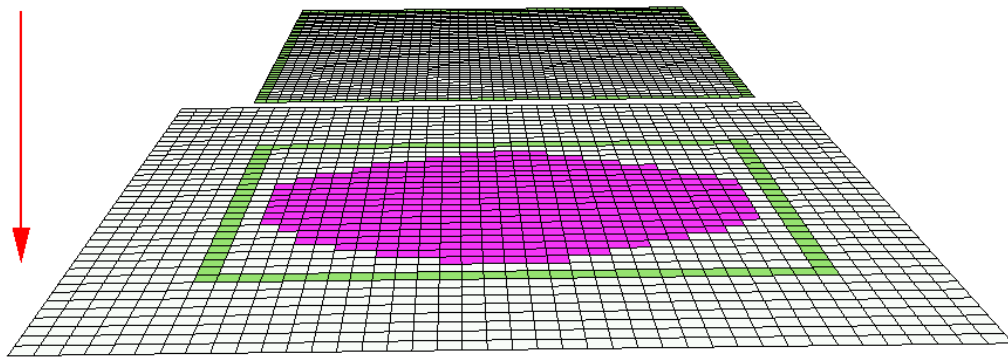
Figure 4.5: Coarsening step interpolation. The code is cell centered; consequently interpolation is necessary for the coarsening step since coarse and fine cell centers do not exactly coincide. The coarse and fine meshes are color coded to indicate how the coarsening step interpolation proceeds. The green squares indicate the overlap region between the two levels. The arrow indicates the level where the interpolated values are copied to. Interpolation on the fine local mesh provides solution values to the coarse global mesh at points interior to a sphere contained inside the overlap region of the coarse and fine meshes. The purple disk on the coarse level indicates the destination of the interpolated values from the fine level.

4.5   Code Structure and Fundamental Toolkits

High performance computing is most efficient when using robust, portable, and reusable tools. Applications built to scale on large numbers of processors require extensive development and testing and call for development expertise beyond that generally available for a new research problem. An example of this is constrained evolution. Constrained evolution requires solving elliptic and hyperbolic equations in a consistent way on large numbers of processors. The elliptic solves are computationally demanding; practicality requires the elliptic solve to use no more than 40% of the total computational time for a simulation due to limitations in resources. The development time for such a solver capable of scaling to large numbers of processors is tremendous, and this demand alone exceeds the personnel and time resources available to many research groups.

Good programming design in three independent but widely used computational toolkits (SUNDIALS, PETSc, SAMRAI) enabled their use as components in building efficient mesh refined elliptic and hyperbolic solvers. The toolkits ultimately required only minimal modification in this process, saving countless hours.

The major libraries and toolkits used in the codes are the following:

- SUNDIALS – SUite of Nonlinear DIfferential/ALgebraic equation Solvers, Center for Applied Scientific Computing (CASC), Lawrence Livermore National Laboratory (LLNL) [22] [23] [24]

- PETSc – Portable, Extensible Toolkit for Scientific Computation, Argonne National Laboratory [29] [30] [31]

- SAMRAI – Structured Adaptive Mesh Refinement Application Infrastructure, CASC, LLNL [33] [34] [35]

- HDF5 – Hierarchical Data Format 5, National Center for Supercomputing Applications, University of Illinois at Urbana-Champaign in collaboration with

Lawrence Livermore National Laboratory, Sandia National Laboratory, and Los Alamos National Laboratory [38]

- MPI – The Message Passing Interface [39].

Visualization of data was performed using ChomboVis developed at Lawrence Berkeley National Laboratory [40]. Spline routines from the Gnu Scientific Library [36] [37] were used in the mesh-refined evolutions. Maple [41], a commercial symbolic manipulation package maintained and sold by Waterloo Maple Inc., played a critical role in developing and testing the equation evaluation routines.

Four different 3-D codes, two 1-D codes, and one independent residual evaluator were used for producing the results in this thesis. I wrote each code in its entirety. All code was written in either C or C++. In spite of the extensive use of the above mentioned computational toolkits, the codes are complex. To compare complexity, the line counts and language for each code is listed in Table 4.1. The line counts for Maple–generated equation evaluation routines are not included in the code line counts but are listed in a separate column.

4.6 Parallel Performance

The size of the problems addressed requires the use of massively parallel computations. For such problems, the most important performance issue is scalability. Scalability shows how the performance of a code varies over an arbitrary number of processors. It is usually plotted in terms of the speedup as a function of the number of processors. Speedup is defined as follows:

$$\text{speedup}(n) = \frac{\text{Run time on one processor}}{\text{Run time on } n \text{ processors}}. \tag{4.17}$$

In Figure 4.6, the speedup is presented as a function of number of processors for a 3-D constrained evolution evolving a single black hole with ADM. The simulation speedup was measured using a Cray–Dell cluster consisting of PowerEdge 1750

Code Description	Language	Parallel	Line count	Maple
3-D Binary Black Hole Unigrid with ADM using PETSc	C	Yes	14086	15145
3-D Single Black Hole with ADM Mesh Refinement Capable using SAMRAI	C++	Yes	26772	4947
3-D Single Black Hole with GFR Mesh Refinement Capable using SAMRAI	C++	Yes	21595	28985
3-D Single Black Hole with ADM Overlapping Cartesian and Spherical Grids using SAMRAI enhanced by author	C++	Yes	46944	10641
1-D Single Black Hole with ADM	C	No	1529	150
1-D Single Black Hole with GFR	C	No	1708	493
Independent Residual Evaluator	C	No	1724	2403

Table 4.1: Descriptions of the various codes used to generate the results presented. The line counts for Maple–generated equation evaluation routines are not included in the code line counts but are listed in a separate column.

Xeon processors with Myrinet interconnect, providing point-to-point bandwidth of 250MB/sec. The speedup is very near ideal up to and including 64 processors. To do this demonstration, the problem had to fit on one processor. The problem thus is too small for very large numbers of processors as indicated by the fall-off in speedup for cases with more than 64 processors.

4.7   Excision

Evolving the interior of a black hole is troublesome due to the presence of the singularity. Further, the computational expense used in evolving the interior is wasted because the interior cannot causally affect the region exterior to the hole. Several methods have been developed to address this problem. Singularity avoiding spacelike slicings freeze the lapse function before reaching the singularity. This avoids evolving the singularity but also causes large gradients in the lapse near the
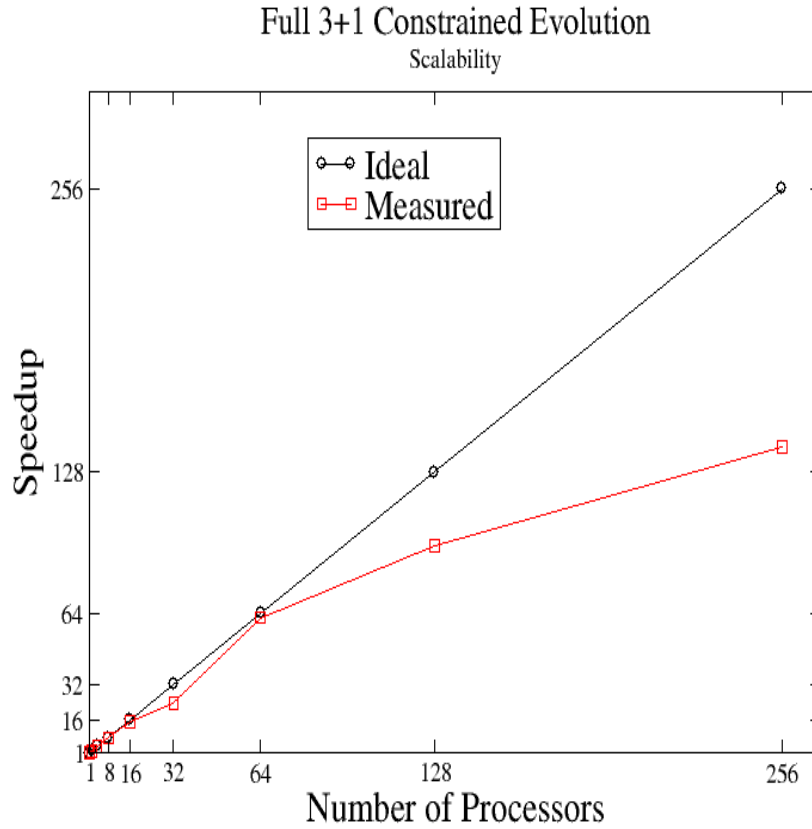
Figure 4.6: Speedup for a full $3 + 1$ constrained evolution. The speedup, as defined in Eq. (4.17), is plotted for an 80^3 simulation of a nonrotating Kerr-Schild black hole of domain $[-8M \ldots 8M]$ using constrained evolution and evolved for a duration of $10M$. The same simulation was performed repeatedly on the indicated number of processors. Because the test problem had to fit in memory on a single processor, it was necessarily small. This contributed to the larger deviation from ideal speedup when performed on 256 processors.

hole as the evolution proceeds. An alternative approach excludes the singularity rather than avoiding it in the slicing. This approach is called excision.

Excision consists of replacing the singularity in the black hole with a mask function [42]. Provided the mask function is entirely contained inside the causally disconnected region of the computational domain, excision analytically cannot affect the rest of the solution, though later chapters present evidence that the edge of the mask is contributing to long term instability of black hole spacetimes. Excision is easily generalized to multiple black hole spacetimes by simply defining and moving more than one mask function according to the dynamics of the problem. Excision has been used successfully before in relatively short (i.e. $\Delta t < 40M$) off-axis binary black hole collisions [43].

In all simulations presented here the mask function is a smooth topological sphere. This makes the excision region on a Cartesian grid appear as a discretized sphere (see Figure 4.7). Masked grid points are not evolved. For binary black holes and boosted single black holes, the mask function position changes with time in a way determined by the user. More discussion on excision with boosted black holes is found in chapter 8. The use of apparent horizon finders enables the location of the outermost marginally trapped surface on each spacelike hypersurface in order to avoid masking any points that may lie outside the black hole interior. The apparent horizon finder used in analyzing the single hole evolutions presented here was the 3-D locator based on Newton's method developed by Mijan Huq [44] [45].

4.8   Gauge Conditions

The standard $3 + 1$ form of the spacetime metric,

$$ds^2 = -\alpha^2 dt^2 + g_{ij}(dx^i + \beta^i dt)(dx^j + \beta^j dt) \tag{4.18}$$
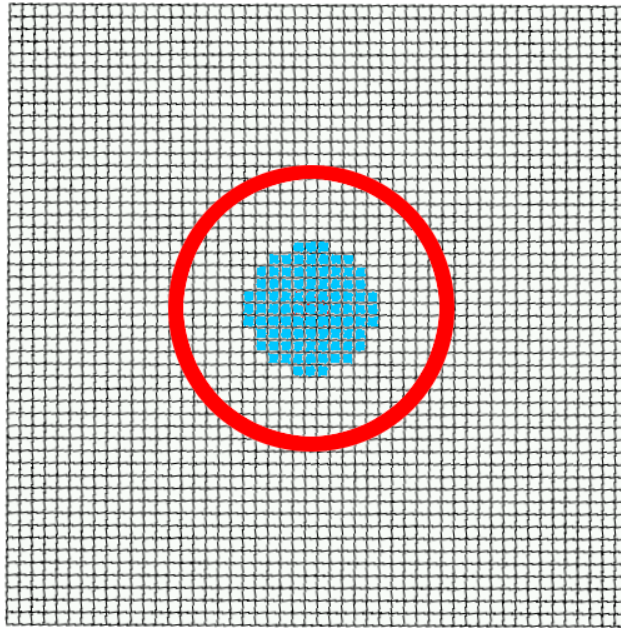
Figure 4.7: Excision region. This grid is a 2-D slice from a 3-D single black hole evolution where the black hole is placed in the center of the domain. The blue shaded cells indicate points that have been masked in order to remove the singularity and the steep gradients immediately surrounding the singularity. The apparent horizon on the hypersurface is denoted by the red circle. Several evolved buffer points inside the apparent horizon but outside the mask are also shown.

expresses the time-space and time-time components of the 4-metric in terms of the shift β^i and the lapse α, respectively. These describe the time evolution of the coordinate system, which is not set by the Einstein equations. Consequently, the lapse and shift are not specified by the 3+1 equations. The choice of these quantities is called the gauge condition.

The simplest gauge condition for evolving a black hole spacetime in Kerr-Schild coordinates (section 2.5) is to simply set the lapse and shift to their analytic values:

$$\alpha = \frac{1}{\sqrt{1 + 2H\, l_t^2}} \tag{4.19}$$

$$\beta_i = 2H\, l_t\, l_i. \tag{4.20}$$

For binary black hole spacetimes, this approach is generalized in a straightforward way:

$$\alpha = \frac{1}{\sqrt{1 + 2\,_1H\,_1l_t^2 + 2\,_2H\,_2l_t^2}} \tag{4.21}$$

$$\beta_i = 2\,_1H\,_1l_t\,_1l_i + 2\,_2H\,_2l_t\,_2l_i. \tag{4.22}$$

The subscript numbers preceeding the null vectors l^μ and the scalar function H indicate which black hole they describe.

A slightly more complicated gauge condition for evolving in Kerr-Schild coordinates consists of using a *densitized* lapse:

$$\alpha = \alpha_{\mathrm{KS}} \sqrt[n]{\frac{g}{g_{\mathrm{KS}}}}, \tag{4.23}$$

where α_{KS} is the analytic Kerr-Schild lapse, g is the determinant of the 3-metric, g_{ij}, g_{KS} is the analytic value of the determinant of the 3-metric in Kerr-Schild coordinates, and n is either 2 or 3. This gauge choice allows the lapse to vary as the metric evolves. This choice also promotes hyperbolicity in the ADM evolution equations [9].

Several numerical surveys of gauge choices and their effects on the stability of the ADM equations are available [10] [46]. This dissertation uses both the exact lapse and shift gauge condition, and the densitized lapse condition. The simulations presented will indicate which is used. In general, the densitized lapse condition does much better with constrained evolution than without.

4.9 Superposition Initial Data

Producing realistic binary black hole initial data for simulation involves superposing two Kerr-Schild single hole metrics with a technique demonstrated by P. Marronetti and R. Matzner [18]. This method produces approximate initial data that already closely satisfies the constraint equations and requires less initial solving before proceeding with the evolution. Superposition is performed with the null vectors l_i and scalar functions H of each black hole, indicated by the subscripted number immediately preceeding the null vector or scalar function. The resulting trial field approximation is indicated by an overhead tilde. The trace of the extrinsic curvature, K, and trace free parts of the extrinsic curvature, A_{ij}, are treated separately:

$$\tilde{g}_{ij} = \delta_{ij} + 2 \; {}_1H \; {}_1l_i \; {}_1l_j + 2 \; {}_2H \; {}_2l_i \; {}_2l_j \tag{4.24}$$

$$\tilde{K} = {}_1K_i{}^i + {}_2\,K_i{}^i \tag{4.25}$$

$$\tilde{A}_{ij} = \tilde{g}_{n(i} \left[{}_1K_{j)}{}^n + {}_2K_{j)}{}^n - \frac{1}{3}\delta_{j)}{}^n \tilde{K} \right] \tag{4.26}$$

A symmetrization, indicated by the subscripted parentheses, is performed on the trace free part of the extrinsic curvature to ensure that it remains symmetric after superposition:

$$V_{(ij)} = \frac{1}{2} \left(V_{ij} + V_{ji} \right) \tag{4.27}$$

The gauge variables, α and β^i, for binary black hole data are produced via an analogous superposition method as described in section 4.8.

4.10   Boundary Conditions

Two types of single hole problems are visited in this dissertation: stationary black hole evolutions and boosted black hole evolutions. Both scenarios are intended to better understand and improve binary black hole evolutions. All cases require outer and inner boundary conditions. The outer boundary consists of points that lie immediately outside the computational domain. The inner boundary consists of points that lie inside the computational domain immediately adjacent to the excision region. The excision region, or mask, is spherical and lies inside the causally disconnected region of the computational domain (see section 4.7).

The inner and outer boundary conditions for elliptic solves are Dirichlet for both single and binary black hole evolutions. The conformal factor and vector potential in the conformal transverse-traceless decomposition (see section 3.1) are set to trivial values at both boundaries:

$$\phi = 1 \tag{4.28}$$

$$w^i = (0, 0, 0). \tag{4.29}$$

For single black hole evolutions, the hyperbolic solve uses outer boundary values set to the analytic solution. The inner boundary is free, made possible by the fact that the inner boundary is causally disconnected from the rest of the computational domain. The free inner boundary is implemented by using the one-sided finite differencing stencils listed in appendix A.

For binary black hole evolutions, the hyperbolic solve uses outer boundary values set to a superposition of two Kerr-Schild single hole metrics (see section 4.9). This simple approximation has been shown to be remarkably accurate through various investigations of solved initial data using Robin boundary conditions [17] [18]. The inner boundaries for binary black hole evolutions are free, the same as for single hole evolutions.

41

4.11 Code Verification

The object of this dissertation is to produce convergent numerical solutions to the governing equations in the code. While code validation will only be possible once astrophysical gravitational wave signals are detected, code order verification using known analytic solutions provides a means to test the code implementation and find errors. This dissertation adopts the ideas of Salari and Knupp for code verification [47].

Inherent to any discrete approximation of a continuum expression is a discretization error. Truncation error in the finite difference approach, as discussed in section 4.1, gives a discretization error related to the distance between points on a grid. However, this is not the only source of error; two other contributions come from round-off error and incomplete iterative convergence error. Round-off error results from the finite-precision arithmetic performed on a computer. Incomplete iterative convergence error results when solving algebraic systems using an iterative method, such as GMRES. This error can be controlled by changing the user-specified error tolerance for the iterative method.

These three sources of error, discretization error, round-off error, and incomplete iterative convergence error, all contribute to the total error in the numerical solution. By making the iterative error tolerance small enough so that the discretization error dominates, the discretization error can be independently verified through convergence. Any inconsistencies between the theoretical and measured discretization error indicate a failure and possible coding mistake.

The test problem selected for code verification in this dissertation is the isolated Schwarzschild black hole in Kerr-Schild coordinates. This test problem has proven to be very difficult for numerical relativity codes. The problem is time-independent analytically, though most numerical attempts blow up after a certain number of evolution steps. Convergence tests for evolutions of this test problem

will be shown throughout the following chapters. The spatial finite differences in all cases are fourth order, and residual evaluations show the appropriate fourth order convergence. The time integration scheme is variable order, depending on a user-specified tolerance. In most long lifetime simulations presented in later chapters, this results in an overall convergence order of ~ 3.

Chapter 5

Unconstrained Single Black Hole Spacetimes

The vast majority of single black hole and binary black hole simulations consist of providing consistent initial data and then solving the evolution equations while only monitoring the constraint violations as the simulation proceeds. Such an evolution is called a *free* or *unconstrained* evolution. This chapter will explore several unconstrained evolutions of an isolated, non-spinning Kerr-Schild black hole in both 1-D/spherical symmetry using spherical coordinates and in full 3-D using Cartesian coordinates, for both the ADM formulation and the Generalized Frittelli-Reula formulation. To improve stability for the ADM formulation, terms proportional to the Hamiltonian and momentum constraints are subtracted from the right hand side of the $\dot{K}$ equations. Optimal constraint subtractions for the ADM formulation are presented.

5.1 Raw ADM

Evolving a single black hole using an analytic lapse and shift with the standard ADM equations is troublesome both with and without spherical symmetry. Figure 5.1 shows a small domain 1-D/spherically symmetric evolution using the standard ADM equations. The log of the rms-norm of the Hamiltonian constraint violation is plotted as a function of time in units of M, the mass of the black hole. The rms-norm of a constraint gives an average absolute value for that constraint's violation across the grid (see section 2.6). For a stable evolution of this static test problem, the rms-norm of the constraints should relax to a small, non-zero value and remain there throughout the simulation. An instability forms, however, and causes the evolution to fail. The momentum constraint likewise illustrates this instability, as seen in Figure 5.2, which plots the only relevant momentum contraint in spherical symmetry, C^r, as a function of time. Snapshots at selected times of g_{rr} plotted as a function of r are presented in Figure 5.3.

Using a densitized lapse somewhat improves the lifetime of an unconstrained evolution when evolving a Kerr-Schild black hole with spherical symmetry. Figure 5.4 shows log of the rms-norm for the Hamiltonian constraint violation as a function of time for an unconstrained black hole evolution using ADM with a densitized lapse.

The instability becomes more pronounced in the full 3-D case. Figure 5.5 shows the rms-norm of the Hamiltonian constraint violation as a function of time for a full evolution without any special symmetries. The momentum constraint violations are plotted in Figure 5.6.

Varying the computational domain does not appreciably improve the behavior of an unconstrained evolution. This is seen in Figure 5.7, which plots the l_2-norm of the Hamiltonian constraint violation as a function of time for domains of $[-5M \ldots 5M]$, $[-10M \ldots 10M]$, and $[-15M \ldots 15M]$.
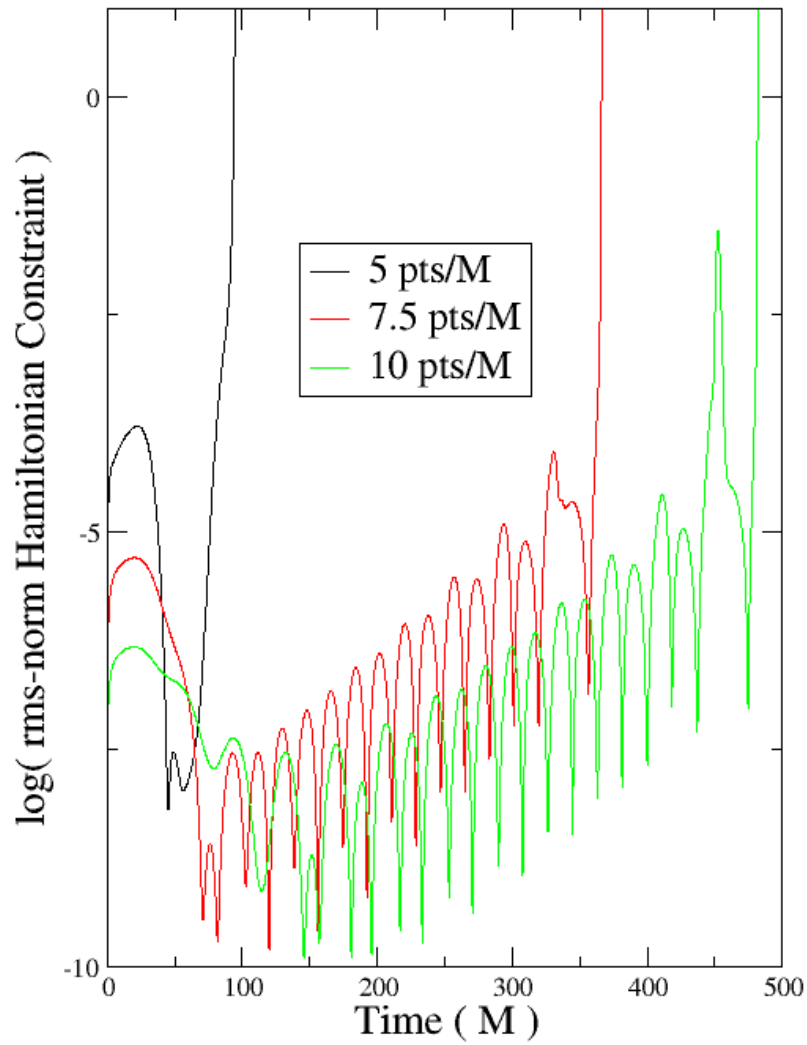
Figure 5.1: The log of the rms-norm for the Hamiltonian constraint violation as a function of time for a 1-D/spherically symmetric unconstrained black hole evolution using ADM. The domain of the simulation was $r = 0.8M \dots 10.6M$ and the lapse function was analytic. Results at three resolutions are presented.
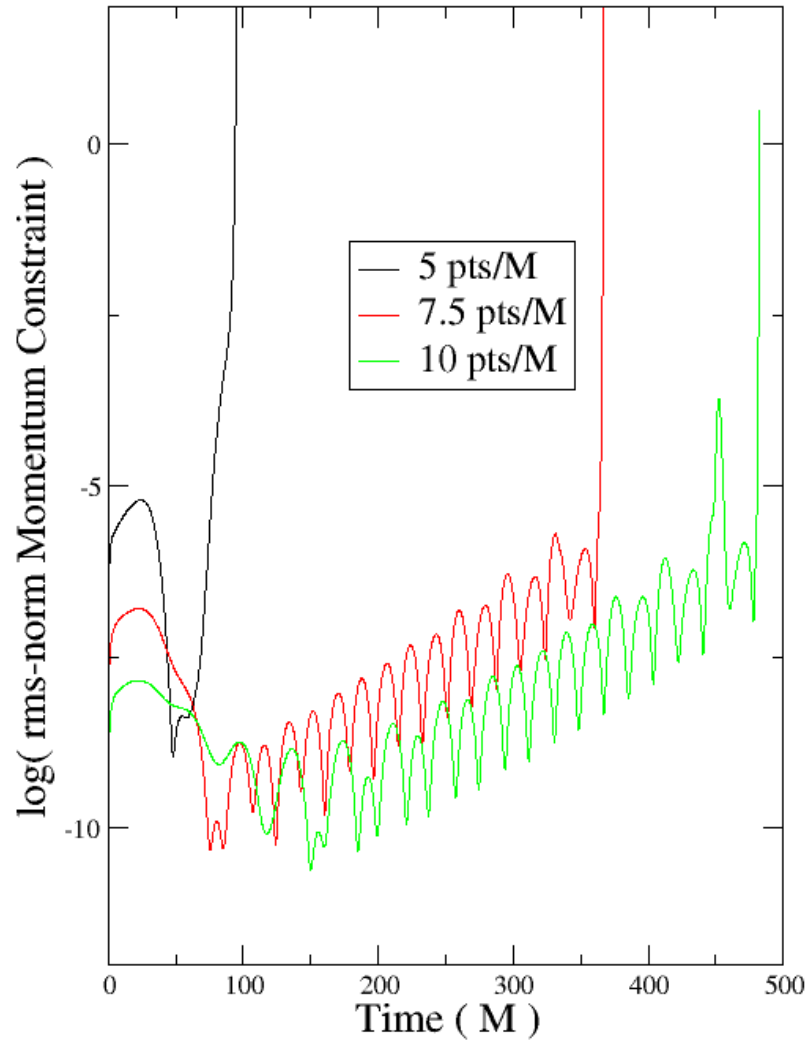
Figure 5.2: The log of the rms-norm for the momentum constraint C^r as a function of time for the same cases as in Figure 5.1.
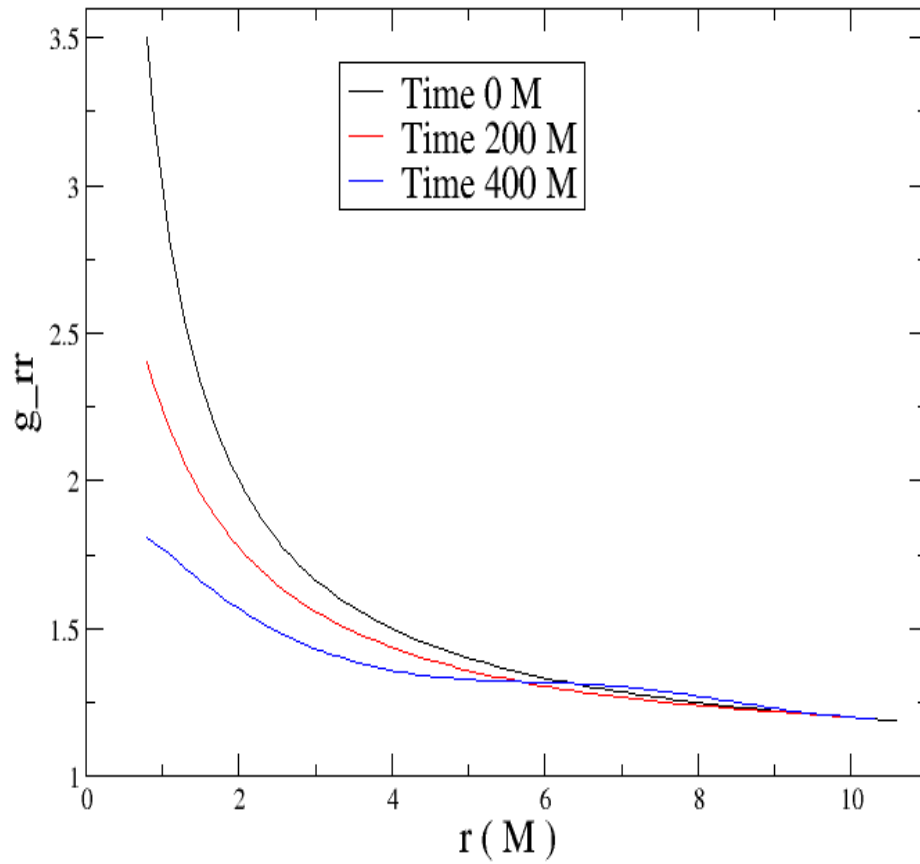
Figure 5.3: Snapshots of g_{rr} as a function of the radius at selected times. Taken from the 10 pts/M simulation seen in Figures 5.1 and 5.2.
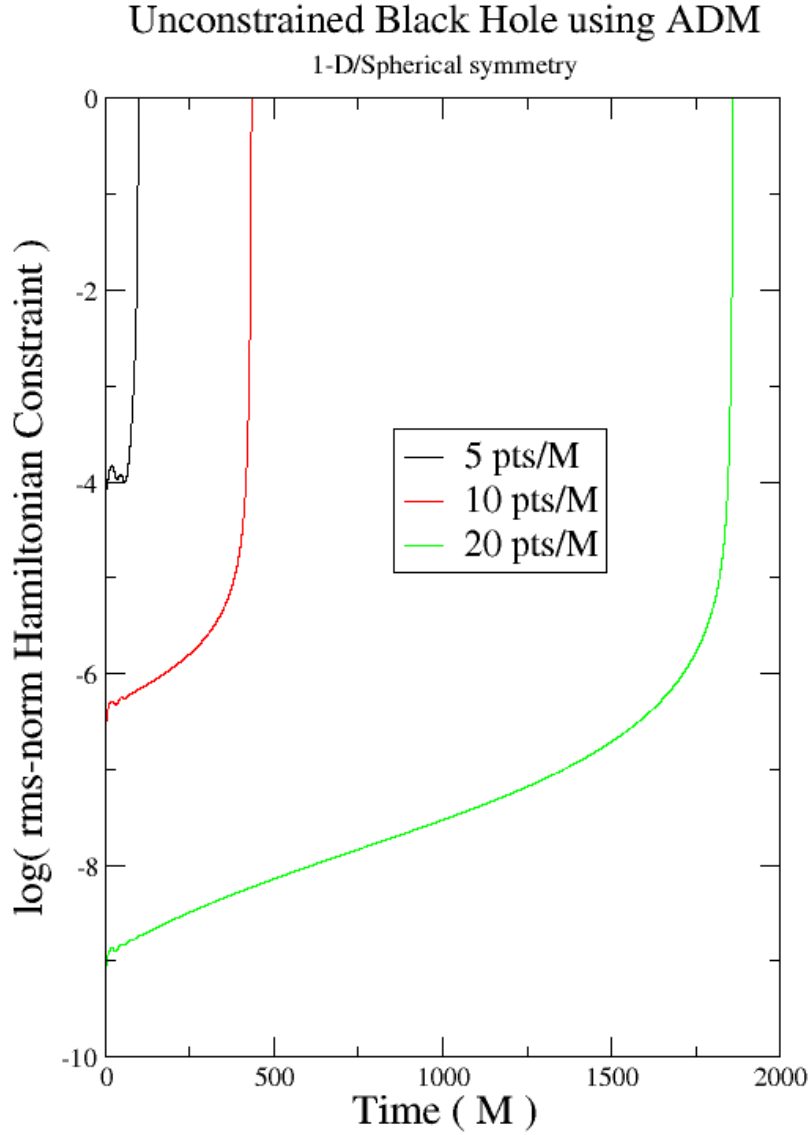
Figure 5.4: The log of the rms-norm for the Hamiltonian constraint violation as a function of time for an unconstrained 1-D/spherically symmetric black hole evolution using ADM. The domain of the simulation was $r = 0.8M \ldots 10.6M$ and the lapse function was densitized with $n = 2$ (see Eq. (4.23)). Results at three resolutions are presented.

Figure 5.5: The log of the rms-norm for the Hamiltonian constraint violation as a function of time for an unconstrained black hole evolution using ADM. The domain of the simulation for each of the three spatial axes was $[-10M \ldots 10M]$ and the lapse function was analytic. The excision radius was $0.85M$. Results at two resolutions are presented.
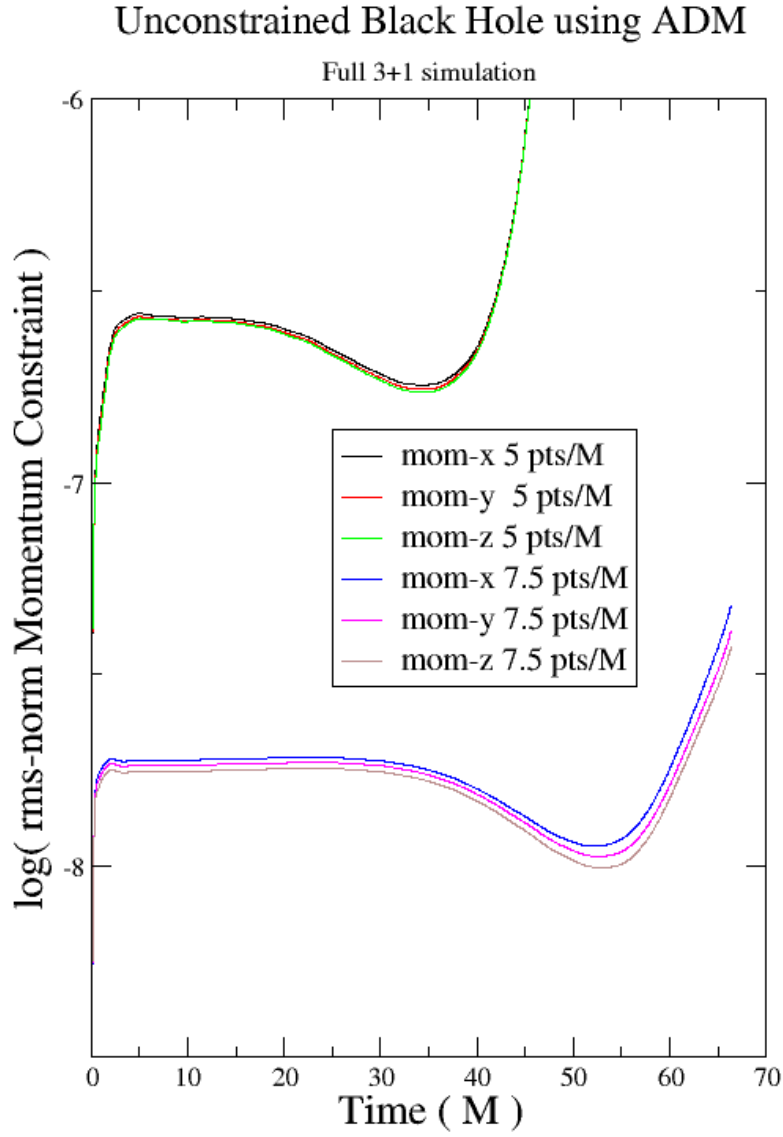
Figure 5.6: The log of the rms-norm for the momentum constraints C^i as a function of time for the same cases as in Figure 5.5.

Using a densitized lapse in a full unconstrained, unmodified ADM evolution aggravates the instability when compared with the analytic lapse case; no stability benefit was found. Figure 5.8 shows the l_2-norm of the Hamiltonian constraint plotted as a function of time for a simulation using a densitized lapse with varying choice of exponent (see section 4.8).

5.2 Modified ADM

A simple way to control the growth of the constraints and unstable behavior observed in an unconstrained evolution of a black hole is to modify the standard ADM equations by subtracting terms proportional to the constraint violations from the right hand side of the $\dot{K}$ equations, Eq. (2.23). This idea has been applied before in magnetohydrodynamics codes to control the $\nabla \cdot B = 0$ constraint by using the constraint violation in a source term for the evolution equations [28]. In numerical relativity, constraint subtraction techniques have been extensively explored for the Baumgarte-Shapiro-Shibata-Nakamura (BSSN) formulation [48]. Recently, there have been suggestions to incorporate spatial derivatives of the constraints in the evolution equations [49]. Exploring the parameter space to find straightforward constraint subtractions that produce long-lived unconstrained evolutions is the simplest approach to controlling the unstable behavior seen with the standard ADM equations.

Using quantities expressing the size of the constraint equations' violation, Eqs. (2.28–2.29), a list of potential constraint subtractions terms was constructed:

$$\alpha g_{ij} C^0$$

$$\alpha K_{ij} C^0$$

$$\alpha g_{ij} C^k \beta_k.$$

Extensive testing, first in spherical symmetry and later in full 3-D, resulted in the
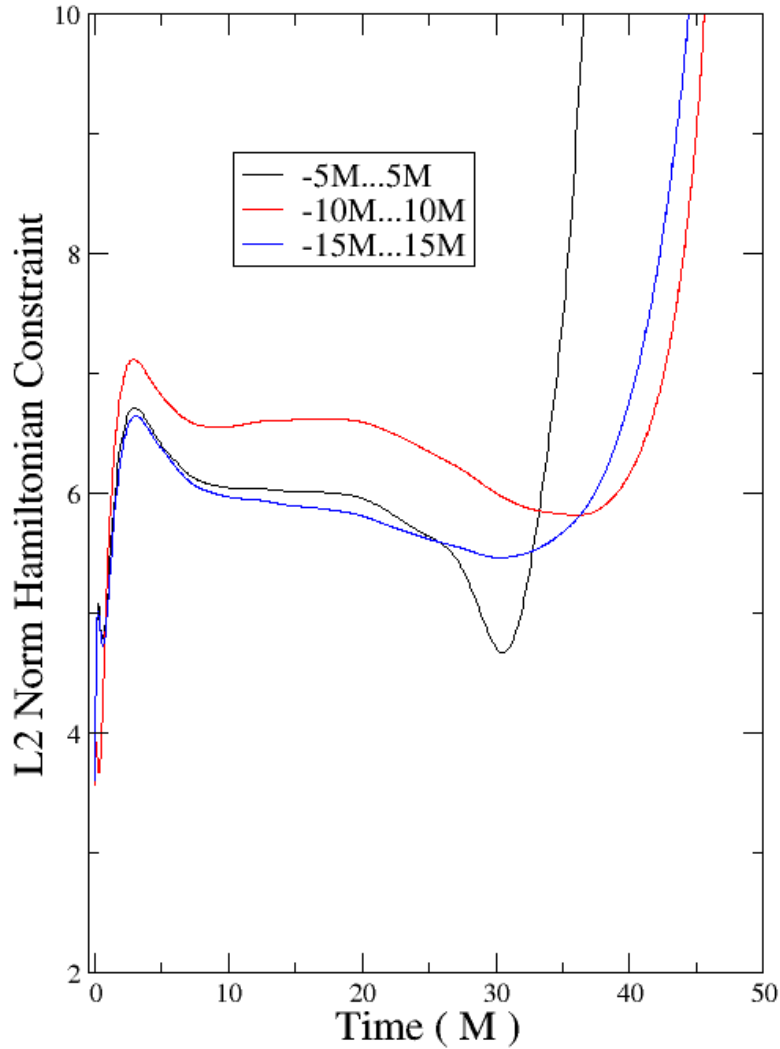
Figure 5.7: The l_2-norm for the Hamiltonian constraint violation as a function of time for three unconstrained black hole evolutions using ADM performed on different computational domain sizes. Each had a resolution of $M/5$, an excision radius of $0.85M$, and used the analytic lapse. The spatial domains explored were $[-5M \ldots 5M]$, $[-10M \ldots 10M]$, and $[-15M \ldots 15M]$.
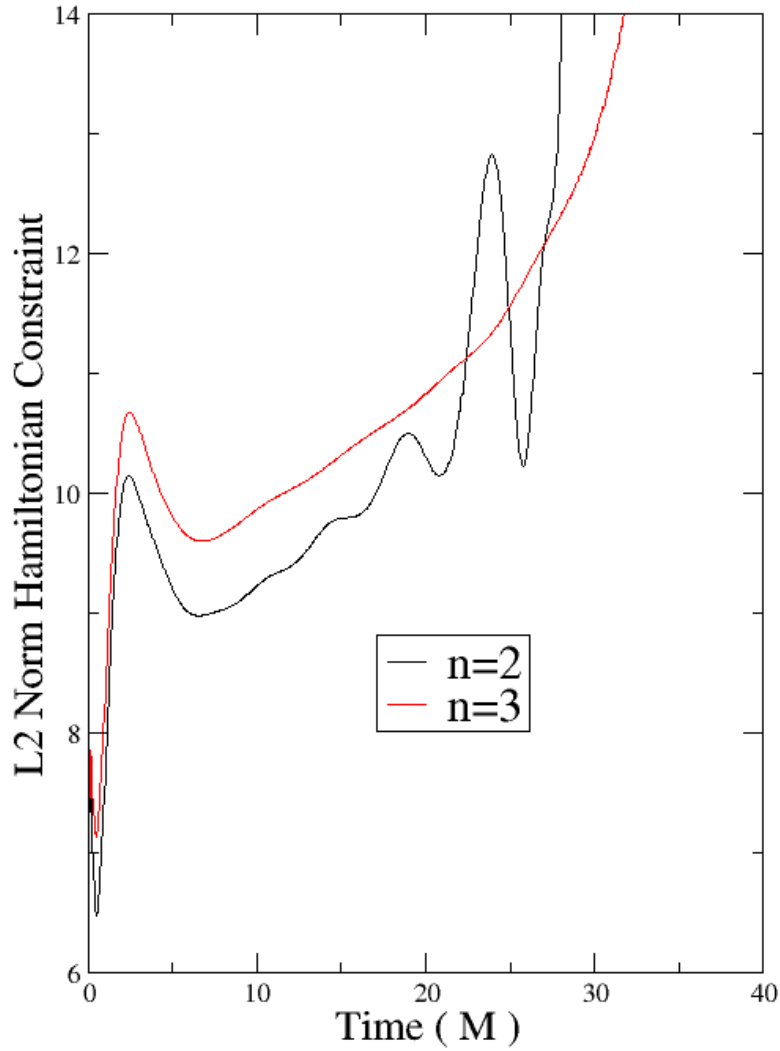
Figure 5.8: The l_2-norm for the Hamiltonian constraint as a function of time for two unconstrained black hole evolutions using ADM with a densitized lapse. Each had a resolution of $M/5$, an excision radius of $0.75M$, and a computational domain of $[-10M \ldots 10M]$ in each spatial direction. The factor n used in the densitized lapse took a value of either 2 or 3 (see Eq. (4.23)).

following constraint subtraction:

$$-0.464\alpha g_{ij}C^0 - 0.36\alpha K_{ij}C^0. \tag{5.1}$$

When subtracting these terms from the right hand side of the $\dot{K}$ equations, drastic improvements in simulation lifetime resulted. In Figure 5.9, the log of the rms-norm for the Hamiltonian constraint violation in simulations of an isolated, non-spinning black hole is presented. These simulations compare, at two different resolutions, the effect of constraint subtraction on the stability of a single hole evolution. The momentum constraints for these simulations are plotted in Figure 5.10.

While constraint subtraction remarkably improves the lifetime of single black hole in an unconstrained evolution, it does not make the evolution stable. This is most apparent when making the spatial domain of the simulation larger, which usually makes a black hole simulation more unstable. In Figure 5.11 the l_2-norms are plotted for three different unconstrained evolutions using the constraint subtraction in Eq. (5.1) and performed on varying spatial domains. The $[-10M \ldots 10M]$ and $[-15M \ldots 15M]$ domain simulations in Figure 5.11 can be directly compared with Figure 5.7, which displays the same evolutions performed without constraint subtraction.

The blow up in the fields for these runs is most pronounced near the excision region, as seen in Figures 5.12, 5.13, 5.14, and 5.15, which show the difference in g_{xx} from the analytic value at time $400M$ and $800M$ for the $[-15M \ldots 15M]$ simulation presented in Figure 5.11. Figure 5.12 shows the $z = 0$ plane of the difference between the analytic and numeric values of g_{xx} at time $400M$. Figure 5.13 shows the $z = 0$ plane of the difference at time $800M$ using the same color map as in Figure 5.12. Figures 5.14 and 5.15 show the full 3-D difference between analytic and numeric values at time $800M$ using a color map that extends over the entire range of the difference.

A difficulty in using constraint subtraction to improve the lifetime of a simu-
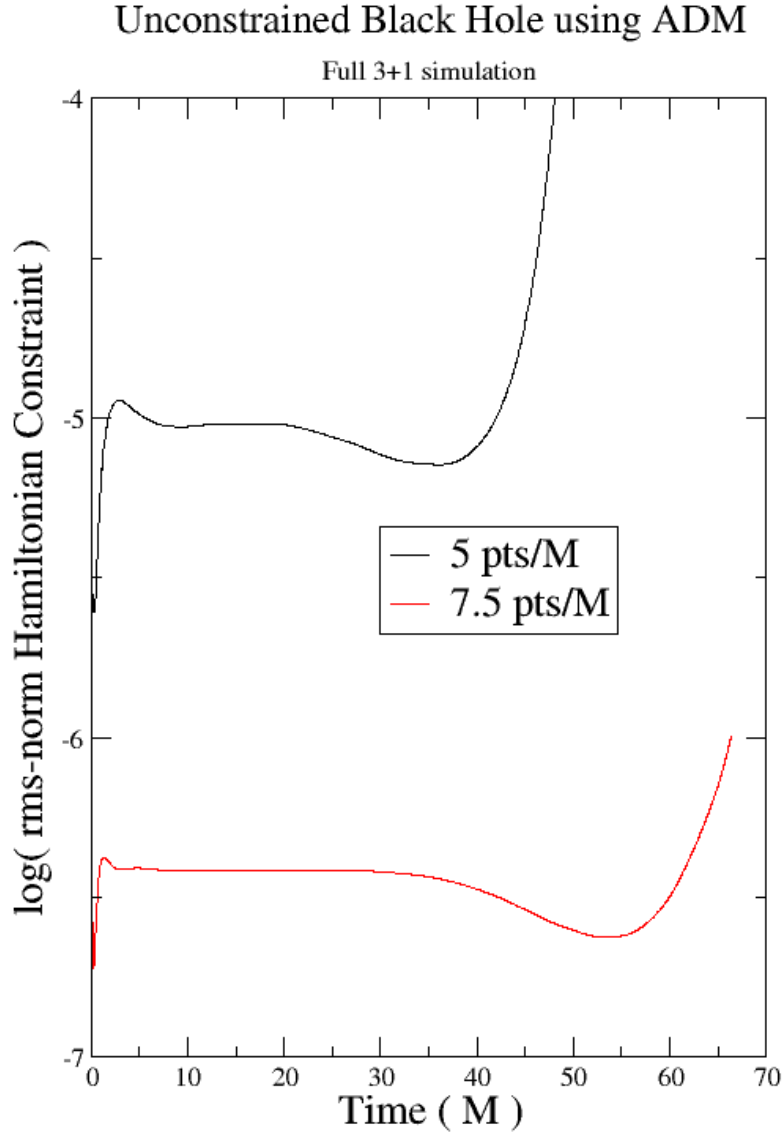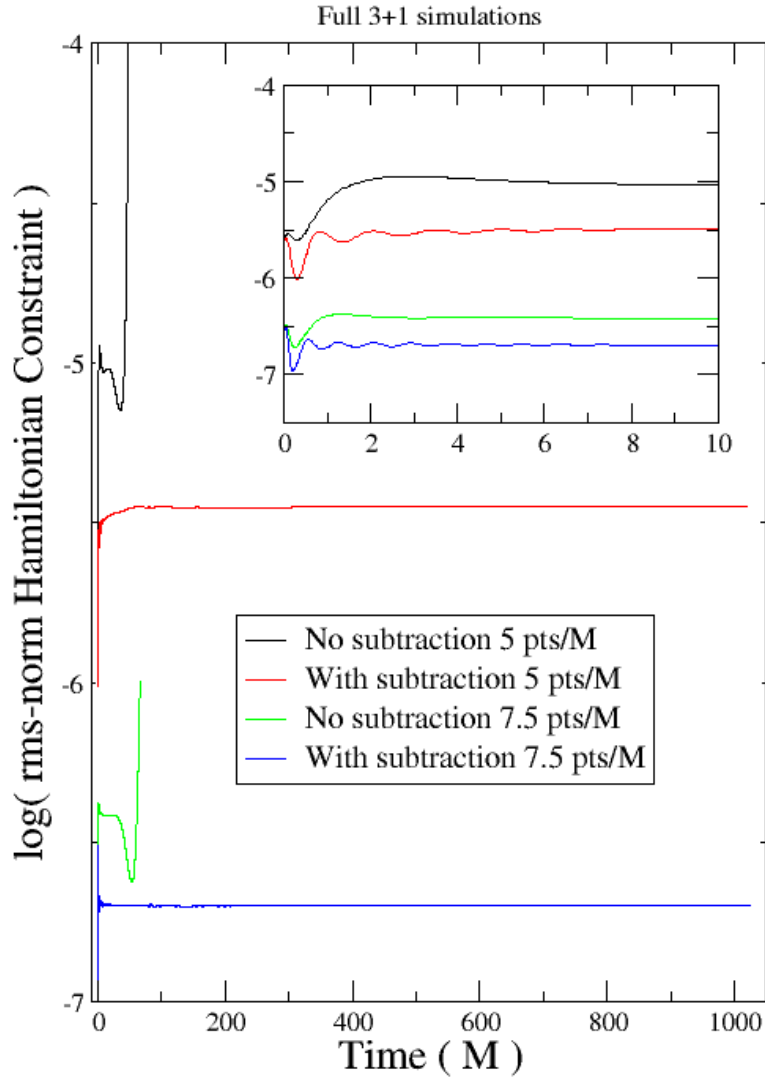
Figure 5.9: The log of the rms-norm for the Hamiltonian constraint violation as a function of time for four unconstrained black hole evolutions using ADM with and without constraint subtraction at different resolutions. Each had a spatial domain of $[-10M \ldots 10M]$, used an excision radius of $0.85M$, and used the analytic lapse. The inset provides a view of the constraint behavior early in the evolution for each run. The constraint subtraction employed is that specified in Eq. (5.1).
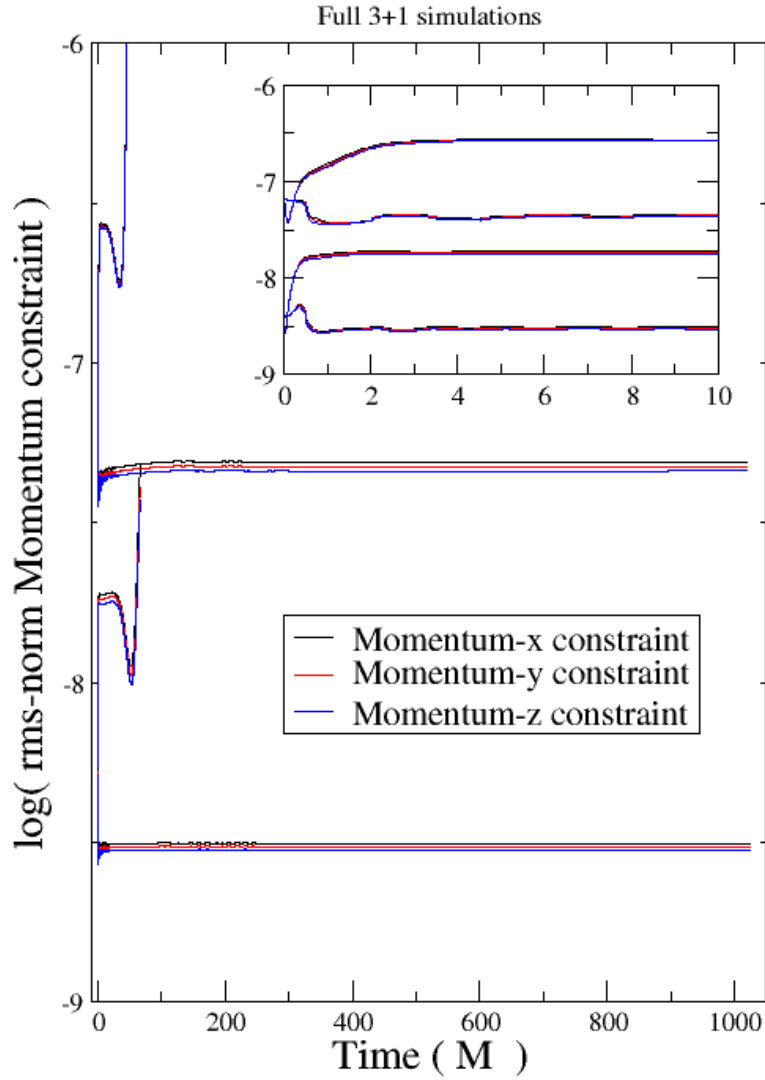
Figure 5.10: The rms-norm for the momentum constraints as a function of time for the same simulations as presented in Figure 5.9. The inset provides a view of the constraint behavior early in the evolution for each run. These simulations use no special symmetries and are full 3-D simulations. The constraint subtraction employed is that specified in Eq. (5.1).
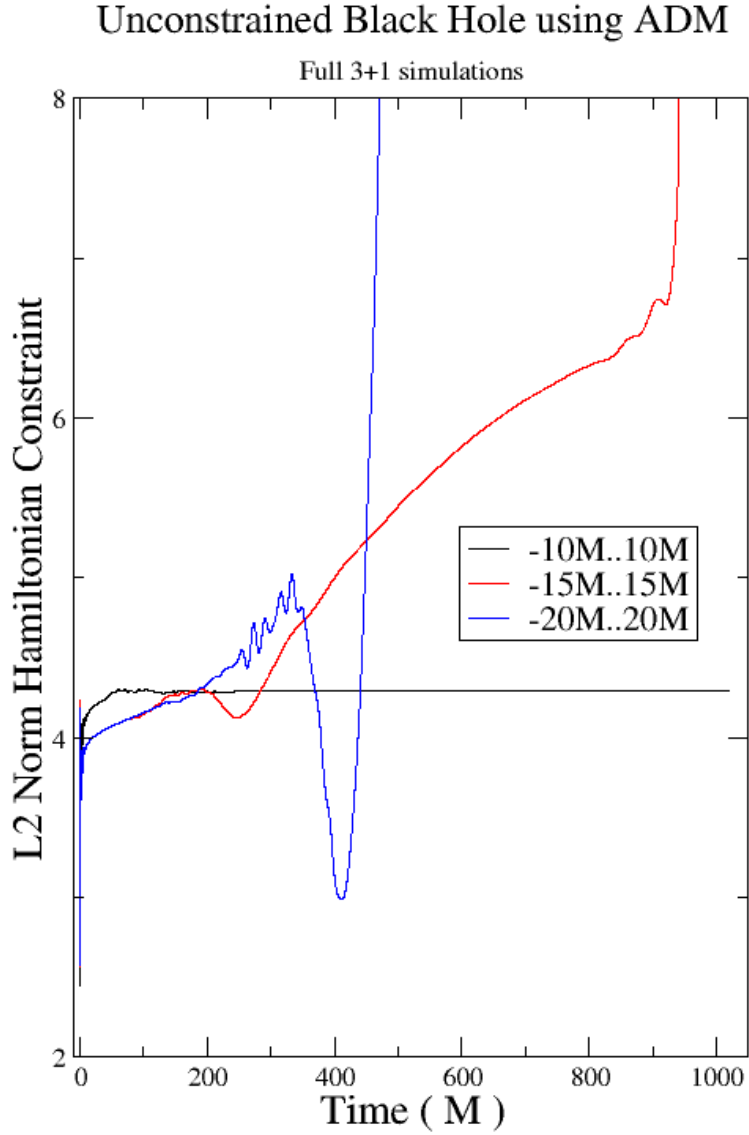
Figure 5.11: The l_2-norm of the Hamiltonian constraint for three unconstrained black hole simulations using ADM with constraint subtraction and performed on varying domain sizes. Each had a resolution of $M/5$, used an excision radius of $0.85M$, used the analytic lapse, and used the constraint subtraction specified in Eq. (5.1).
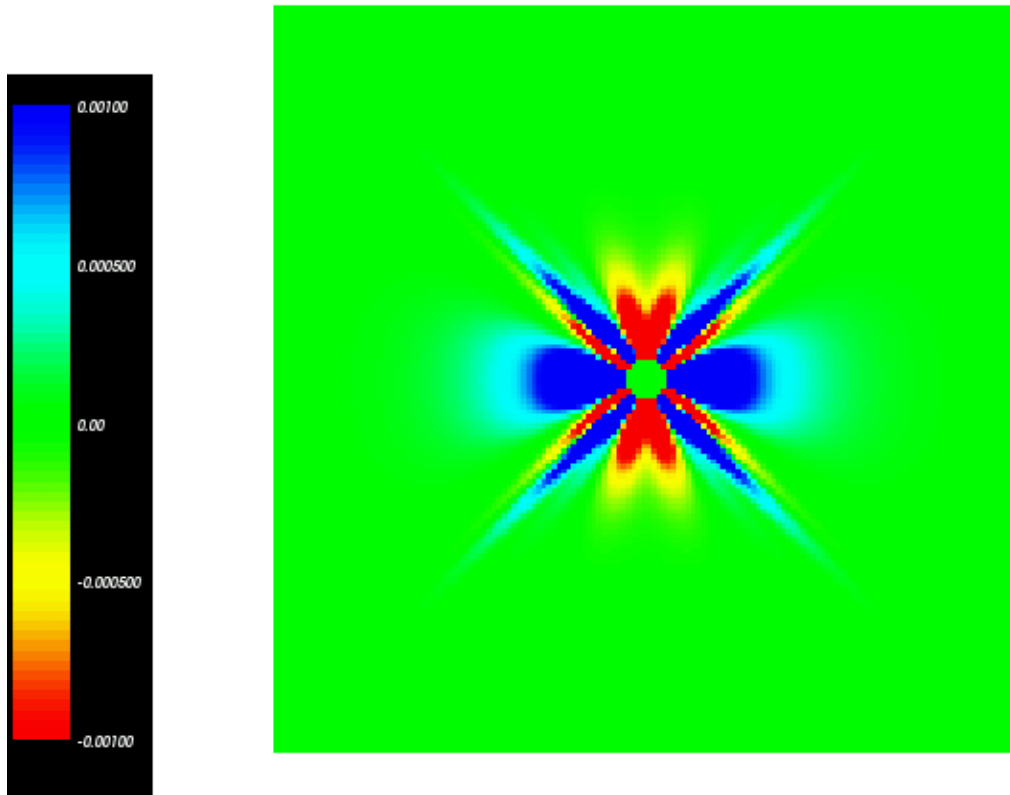
Figure 5.12: The $z = 0$ plane showing the difference between the analytic and numerical values for g_{xx} at time $t = 400M$ for the $[-15M \dots 15M]$ simulation with constraint subtraction, presented in Figure 5.11.
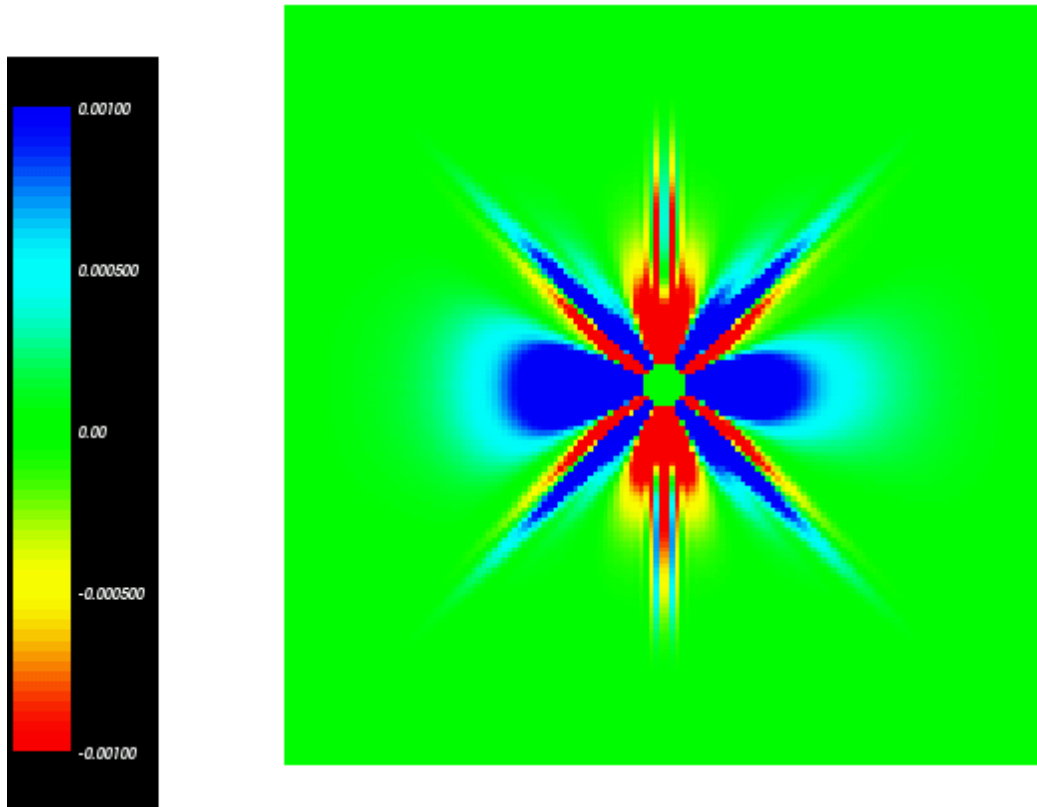
Figure 5.13: The $z = 0$ plane showing the difference between the analytic and numerical values for g_{xx} at time $t = 800M$ for the $[-15M \ldots 15M]$ simulation with constraint subtraction, presented in Figure 5.11.
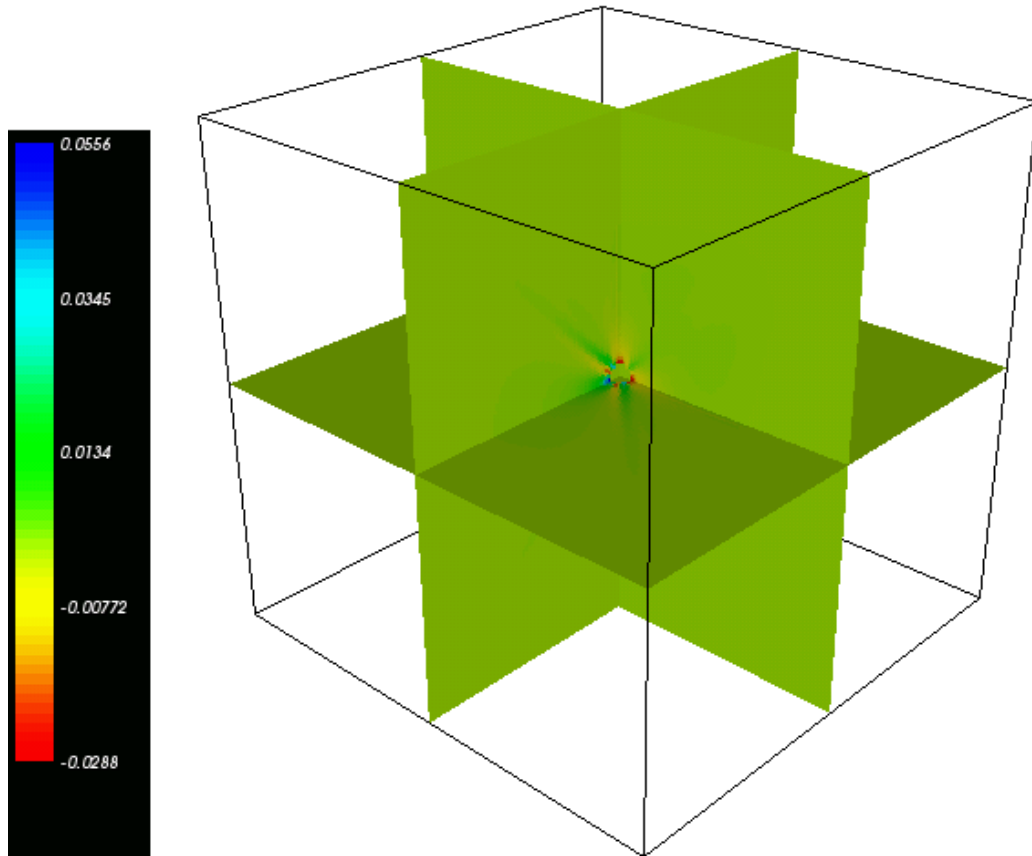
Figure 5.14: The difference between the analytic and numerical values for g_{xx} at time $t = 800M$ for the $[-15M \ldots 15M]$ simulation with constraint subtraction, presented in Figure 5.11. The difference is most pronounced near the mask. A close-up view of the error near the mask is shown in Figure 5.15.
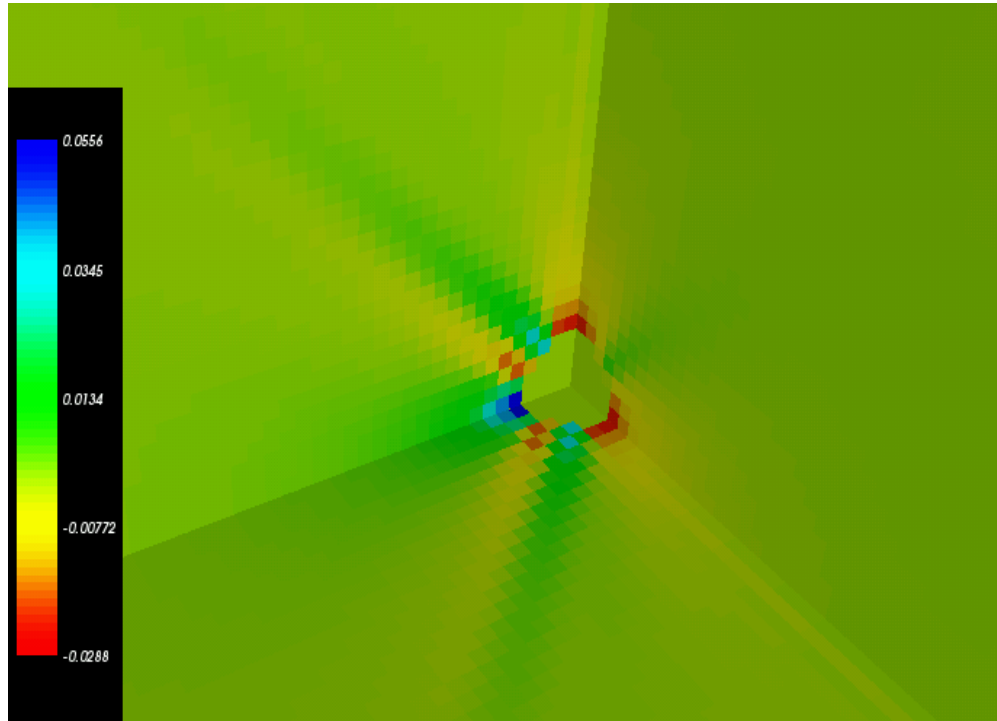
Figure 5.15: The difference between the analytic and numerical values for g_{xx} at time $t = 800M$ for the $[-15M \ldots 15M]$ simulation with constraint subtraction, presented in Figure 5.11. The difference is most pronounced near the mask.

lation is the sensitivity to the subtraction; small variations from the best subtraction found, Eq. (5.1), result in large differences in simulation lifetime. To give an idea of the sensitivity involved with constraint subtraction, Figure 5.16 plots the l_2-norm of the Hamiltonian constraint violation for several runs employing constraint subtraction slightly different from that found in Eq. (5.1).

It is difficult to relate constraint subtractions between different formulations of the Einstein equations. The best constraint subtraction found in the experiments presented here is relatively small, less than 0.5. Constraint subtraction in other approaches can often be larger, ~ 12, as is the case in Scheel et. al. [50]. Constraint subtraction using BSSN can involve subtracting constraints from the right hand side of the $\dot{g}$ equations in addition to the $\dot{K}$ equations [51]. The difficulty in relating constraint subtractions between formulations, the necessity of tuning the subtractions, and the difficulty in tuning the subtractions for simulations with ever larger spatial domains combine to make constraint subtraction a less than desirable option in numerical simulation.

5.3   GFR

Evolving a nonrotating Kerr-Schild black hole using unconstrained GFR has proven difficult. This may be due to several reasons. The evolution scheme used for these studies, Adams-Moulton (section 4.2), does not take advantage of the flux conservative form in which the formulation is written. Also, the parameter space in the formulation is large enough to complicate efforts to adequately explore it. Regardless of these issues, however, unconstrained 3-D simulations using GFR have a slightly longer lifetime than the analogous unconstrained, unsubtracted ADM case. 1-D GFR simulations, in contrast, do not have a longer lifetime than the analogous ADM cases.

In Figure 5.17, the rms-norm of the Hamiltonian constraint violation is plot-
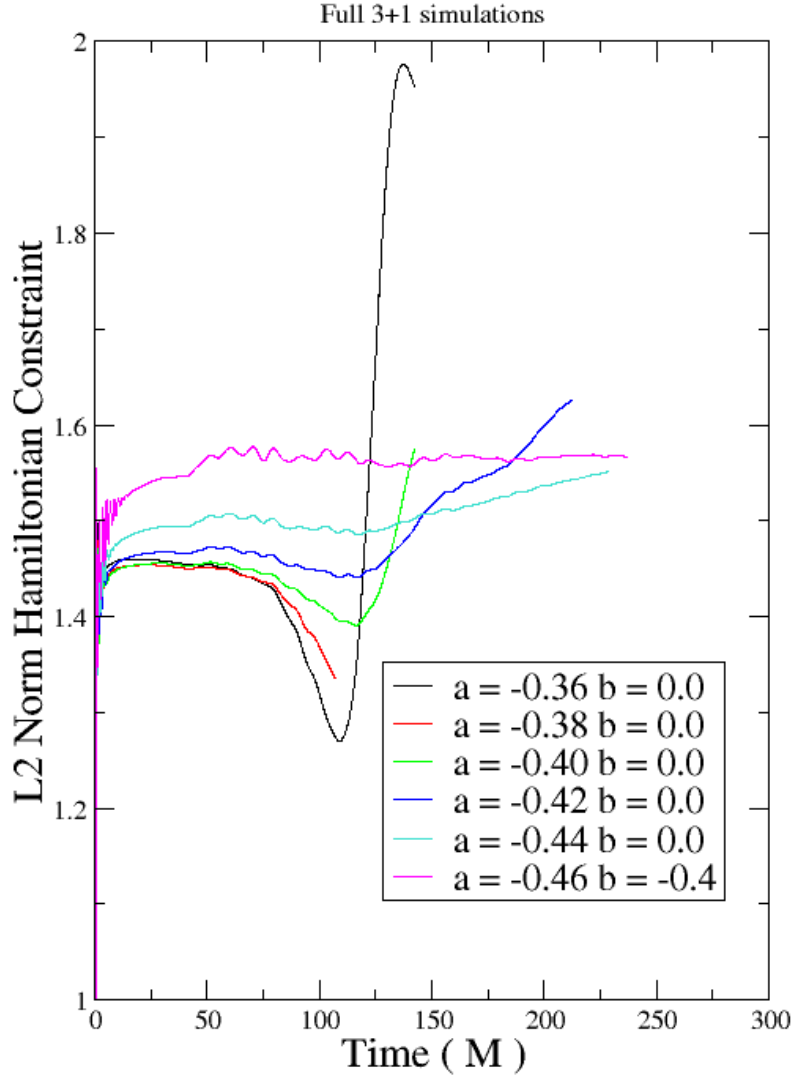
Figure 5.16: The l_2-norm of the Hamiltonian constraint violation for several uncon-strained evolutions performed on a domain of $[-10M \ldots 10M]$ using a resolution of $M/5$ and the analytic lapse. The excision radius in these simulations was $1.0M$. The legend indicates the specific subtraction employed by using the letters 'a' and 'b' to stand for the subtraction coefficients: $+\text{a}\,\alpha g_{ij}C^0 + \text{b}\,\alpha K_{ij}C^0$. The optimal subtraction found was $-0.464\alpha g_{ij}C^0 - 0.36\alpha K_{ij}C^0$.

ted as a function of time for several unconstrained simulations of a Kerr-Schild black hole with spherical symmetry. The domain for these simulations was $[0.8M \ldots 10M]$ with a resolution of $M/5$. The γ and Θ parameter values were chosen according to Eq. (2.38) to ensure physically realistic characteristic speeds.

By choosing GFR parameters $\eta = 0$ and $\gamma = 0$, the first-order form of the ADM equations results. This can be directly compared to the raw ADM cases previously presented in section 5.1. In Figure 5.18, the log of the rms-norm for the Hamiltonian constraint violation is plotted as a function of time for a Kerr-Schild black hole simulation performed at three resolutions with spherical symmetry. The spatial domain was $[-0.8M \ldots 10M]$. The lapse in this case, as with all GFR simulations, was densitized. These simulations can be directly compared with results from the standard ADM form, performed with a densitized lapse and spherical symmetry, presented in Figure 5.4, which performed much better.

In Figure 5.19 the l_2-norm of the Hamiltonian constraint violation is plotted as a function of time for two full $3 + 1$ simulations using $\eta = 0.5$ and $\eta = 0.85$ values. The simulations evolved a nonrotating Kerr-Schild hole on a spatial domain of $[-10M \ldots 10M]$ with a resolution of $M/5$. Just like the spherically symmetric case, the γ and Θ parameters were chosen according to Eq. (2.38) to ensure the system has physically realistic characteristic speeds. These plots can be compared with the ADM cases in Figure 5.5. No significant improvement was seen in the GFR cases.
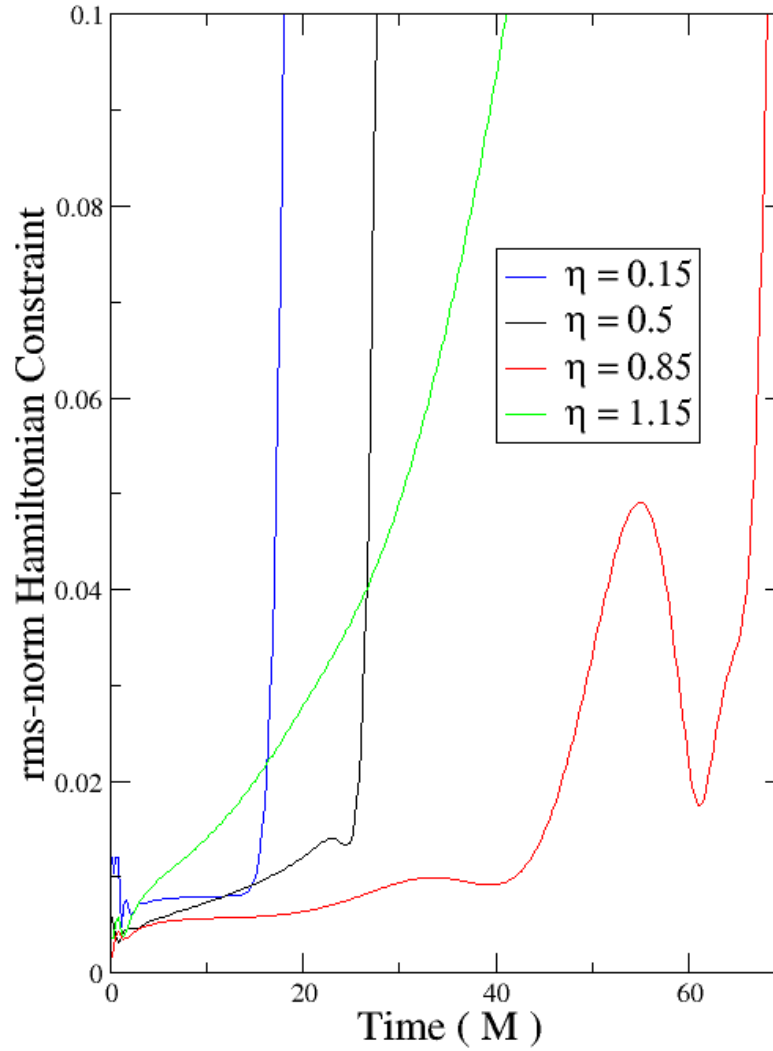
Figure 5.17: The rms-norm of the Hamiltonian constraint violation as a function of time for several unconstrained simulations using GFR with spherical symmetry. The simulations evolved a nonrotating Kerr-Schild black hole on a spatial domain of $[0.8M\ldots 10M]$ with a resolution of $M/5$. Parameters γ and Θ were determined by Eq. (2.38).
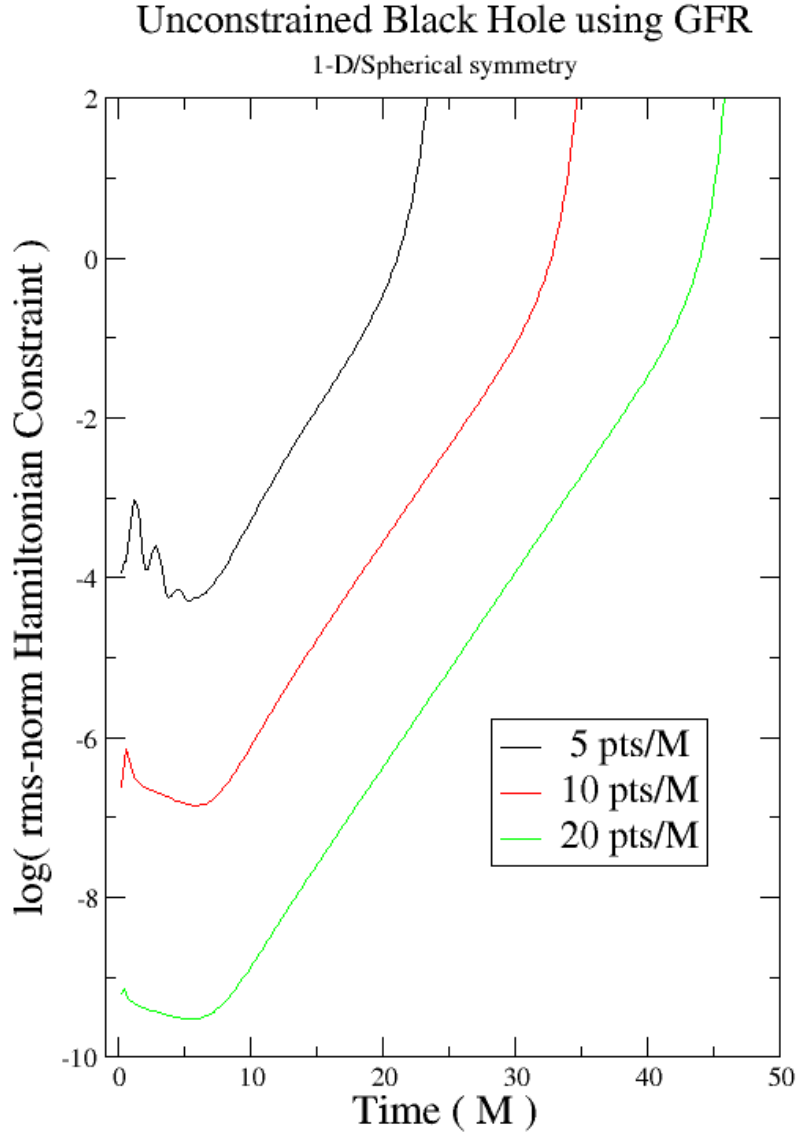
Figure 5.18: The log of the rms-norm for the Hamiltonian constraint violation as a function of time for three unconstrained simulations using GFR with spherical symmetry. The simulations evolved a nonrotating Kerr-Schild black hole on a spatial domain of $[0.8M \ldots 10M]$ at three different resolutions with GFR parameters corresponding to the first-order form of the ADM equations, $\eta = 0$ and $\gamma = 0$. Compare this with the standard form results for the same simulation, Figure 5.4.
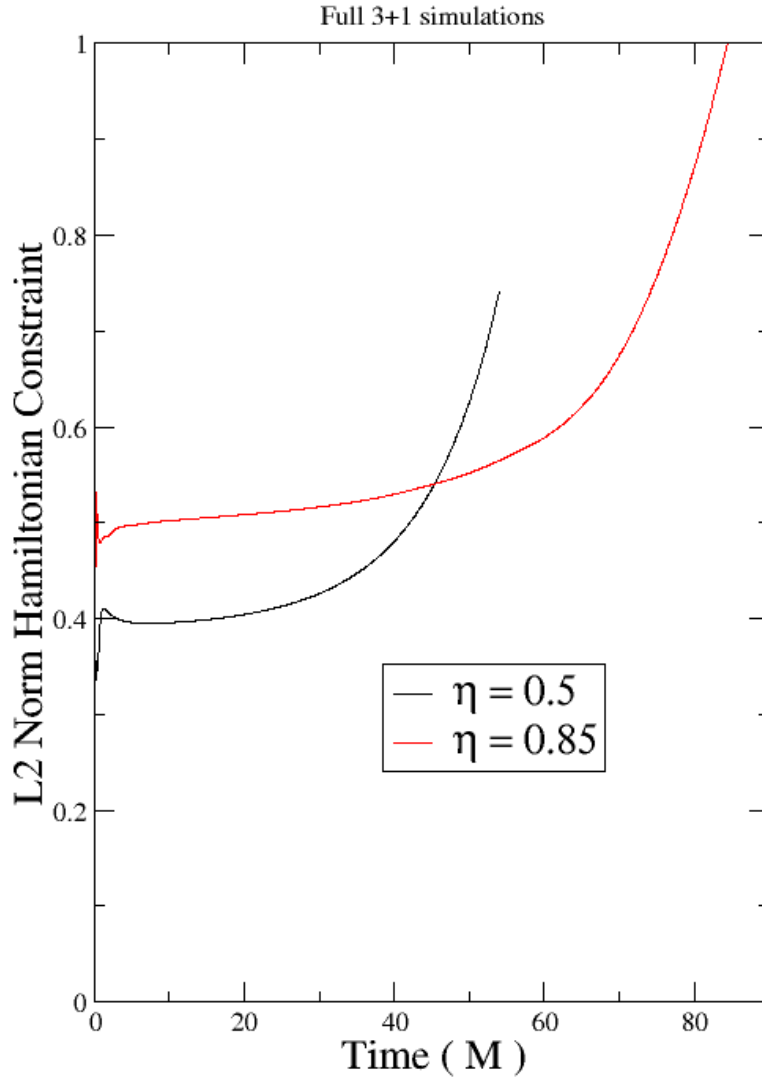
Figure 5.19: The l_2-norm of the Hamiltonian constraint violation as a function of time for two unconstrained simulations using GFR. The simulations evolved a nonrotating Kerr-Schild black hole on a spatial domain of $[-10M \ldots 10M]$ with a resolution of $M/5$ using GFR parameters of either $\eta = 0.5$ or $\eta = 0.85$. Parameters γ and Θ were determined by Eq. (2.38). The excision radius was $0.75M$.

Chapter 6

Constrained Single Black Hole Spacetimes

Constrained evolution consists of periodically solving the constraints in developing a simulated spacetime. Evolved fields are periodically used as background fields for solving the potentials ϕ and w^i appearing in the conformal transverse-traceless decomposition (see Eqs. (3.5–3.6)) and the dynamic variables are subsequently updated by the result (see Eqs. (3.2–3.3)).

The guiding principle behind this approach to constrained evolution is found in a statement by G. Tóth: "Exact solution of the constraints to round off precision is not necessary. It is sufficient to solve the problem to a particular accuracy that is small relative to the error generated in one timestep" [28]. Consequently, the constraint solves take up an acceptably small percentage of the overall computation time for any given problem. Further, the constraint violations will be non-zero throughout the course of a constrained evolution even though the constraints are being solved. To ensure that the simulations are indeed solving the Einstein equations, an independent residual evaluator is used for full 3+1 simulations to calculate all the components of the Einstein tensor and subsequently verify their convergence.

This chapter will explore the influence of constrained evolution using the standard ADM and GFR formulations. A brief historical review of constrained evolution will be presented first. Unconstrained and constrained evolutions will then be presented for comparison, first in spherical symmetry and later without. All the simulations presented in this chapter place the center of the black hole at $r = 0$ in the computational grid.

6.1 Brief History of Constrained Evolution

The idea of constrained evolution is not new. Most examples of constrained evolution in relativity employ some symmetry and solve only the constraints relevant to the system. Constrained evolution in axial symmetry has been studied extensively. One of the earliest works in axisymmetry, reported by R. F. Stark and T. Piran in 1985 [52], solved only the Hamiltonian constraint while evolving a collapsing polytrope. There are other examples of such partially constrained evolutions [53], but most examples in the literature solve both the momentum and Hamiltonian constraints during the course of an evolution [54] [55] [56] [57] [58] [59]. Furthermore, most 2-D constrained simulations were what M. Choptuik [60] calls *fully constrained*. In these simulations a specific gauge is chosen, and only the remaining dynamical mode is evolved. Every other variable is solved, typically by solution of elliptic equations, in terms of the minimal evolved set.

There are very few examples of constrained evolution performed in full 3-D. Preliminary results of constrained evolution of isolated black holes on small domains were discussed by E. Schnetter [61]. Fully constrained simulations in 3-D are also being studied by S. Bonazzola et al. [62]. The simulations I present here are constrained in the sense that all four constraints are solved, but I do not use the gauge nor construct equations to eliminate variables from the problem.

The lack of examples of constrained evolution in 3-D is usually attributed

to the computationally demanding elliptic solves required periodically throughout an evolution. For the results presented in this thesis, the performance penalty incurred by solving the constraints is typically small because the constraints are never solved to round off precision. Increasing the frequency of the constraint solves can make constrained evolution impractical in terms of performance just as using extremely small Courant factors can make an unconstrained evolution impractical in terms of performance. However, neither of those remedies has been necessary in the constrained evolutions presented in this chapter.

6.2   Constrained Evolution in 1-D using ADM

Results presented in section 5.1 show the difficulty of evolving a nonrotating Kerr-Schild hole with the standard ADM formulation, even in spherical symmetry. Constraining the evolution changes this result considerably. In Figure 6.1, the Hamiltonian constraint violation for constrained and unconstrained 1-D/spherically symmetric evolutions are presented for simulations performed at two resolutions. The only relevent momentum constraint in spherical symmetry is shown in Figure 6.2. Consistent with the principle of solving to an accuracy that is small with respect to the error arising in one timestep, the potential ϕ is small throughout the constrained evolution. In Figure 6.3, the function $\phi - 1$ is plotted across the computational domain at various times in the evolution. In Figure 6.4, the unconstrained and constrained g_{rr} components are plotted at various times in the evolution.

As described in section 4.10, the potentials ϕ and w^i are set to trivial values at the inner and outer boundaries of the solve. Extensive experimentation reveals that placing the inner boundary of the solve at the excision region can trigger instabilities. Supplying a few buffer zones between the inner solve radius and the excision radius dramatically improves constrained evolution results both with and without spherical symmetry. Figure 6.5 displays a schematic of the inner and outer
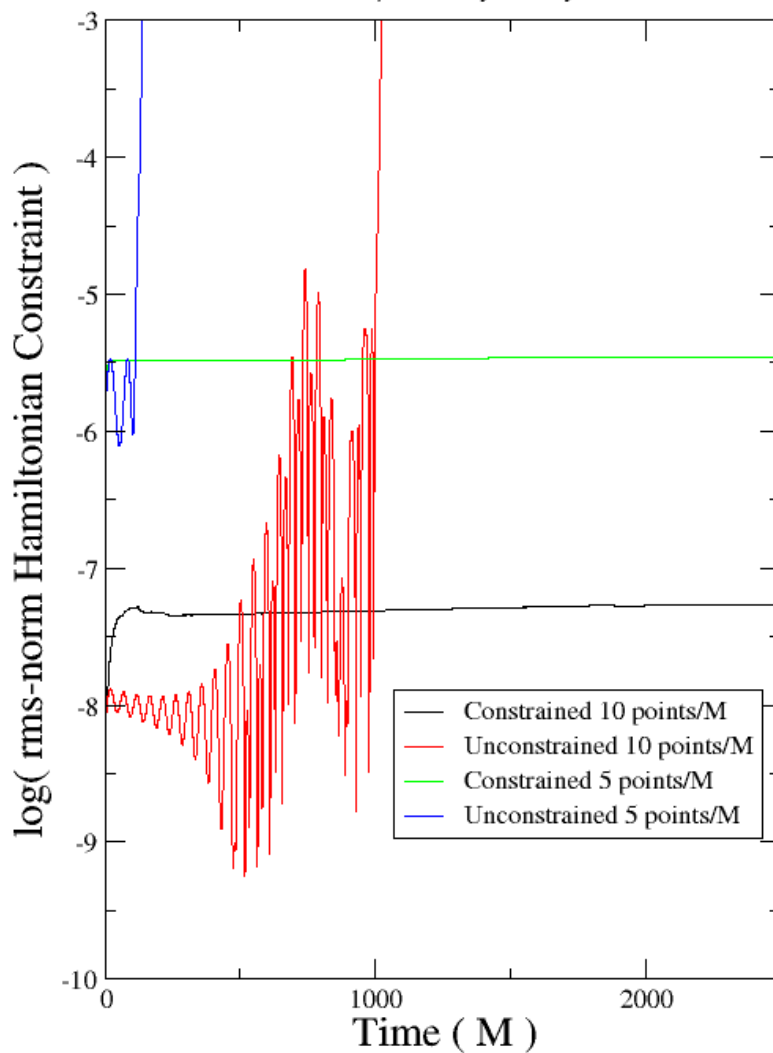
Figure 6.1: Simulations of nonrotating Kerr-Schild black holes comparing constrained and unconstrained evolutions in spherical symmetry. These plots show the log of the rms-norm for the Hamiltonian constraint violation in simulations performed with 5 points/M and 10 points/M on domains of $[0.8M \ldots 250M]$. The lapse was densitized with $n = 3$. The constraints were solved every $0.2M$ wherever $r \geq 2$ in the constrained cases.
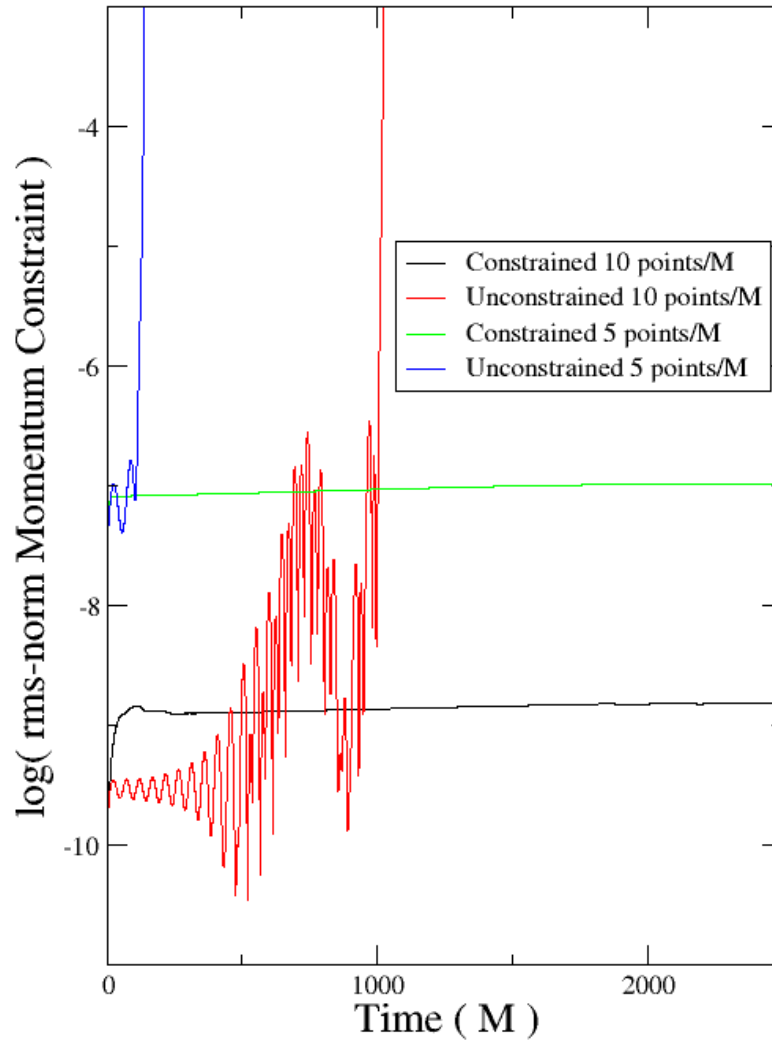
Figure 6.2: The log of the rms-norm for the momentum constraint violation, C^r, in the simulations described in Figure 6.1.
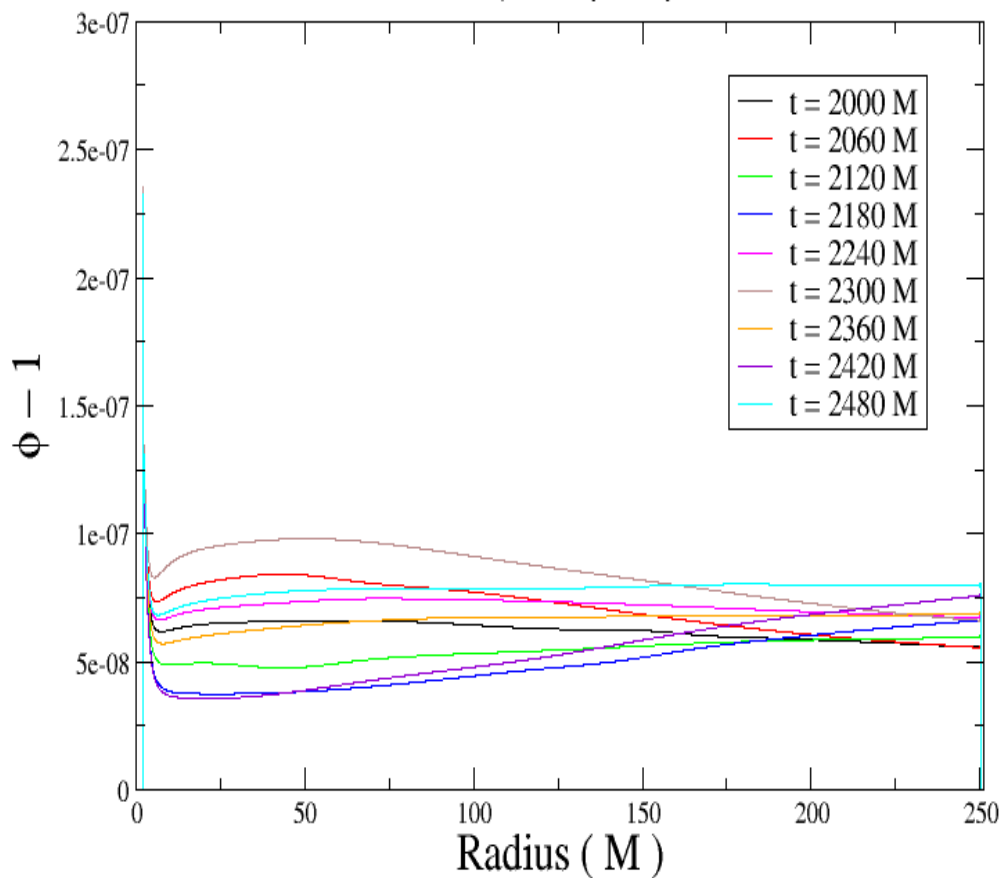
Figure 6.3: The function $\phi - 1$ is plotted here, where ϕ is the conformal factor for solving the Hamiltonian constraint in the higher resolution constrained evolution case presented in Figures 6.1 and 6.2. The function is plotted at various times to show how the constraint solver reacts to control constraint violating modes.
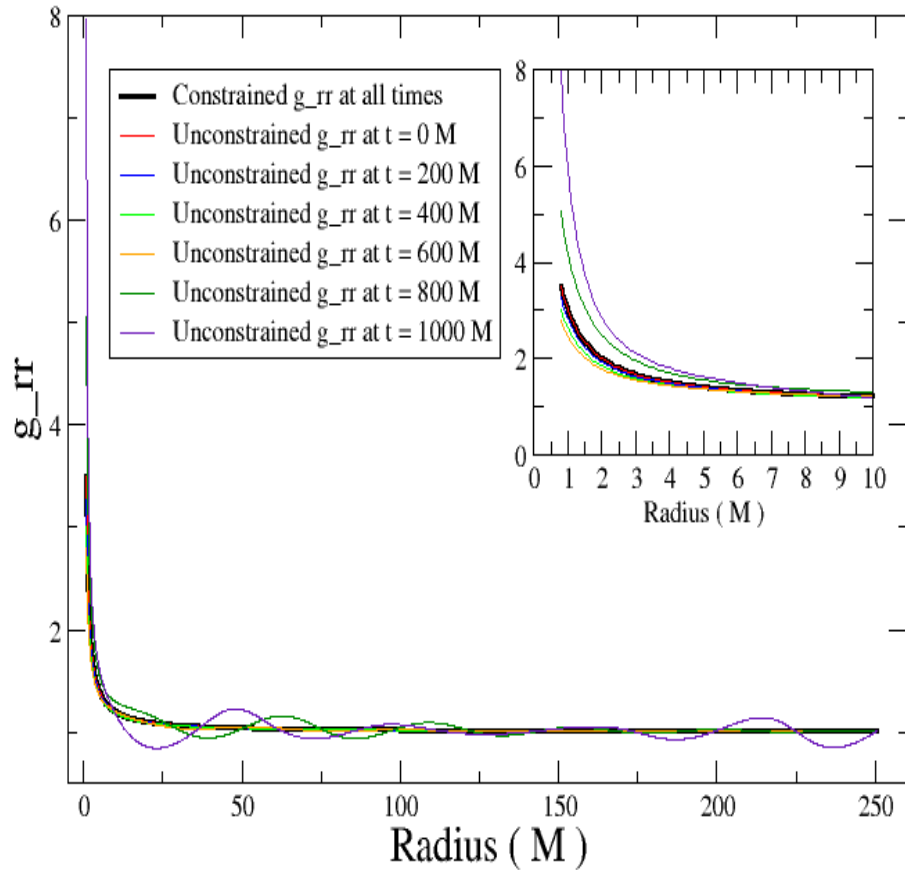
Figure 6.4: The metric component g_{rr} is plotted here as a function of r at several times for the higher resolution constrained and unconstrained evolutions presented in Figures 6.1 and 6.2. The inset shows a view of the g_{rr} close to the excision region. For the constrained case, g_{rr} does not visibly deviate from the initial value. For the unconstrained case, g_{rr} deviates significantly from the analytic value across the entire domain.

elliptic solve boundaries in relation to the excision region for a simulation with three spatial dimensions. Figure 6.6 plots the metric component g_{rr} as a function of radius at various times in two different 1-D/spherically symmetric constrained evolution simulations. These simulations compare solving the entire computational domain versus solving all except for a few zones next to the excision region. The same effect in simulations in full 3-D will be shown in section 6.3.

6.3 Constrained Evolution in 3-D using ADM

Evolutions using any type of symmetry, including spherical, are often artificially simple. Evolving in three spatial dimensions without using any symmetries is a better test case for constrained evolution of black hole spacetimes. Varying the spatial domain of 3-D evolutions in addition to varying the resolution constitutes a robust test of constrained evolution in 3-D. As has already been observed in unconstrained evolutions like those in Figure 5.11, making the spatial domain larger has the effect of making a simulation less stable. This remains the case in constrained evolution as well.

Small domains in 3-D evolutions are generally the easiest to stabilize using constrained evolution. They require very few computer resources and, due to the small domain size, their constraint violating modes are very easy to control with the constraint solver. In Figure 6.7, constrained versus unconstrained evolutions are compared in evolving a nonrotating Kerr-Schild black hole on a spatial domain of $[-3M \ldots 3M]$ in full 3-D. Even though these simulations used the analytic lapse, which generally makes a simulation more unstable, the constraint solver was able to control the constraint violating modes that cause the unconstrained evolution to go unstable very quickly.

Since constraint solving methods are not unique, it is not difficult to imagine that the constraint solver might control the growth of the constraints during a
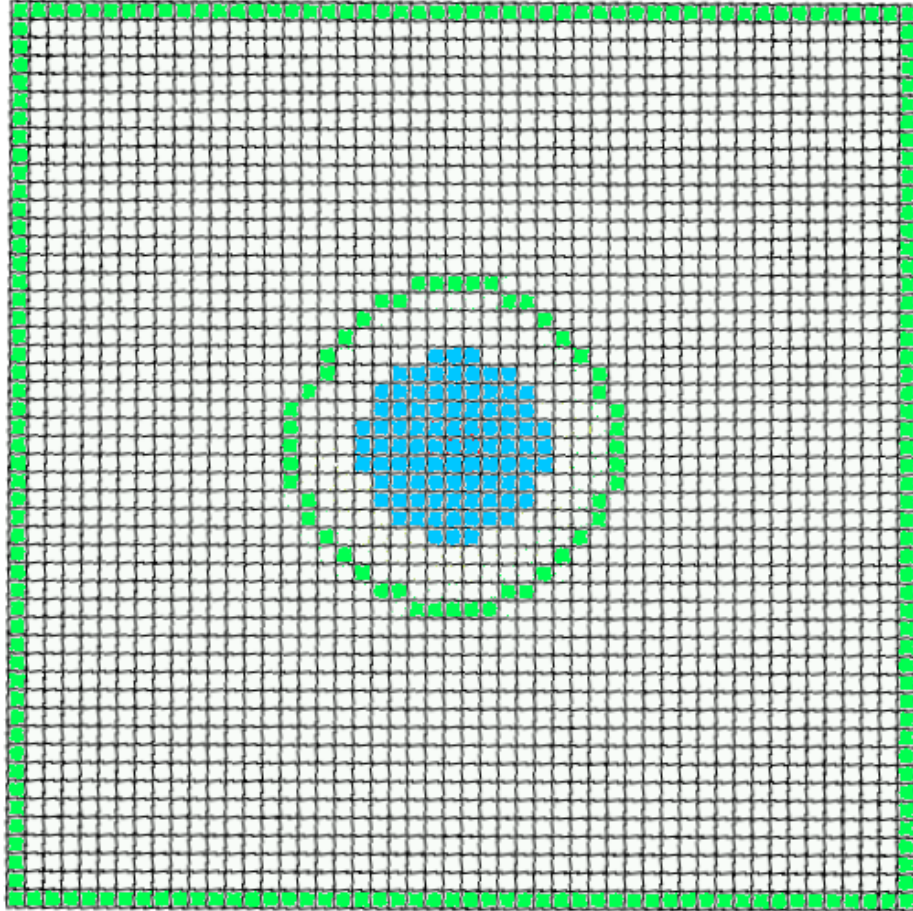
Figure 6.5: The boundary conditions for the elliptic solve, $\phi = 1$ and $w^i = 0$, are applied at the green zones. Experimentation reveals that providing a few buffer zones between the excision region, colored blue, and the inner solve boundary, colored green, dramatically improves a constrained evolution. See Figure 6.6. The evolved field values between the inner solve radius and the excision region are not constrained but rather determined by free evolution.
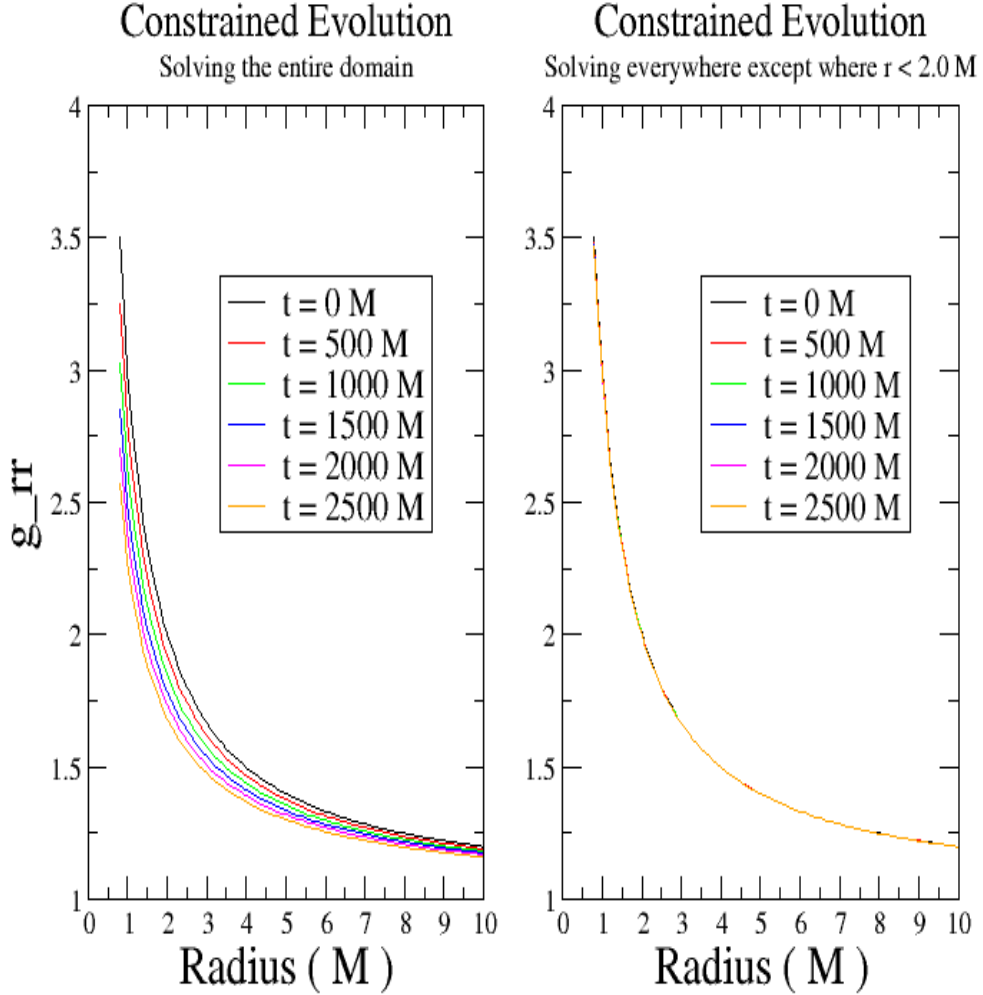
Figure 6.6: The metric component g_{rr} for two different constrained evolutions of a nonrotating Kerr-Schild black hole performed in 1-D/spherical symmetry, plotted here as a function of the radius. The domain of the simulations was $[0.8M \ldots 250M]$, though only $[0M \ldots 10M]$ is plotted here. The system was resolved with 10 points/M and the lapse was densitized with $n = 3$. Constraint solves were performed every $0.2M$ in both cases. Although both cases performed much better than the unconstrained analogue plotted in Figure 6.4, there is clearly a destabilizing effect when solving the constraints at points immediately next to the excision region.
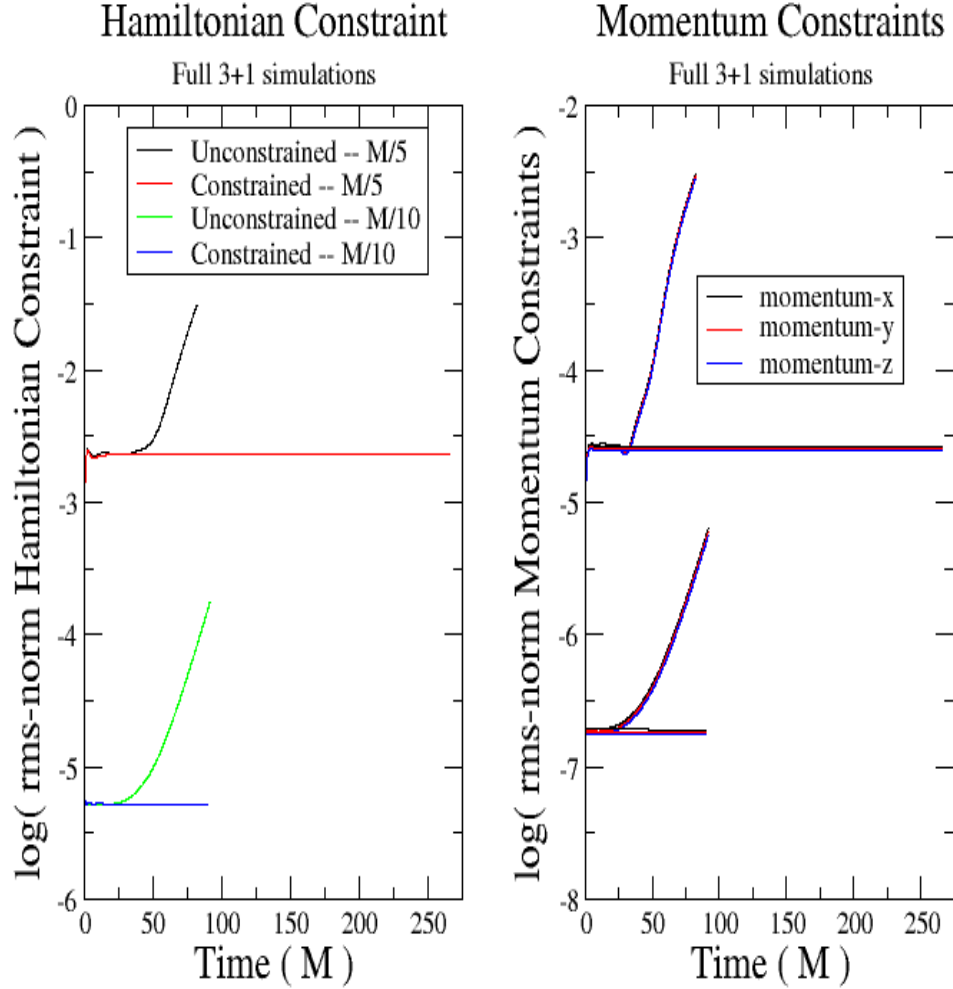
Figure 6.7: The log of the rms-norm for the Hamiltonian and momentum constraints in nonrotating Kerr-Schild hole simulations comparing constrained evolutions with unconstrained evolutions at two different resolutions. The domain in each simulation was $[-3M \ldots 3M]$ in each of the x,y,z directions. The constraints were solved every $0.1M$ in the constrained evolution cases, and the lapse was analytic for both constrained and unconstrained cases. For the constrained evolution cases, the constraints were solved across the entire domain except for points inside $r = 2M$. The singularity was excised at $r = 0.75M$ for all cases.

constrained evolution in such a way as to violate the governing evolution equations. An independent residual evaluation is the only way to verify that this is not the case.

Independent residual evaluations were performed on the simulations presented in Figure 6.7 in order to verify that the constrained evolutions did indeed solve the Einstein equations, Eq. (2.6). The independent residual evaluator uses the 3-metric, g_{ij}, and gauge output from a 3-D simulation to independently calculate time and spatial derivatives using finite difference stencils that are different from those in the evolution code. The residual evaluator then calculates the ten components of the Einstein tensor using the independently calculated derivatives and the supplied metric and gauge. The Hamiltonian and momentum constraints, $G_{0\lambda}$, are already plotted in Figure 6.7. The spatial components of the Einstein tensor, G_{ij}, are plotted in Figure 6.8. The convergent behavior of the Einstein tensor components confirms that the constrained evolution simulations were solving the Einstein equations.

Constrained evolution continues to substantially extend the lifetime of a Kerr-Schild black hole simulation when the domain is made slightly larger from $[-3M \ldots 3M]$ to $[-5M \ldots 5M]$. In Figure 6.9, the rms-norm of the Hamiltonian and momentum constraints are plotted for simulations comparing constrained versus unconstrained evolutions of a nonrotating Kerr-Schild black hole at two resolutions.

Simulations using an analytic lapse with domain sizes of $[-10M \ldots 10M]$ perform much worse with constrained evolution than their smaller domain counterparts presented in Figures 6.7 and 6.9. Figure 6.10 compares a constrained and unconstrained evolution of a single Kerr-Schild black hole with domain size of $[-10M \ldots 10M]$ using the analytic lapse. While the constrained case has a longer lifetime than the unconstrained case, problems arise in the constrained example
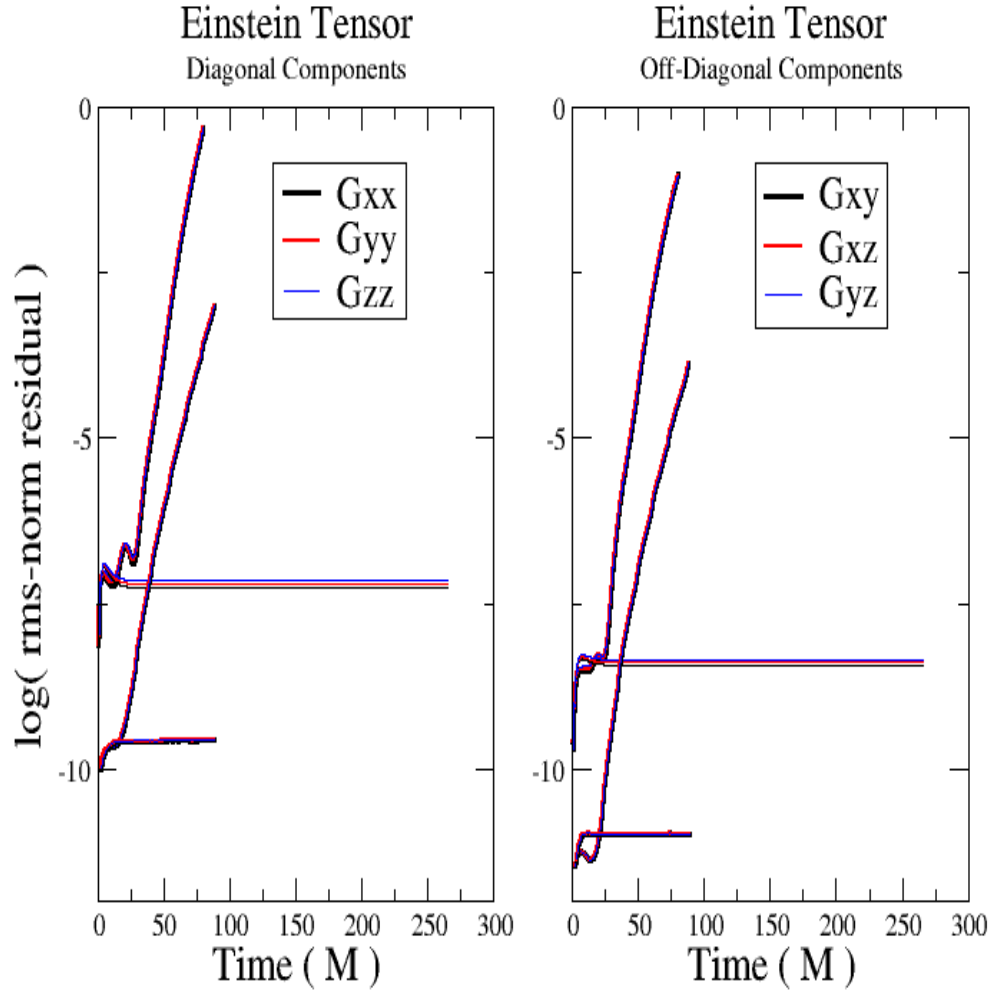
Figure 6.8: The log of the rms-norm for the spatial Einstein tensor components, G_{ij}. These were calculated via an independent residual evaluator to confirm that the constrained evolutions did solve the Einstein equations rather than simply controlling the constraint growth in a way inconsistent with the governing evolution equations. The residuals correspond to the unconstrained and constrained evolutions presented in Figure 6.7. The Einstein tensor components in the constrained evolutions are the convergent straight lines, while the components for the unconstrained evolutions are those that diverge quickly.

Figure 6.9: The rms-norm for the Hamiltonian and momentum constraints in simulations evolving a nonrotating Kerr-Schild black hole comparing constrained with unconstrained evolutions. The singularity was excised at a radius of $0.85M$ and the lapse was analytic in both cases. The constrained evolution cases solved the constraints every $0.1M$ everywhere on the domain except those points where $r < 1.65M$. The spatial domain of the simulations was $[-5M \ldots 5M]$ using a resolution of either $M/5$ or $M/7.5$.

near the excision region where no solving occurs. In this region, fields determined by free evolution serve as the boundary value for the trial fields in the elliptic solve. The constraint solver can do little to control constraint violating modes next to the excision region. These same modes are almost certainly present in the small domain examples of constrained evolution, but the small spatial domain likely prevents such modes from growing.

Two approaches have been explored to correct this problem: first, replacing the analytic lapse with a densitized lapse; second, addressing the problems immediately next to the excision region caused by the jagged shape of the mask.

The theoretical benefits of a densitized lapse have already been discussed in sections 2.3 and 4.8. Experimental results in 3-D unconstrained evolutions using standard ADM show no benefit from using a densitized lapse. This can be readily seen in simulations already presented in Figures 5.5 and 5.8. However, such unconstrained evolutions using standard ADM are already very unstable and may not constitute an adequate test of using a densitized lapse.

Figure 6.11 compares the Hamiltonian constraint for constrained and unconstrained evolutions using a densitized lapse. When comparing these results with the analytic lapse case, seen in Figure 6.10, no significant change in simulation lifetime is noted, even though the case using a densitized lapse appears to have fewer large oscillations in the Hamiltonian constraint. Both simulations experience a surge in the Hamiltonian constraint, beginning around time $70M$; these are due to oscillations in the dynamical variables in the region immediately next to the mask, where no solving occurs. 2-D slices at selected times of the error in g_{xx} taken from the constrained evolution using a densitized lapse with resolution $M/7.5$ can be viewed in Figures 6.12, 6.13, and 6.14.

Examining 2-D slices of errors in the dynamical variables for any evolution reveals distinct error patterns related to the discretized spherical shape of the mask.

The jagged shape of the mask likely contributes to the instability of a simulation, regardless if constrained or unconstrained. Causality problems can arise from finite differencing around the mask if care is not taken to ensure the excision region is small enough.

Making the excision region smaller is expensive computationally because higher resolution is required when evolving closer to the singularity. It also complicates efforts to correctly excise the singularity for boosted black holes in binary black hole spacetimes due to the small size of the excision region. To examine the effect of a smaller excision region, constrained and unconstrained evolutions were performed at three resolutions using an excision radius of $0.5M$. The constraint violations for these simulations are shown in Figures 6.15 and 6.16. While resolution $M/5$ was clearly not sufficient to evolve a nonrotating Kerr-Schild black hole with such a small excision radius, resolution $M/7.5$ was sufficient and lasted $100M$ longer than the exact same case using an excision radius of $0.75M$, seen in Figure 6.11. However, just as in the larger excision radius case, a surge in the constraints appears around $70M$. Independent residual evaluations showing the spatial Einstein tensor components reveal this same surge, only more pronounced. The independent residual evaluations for the constrained cases with resolution $M/7.5$ and $M/10$ are plotted in Figures 6.17 and 6.18. Notice particularly that the diagonal components lose convergence (the $M/7.5$ and $M/10$ residuals cross) around $t = 120M$. 2-D slices along $z = 0$ at selected times of the Einstein tensor component G_{xx} are shown in Figures 6.19, 6.20, 6.21, 6.22, 6.23. The loss of convergence after $t = 120M$ in the Einstein tensor suggests that, while the constraint solver is keeping the constraints from growing, the system is no longer solving the Einstein equations. This continues to be the challenge for large domain constrained evolution tests.

A way to solve problems associated with the jagged shape of the excision region is to make the excision region truly spherical by overlapping spherical and

Cartesian computational grids. This approach, motivated by the successful scalar field evolutions performed with this approach by G. Calabrese and D. Neilsen [63], has been implemented by the author for evolving the full Einstein vacuum equations and will be discussing in chapter 8. Further discussion of the causality problems due to the discretized shape of the excision region is found in section 8.1.

Solving the constraints in a constrained evolution over the entire computational domain, including those points immediately next to the excision region, results in unstable evolutions. Figure 6.24 shows a constrained evolution of a non-rotating Kerr-Schild hole in three spatial dimensions of size $[-10M \dots 10M]$ using a densitized lapse where the constraints were solved over the entire domain of the simulation. Consistent with the strategy of constrained evolution, the constraints were not solved to round-off precision every timestep. The solved fields immediately next to the excision region promoted an instability in the constrained evolution case. This result is not new; the same instability was found in the constrained evolution perfomed in 1-D/spherical symmetry presented in Figure 6.6. For further reference, Figure 6.25 compares two constrained evolution cases identical in every respect except for the domain over which the constraints are solved.

6.4 Constrained Evolution using GFR

Initial investigation into constrained evolution using GFR instead of ADM has shown encouraging results in spherical symmetry. Constrained evolution using ADM is currently superior to using GFR both with spherical symmetry and in full 3-D. However, as seen in section 6.3, corrections to ADM to improve hyperbolicity such as using a densitized lapse had a significant impact on the success of a constrained evolution. From this, it is not unreasonable to suspect that using a strongly hyperbolic formulation from the start will lead to successful constrained evolutions.

The method for constrained evolution of the GFR formulation consisted of
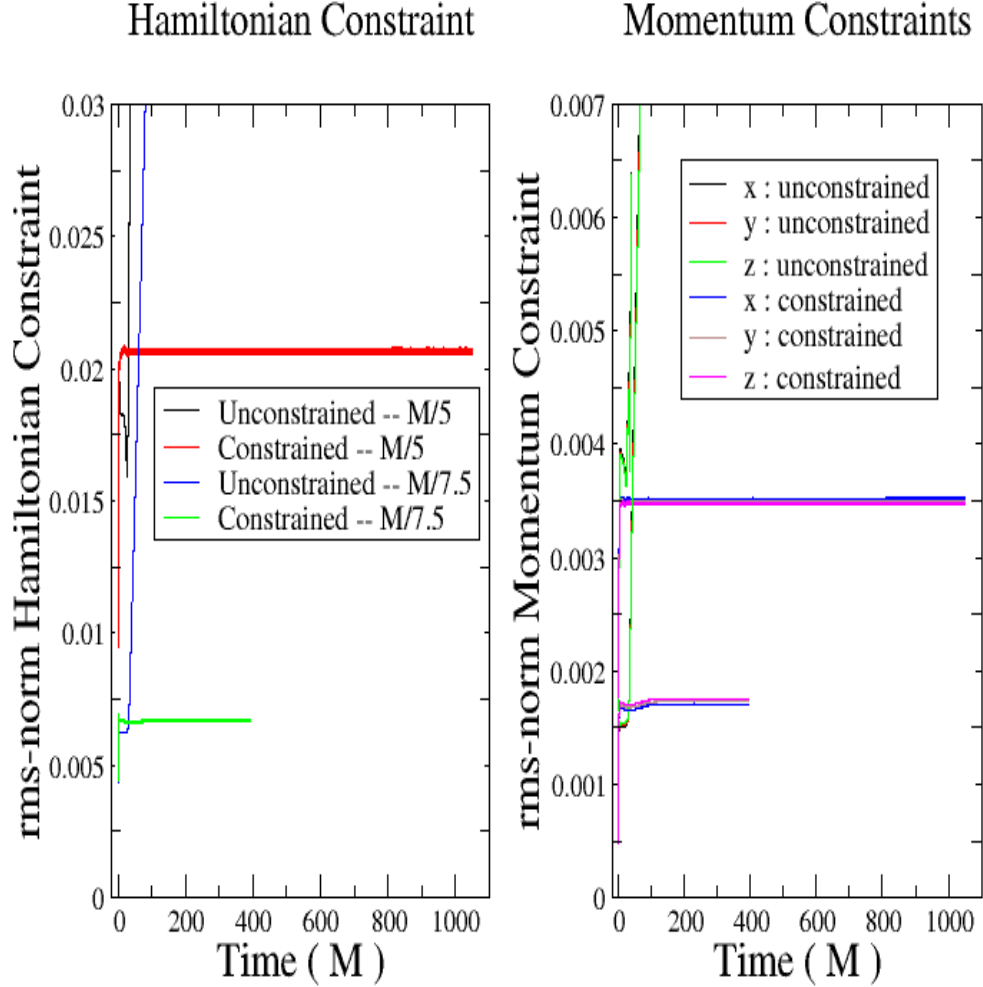
Figure 6.10: The rms-norm for the Hamiltonian constraint in simulations evolving a nonrotating Kerr-Schild black hole with a spatial domain of $[-10M \ldots 10M]$. The excision radius was $0.85M$ in both constrained and unconstrained cases. Both used the analytic lapse and had a resolution of $M/5$. The constraints were solved in the constrained evolution case every $0.1M$ everywhere on the domain except those points where $r < 1.65M$. There is a high-frequency oscillation in the rms-norm of the Hamiltonian constraint that appears around $t = 130$ in the constrained case, resulting in the thick troughs visible in the plot.
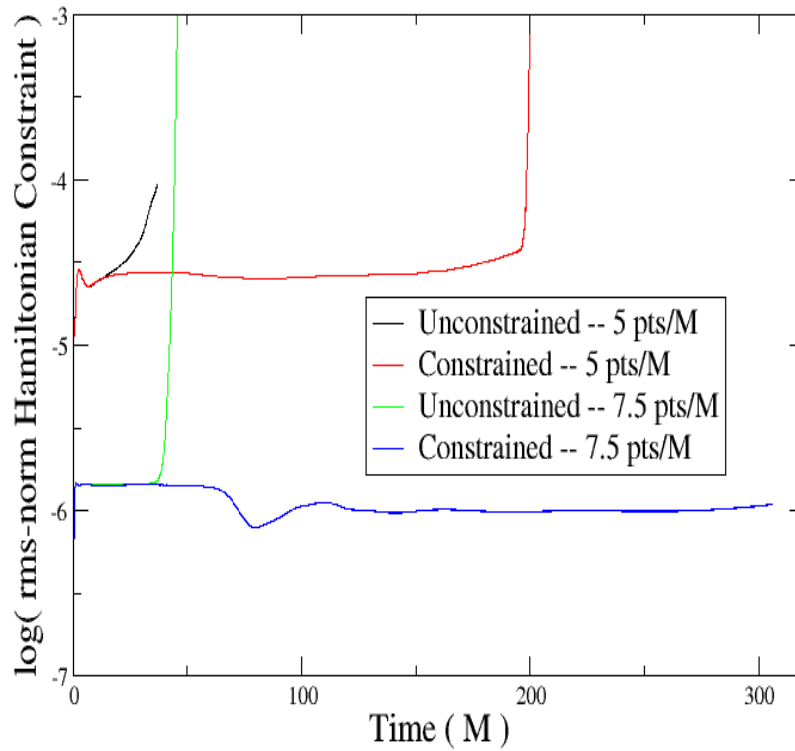
Figure 6.11: The log of the rms-norm for the Hamiltonian constraint in simulations evolving a nonrotating Kerr-Schild black hole with a spatial domain of $[-10M \ldots 10M]$ at two resolutions: $M/5$ and $M/7.5$. The excision radius was $0.75M$ in both constrained and unconstrained cases. All four simulations used a densitized lapse with $n = 3$. The constraints were solved in the constrained evolution cases every $0.05M$ everywhere on the domain except those points where $r < 2.0M$.
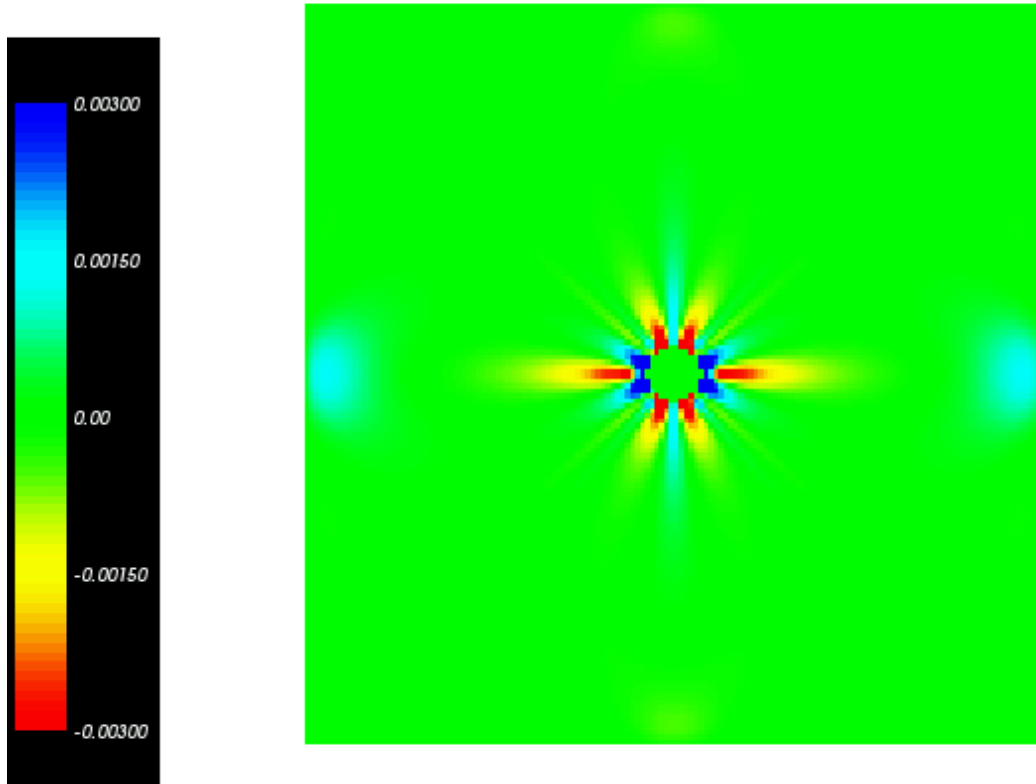
Figure 6.12: The $z = 0$ plane of the difference between the exact and numerical values of g_{xx} at time $80.0M$ for the $M/7.5$ constrained evolution shown in Figure 6.11. A large fluctuation in the Hamiltonian constraint occurs at $t = 80M$, due to variations in the fields next to the mask.
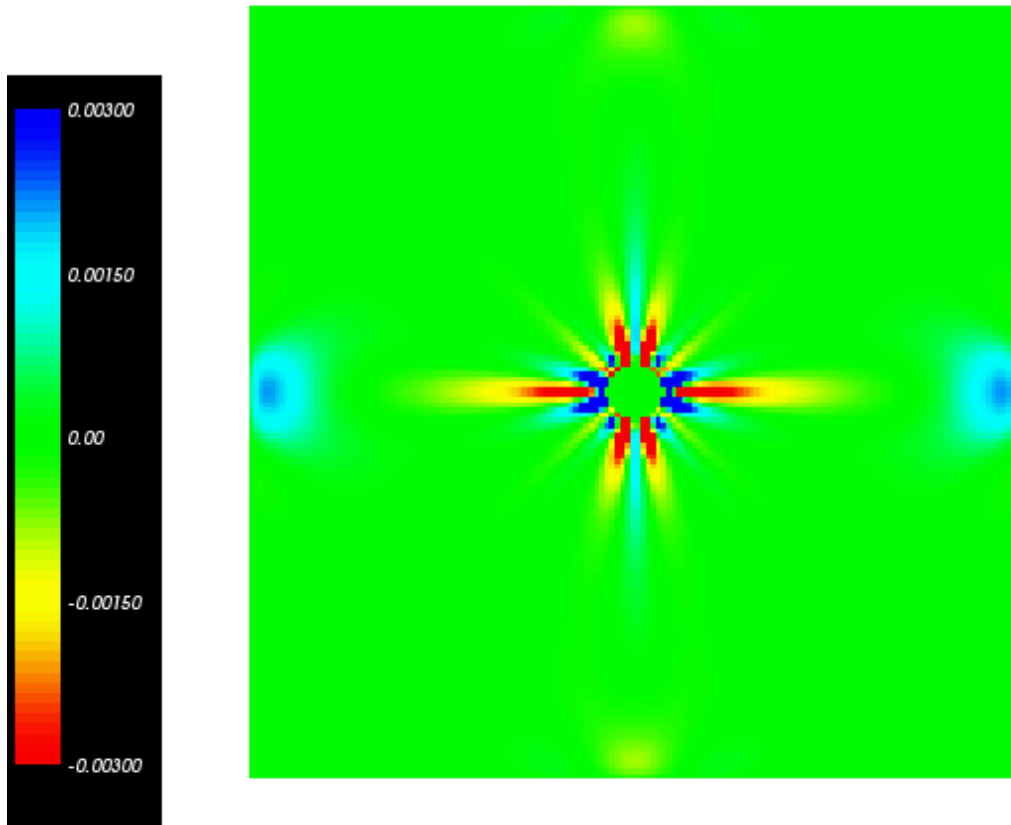
Figure 6.13: The $z = 0$ plane of the difference between the exact and numerical values of g_{xx} at time $120.0M$ for the $M/7.5$ constrained evolution shown in Figure 6.11. The fluctation in the Hamiltonian constraint stops at $t = 120M$.
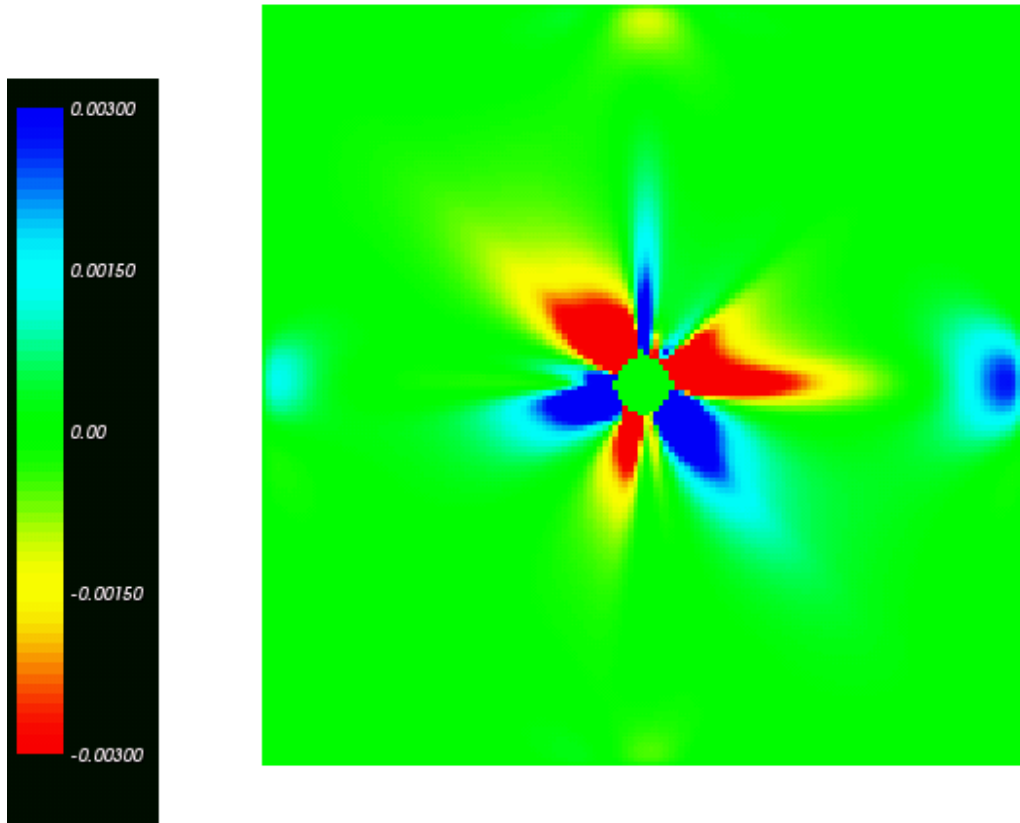
Figure 6.14: The $z = 0$ plane of the difference between the exact and numerical values of g_{xx} at time $300.0M$ for the $M/7.5$ constrained evolution shown in Figure 6.11. The simulation appears to be going unstable by this point.

Figure 6.15: The log of the rms-norm for the Hamiltonian constraint in simulations evolving a nonrotating Kerr-Schild black hole with a spatial domain of $[-10M \ldots 10M]$ at three resolutions: $M/5$, $M/7.5$, and $M/10$. The momentum constraint violations can be found in Figure 6.16. The excision radius was $0.5M$ in all constrained and unconstrained cases. All simulations used a densitized lapse with $n = 3$. The constraints were solved in the constrained evolution cases every $0.05M$ everywhere on the domain except those points where $r < 2.0M$. The simulations presented here with resolution $M/5$ and $M/7.5$ are the same as those presented in Figure 6.11 except these were performed with a smaller excision region. Independent residual evaluations for the constrained cases with resolution $M/7.5$ and $M/10$ are found in Figures 6.17 and 6.18.

91
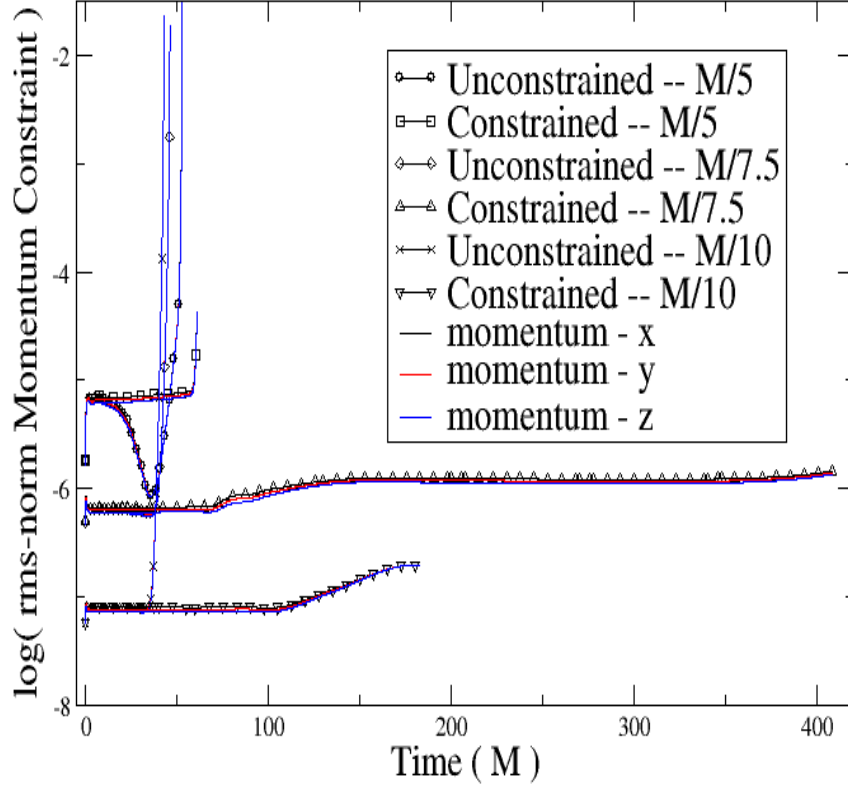
Figure 6.16: The log of the rms-norm for the momentum constraints in simulations evolving a nonrotating Kerr-Schild black hole with a spatial domain of $[-10M \ldots 10M]$ at three resolutions: $M/5$, $M/7.5$, and $M/10$. The Hamiltonian constraint violation can be found in Figure 6.15. The excision radius was $0.5M$ in all constrained and unconstrained cases. All simulations used a densitized lapse with $n = 3$. The constraints were solved in the constrained evolution cases every $0.05M$ everywhere on the domain except those points where $r < 2.0M$. The simulations presented here with resolution $M/5$ and $M/7.5$ are the same as those presented in Figure 6.11 except these were performed with a smaller excision region. Independent residual evaluations for the constrained cases with resolution $M/7.5$ and $M/10$ are found in Figures 6.17 and 6.18. Notice that the solution appears to be losing convergence at $t \simeq 120M$. (The $M/10$ curves are no longer separated by a constant logarithm from the $M/7.5$ curve).
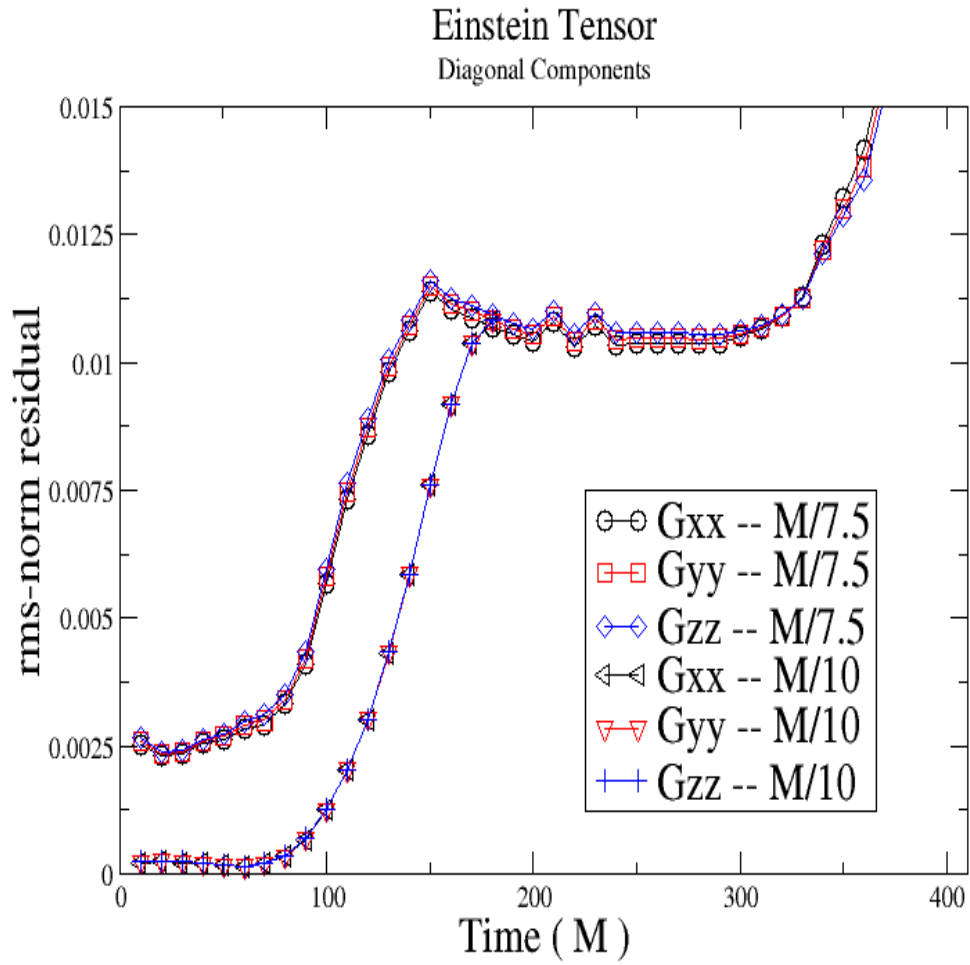
Figure 6.17: The rms-norm of the spatial diagonal components of the Einstein tensor for the $M/7.5$ and $M/10$ constrained simulations presented in Figures 6.15 and 6.16. The loss of convergence around $t = 120M$ is more evident in these residuals.
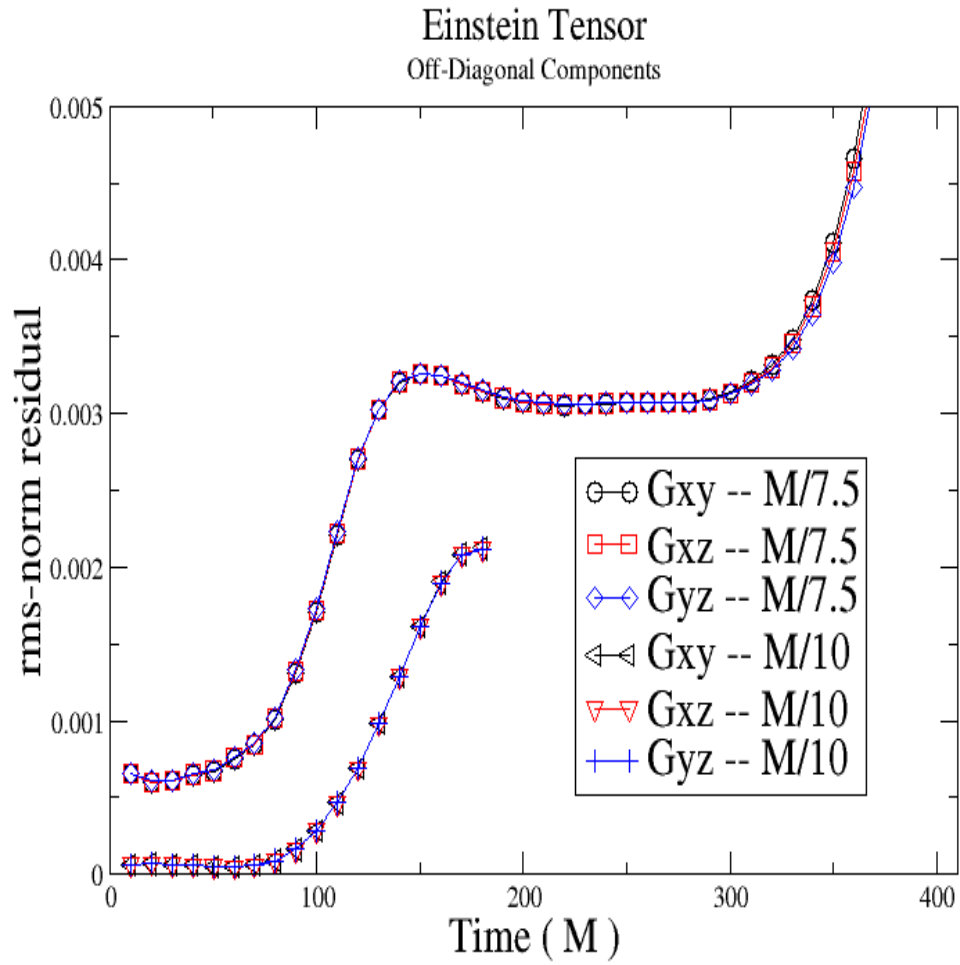
Figure 6.18: The rms-norm of the spatial off-diagonal components of the Einstein tensor for the $M/7.5$ and $M/10$ constrained simulations presented in Figures 6.15 and 6.16.
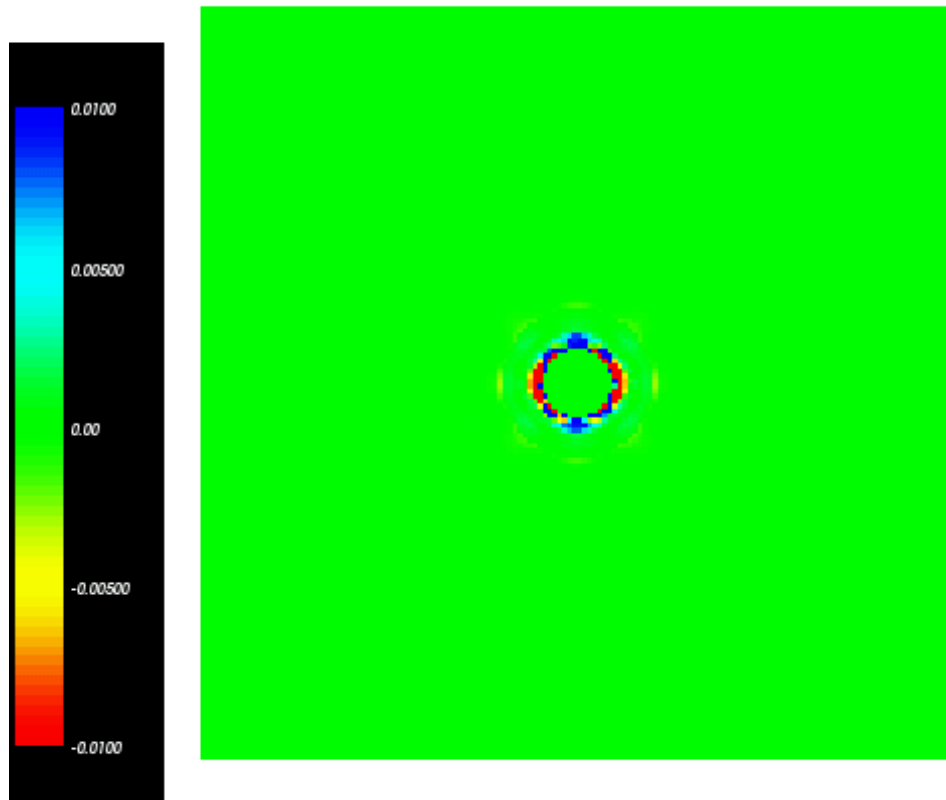
Figure 6.19: The $z = 0$ plane of the Einstein tensor component G_{xx} at time $10M$ for the $M/7.5$ constrained evolution presented in Figure 6.17.
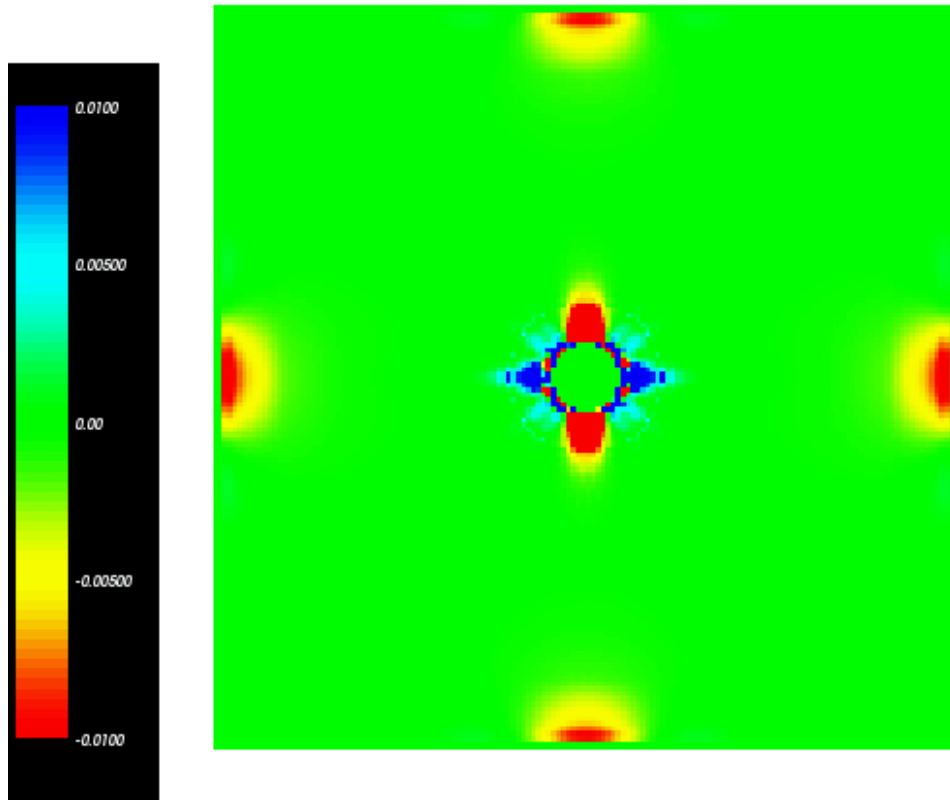
Figure 6.20: The $z = 0$ plane of the Einstein tensor component G_{xx} at time $100M$ for the $M/7.5$ constrained evolution presented in Figure 6.17.
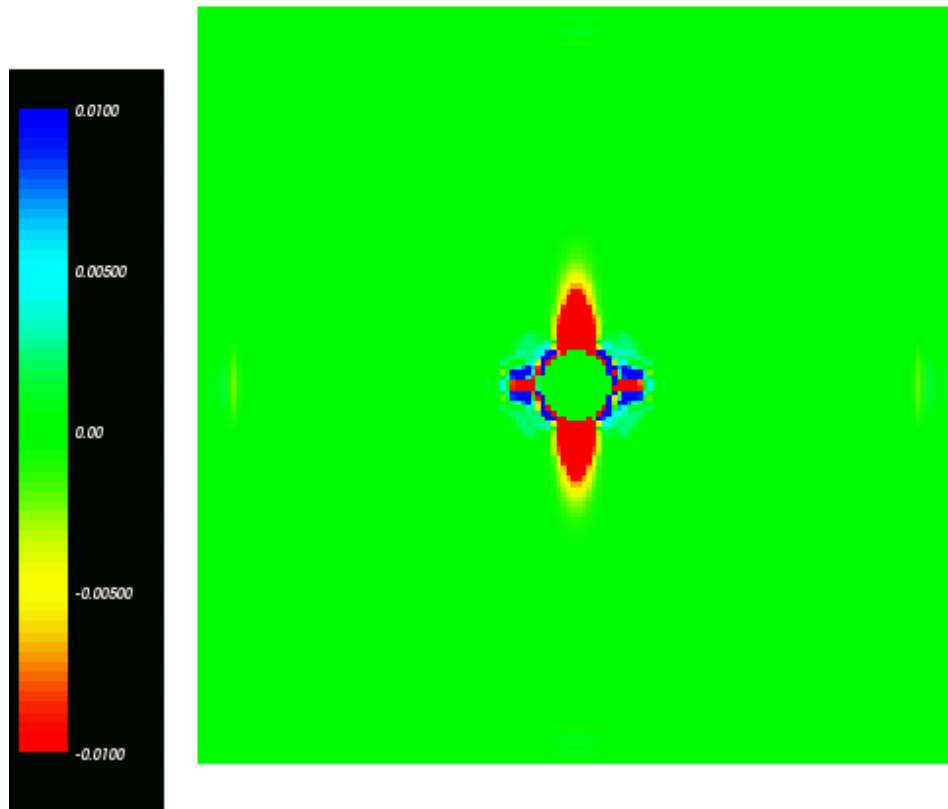
Figure 6.21: The $z = 0$ plane of the Einstein tensor component G_{xx} at time $200M$ for the $M/7.5$ constrained evolution presented in Figure 6.17.
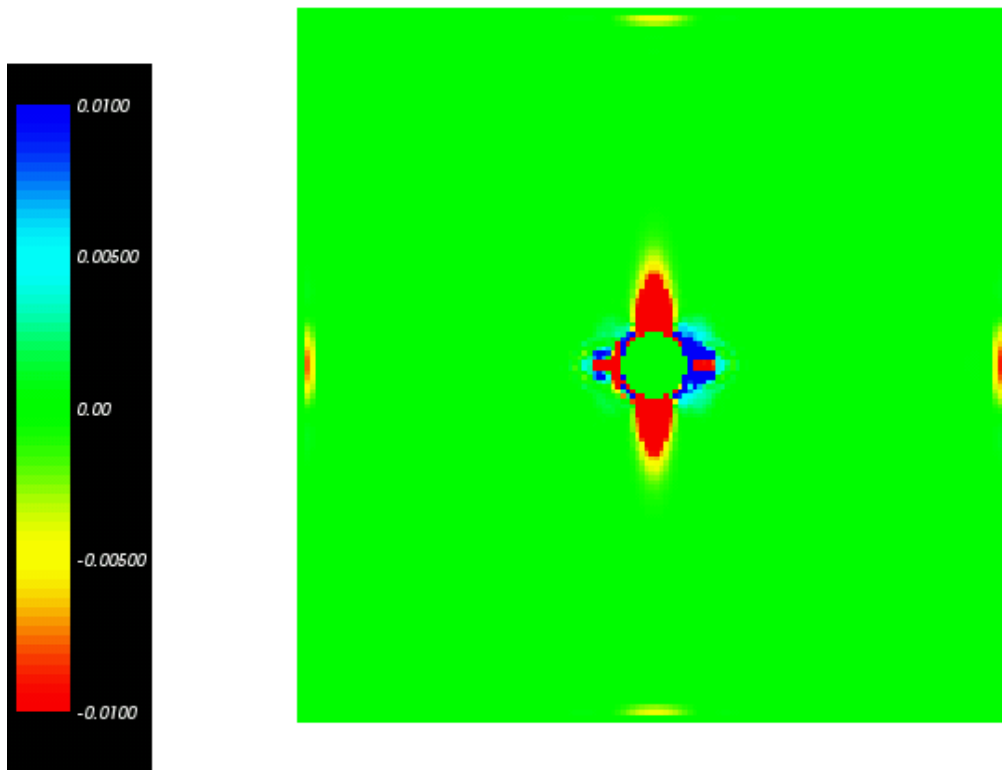
Figure 6.22: The $z = 0$ plane of the Einstein tensor component G_{xx} at time $300M$ for the $M/7.5$ constrained evolution presented in Figure 6.17.
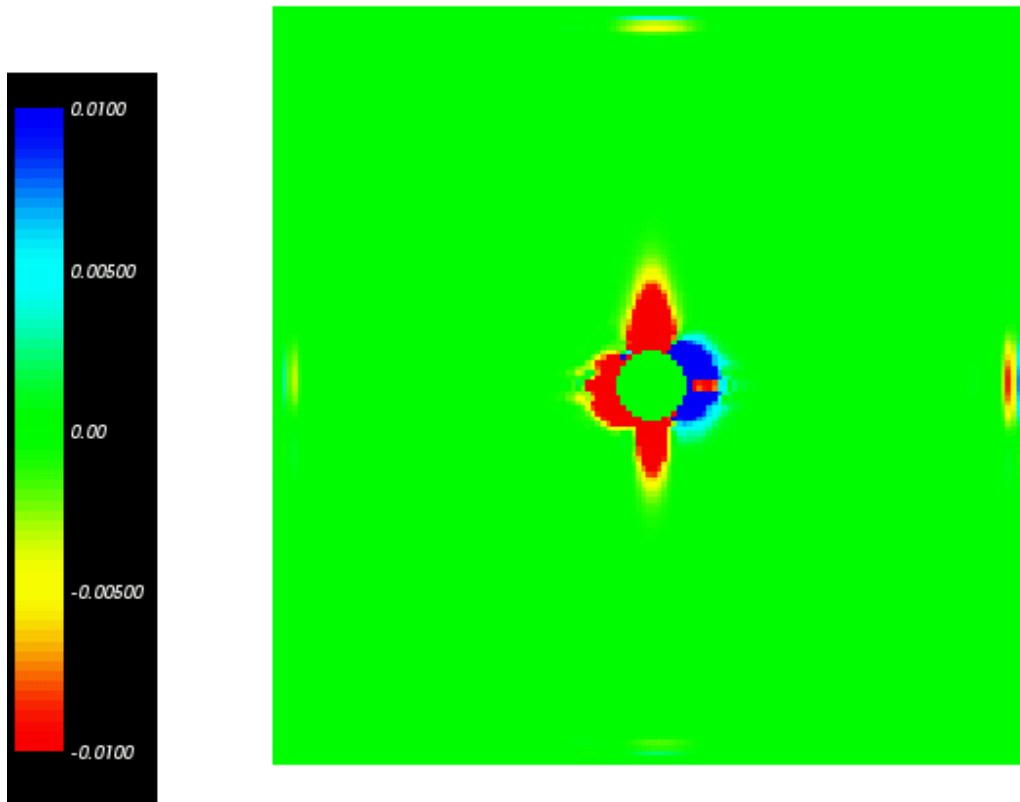
Figure 6.23: The $z = 0$ plane of the Einstein tensor component G_{xx} at time $400M$ for the $M/7.5$ constrained evolution presented in Figure 6.17.
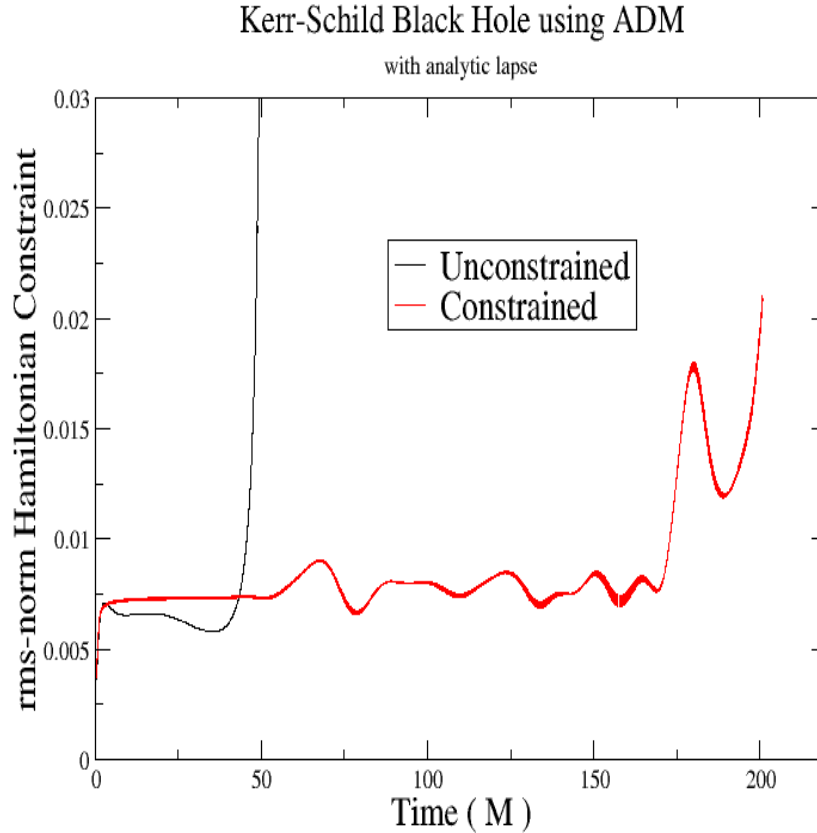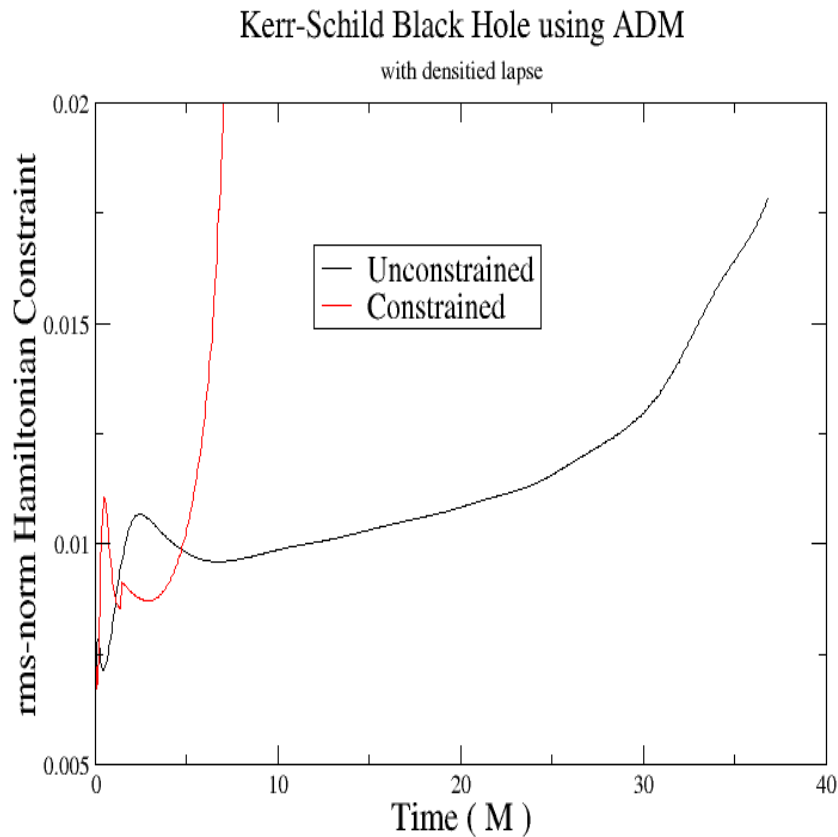
Figure 6.24: The rms-norm for the Hamiltonian constraint in simulations evolving a nonrotating Kerr-Schild black hole with a spatial domain of $[-10M \ldots 10M]$ at resolution of $M/5$. The excision radius was $0.75M$ in both constrained and unconstrained cases. Both simulations used a densitized lapse with $n = 3$. The constraints were solved in the constrained evolution case every $0.05M$ everywhere on the domain, even at points immediately next to the excision region. Unstable behavior in constrained evolution has been seen before in comparable spherically symmetric simulations where the constraints were solved at the points immediately next to the excision region. See Figure 6.6.

Kerr-Schild Black Hole using ADM

Constrained Evolution with densitized lapse
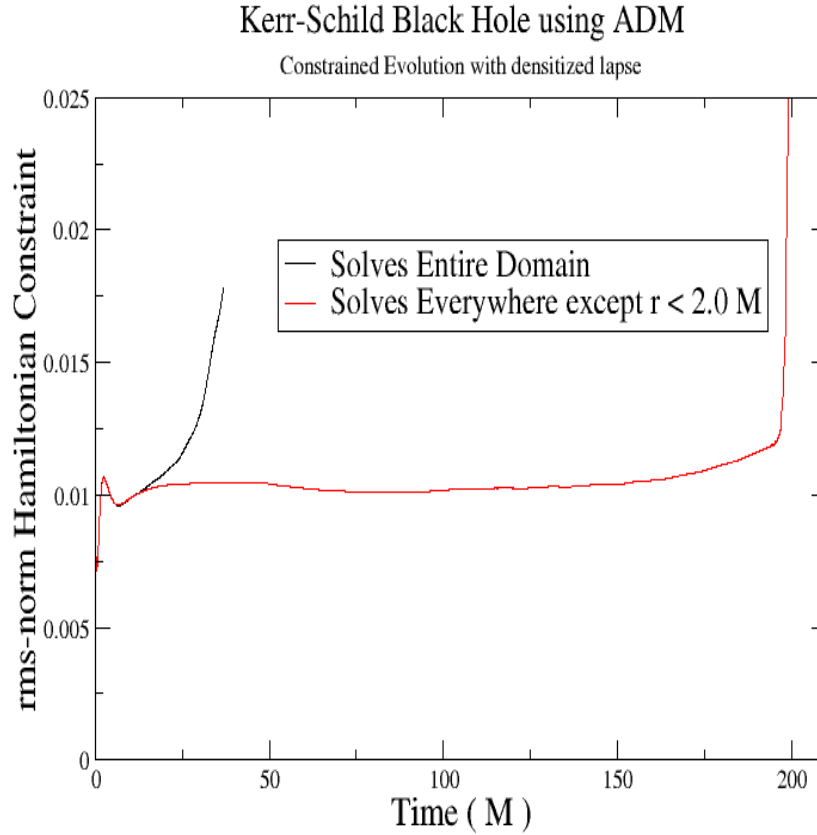
Figure 6.25: The rms-norm for the Hamiltonian constraint in two constrained evolution simulations evolving a nonrotating Kerr-Schild black hole with a spatial domain of $[-10M \ldots 10M]$ at resolution of $M/5$. The simulations are identical in all respects except for the domain over which the constraints were solved. The excision radius was $0.75M$ in both cases. Both simulations used a densitized lapse with $n = 3$ and the constraints were solved every $0.05M$. The constrained evolution case which solved the constraints over the entire domain blew up quickly. The constrained evolution case which solved the constraints only at those points where $r \geq 2.0M$ did much better. The short lived simulation here is the same as the constrained solution shown in Figure 6.24.

101

converting the GFR variables h^{ij} and P^{ij} to ADM variables. The constraints were subsequently solved using the conformal transverse-traceless method discussed in section 3.1. The updated fields g_{ij} and K_{ij} were then converted back to GFR variables h^{ij} and P^{ij} and the evolution would then proceed. Constrained evolution tests showed that enforcing the definition of $M^{ij}{}_k$,

$$M^{ij}{}_k \;=\; \frac{1}{2}\left(\partial_k h^{ij} - h^{ij}h_{mn}\partial_k h^{mn}\right),$$

resulted in wildly unstable simulations. Consequently, the $M^{ij}{}_k$ variables were not updated after a constraint solve in a constrained evolution. The $M^{ij}{}_k$ definition becomes an unenforced constraint with this approach, even as the Hamiltonian and momentum constraints are enforced.

Figure 6.26 compares constrained and unconstrained GFR evolutions of a nonrotating Kerr-Schild black hole with spherical symmetry. Throughout the constrained simulations, constraint violating modes appear but remain under control by the constraint solver. However, when similar simulations are performed in full 3-D, the case for constrained evolution is less convincing.

Figure 6.27 compares constrained and unconstrained evolutions of a nonrotating Kerr-Schild black hole in full 3-D. The parameters in the formulation were chosen so that the evolution equations alone are weakly hyperbolic. This can be compared with Figure 6.28, which compares constrained and unconstrained evolutions at different resolutions with the formulation parameters η, γ, and Θ chosen so that the evolution equations alone are strongly hyperbolic.

While the constrained evolution examples presented here do poorly when using GFR without any symmetries, most of the parameter space for GFR remains unexplored. Experience in using ADM suggests that improving the hyperbolicity of the evolution equations can positively impact a constrained evolution. Further study into constrained evolution using GFR or another strongly hyperbolic formulation is warranted.
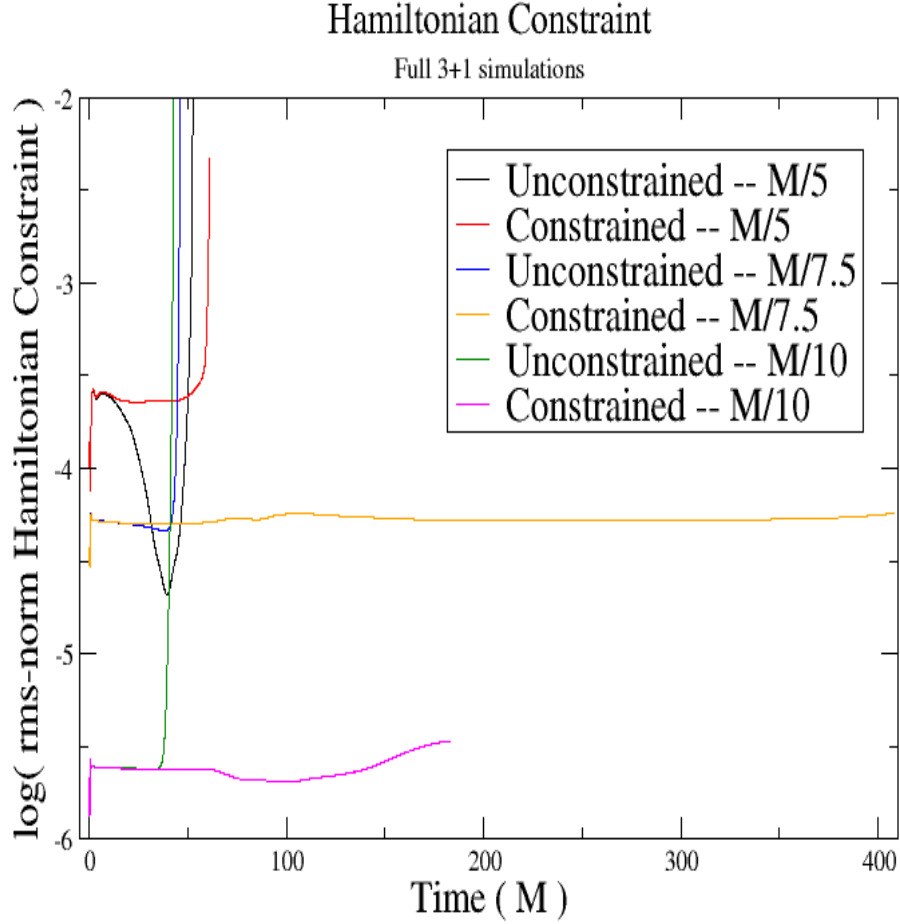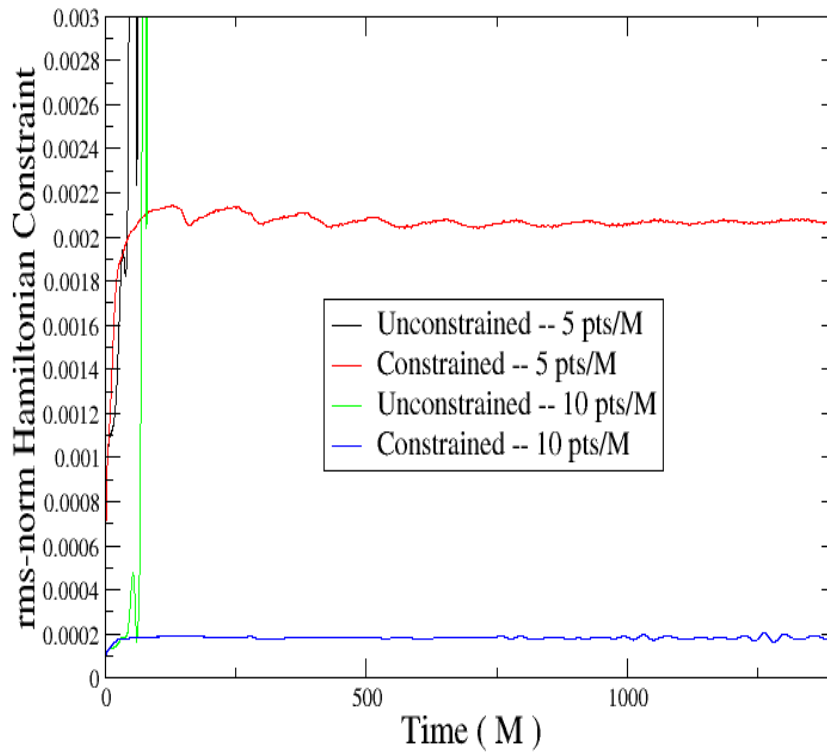
Figure 6.26: The rms-norm for the Hamiltonian constraint in simulations evolving a nonrotating Kerr-Schild black hole in spherical symmetry with a spatial domain of $[0.8M \ldots 250M]$ using the GFR formulation. The parameters were chosen so that the evolution system alone is at least strongly hyperbolic: $\eta = 0.85$, γ and Θ chosen according to Eq. (2.38). The constraints were solved in the constrained evolution case every $0.2M$ everywhere on the domain except those points where $r < 2.4M$.
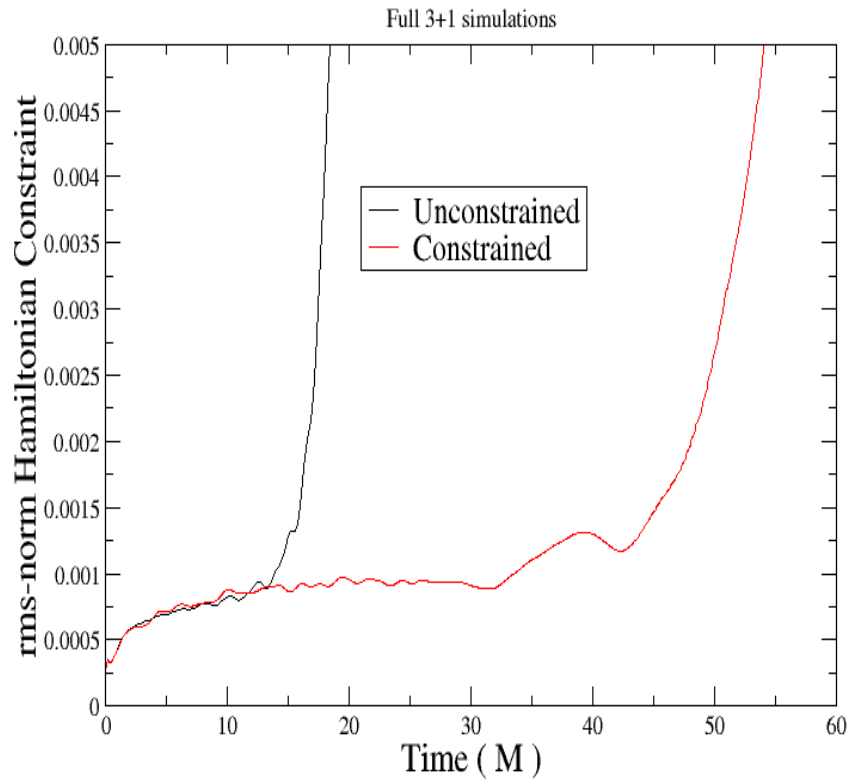
Figure 6.27: The rms-norm for the Hamiltonian constraint in simulations evolving a nonrotating Kerr-Schild black hole with a spatial domain of $[-10M \ldots 10M]$ at resolution of $M/5$ using the GFR formulation. The parameters were chosen so that the evolution system alone is weakly hyperbolic: $\eta = 0.5$, $\gamma = 0.8$, and $\Theta = 0.8$. The excision radius was $0.75M$ in both constrained and unconstrained cases. The constraints were solved in the constrained evolution case every $0.05M$ everywhere on the domain except those points where $r < 2.3M$.
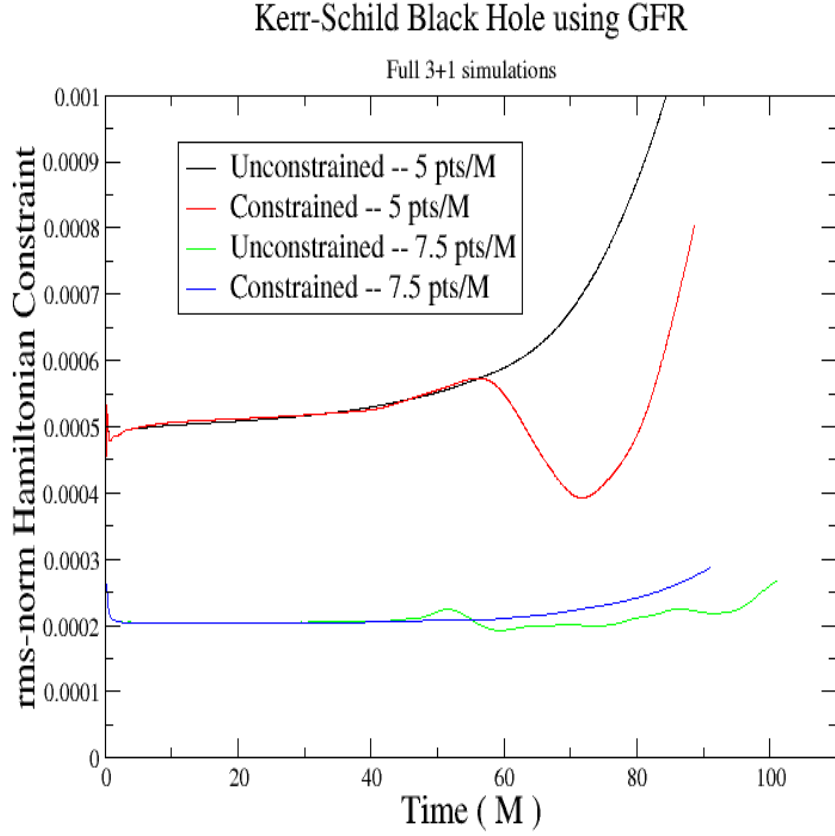
Figure 6.28: The rms-norm for the Hamiltonian constraint in simulations evolving a nonrotating Kerr-Schild black hole with a spatial domain of $[-10M \ldots 10M]$ at resolution of $M/5$ and $M/7.5$ using the GFR formulation. The parameters were chosen so that the evolution system alone is at least strongly hyperbolic: $\eta = 0.85$, γ and Θ chosen according to Eq. (2.38). The excision radius was $0.75M$ in all constrained and unconstrained cases. The constraints were solved in the constrained evolution case every $0.05M$. The constrained simulation with resolution $M/5$ solved the constraints everywhere on the domain except those points where $r < 3.0M$; the constrained simulation with resolution $M/7.5$ solved the constraints everywhere except where $r < 2.3$.

Chapter 7

Constrained Mesh Refined Black Hole Spacetimes

Large domain simulations, necessary to model gravitational radiation from binary black hole spacetimes, are computationally demanding both in terms of time and memory when performed with only one global resolution. Steep gradients occur in the dynamical variables near a black hole and high resolution is needed to adequately resolve this region. However, there is no need for high resolution far from a hole where the gradients are close to zero. This fact has motivated many attempts at using mesh refinement in evolving black hole spacetimes. Often errors grow at the coarse-fine mesh interfaces in these simulations, resulting in unstable evolutions. This chapter examines the influence of constraint solving on mesh refined systems. Evidence is given that constrained evolution can improve a mesh refined simulation which would otherwise be extremely short-lived due to poor treatment at the coarse-fine interface.

7.1 Brief History

Many successful efforts have been conducted to model black hole spacetimes with mesh refinement. These are based on the principles published by Berger and Oliger in 1984 [64] and generally employ interpolation from the coarse grid to a finer nested grid for the finer grid boundaries. Restriction operations provide fine grid data to the coarse grid where there is an overlap. Mesh refinement was first applied to a Schwarzschild black hole in 1996 by B. Brügmann [65]. In 2003, B. Brügmann et al. reported evolving an orbiting binary black hole system using fixed mesh refinement and the BSSN formulation [66]. Using the CACTUS toolkit [67], E. Schnetter, S. Hawley, and I. Hawke published in 2004 fixed mesh refinement results for a Schwarzschild black hole using the BSSN formulation that were comparable to unigrid results in terms of accuracy, stability, and convergence [68]. These simulations evolved the system in octant symmetry using standard excision. Also in 2004, B. Imbiriba et al. published fixed mesh refinement results for a Schwarzschild black hole using the BSSN formulation and the puncture method to treat the singularity [69]. Using the PARAMESH toolkit [70], they present an algorithm for handling the coarse-fine interfaces to improve stability in a mesh refined simulation.

In all these examples critical interpolation conditions had to be developed to handle the restriction and refinement operations. The interpolation conditions at the coarse-fine interfaces can be crucial to a successful mesh refined simulation as was explored by D. Choi and collaborators [71]. Further, these interpolation conditions are particular to the integration method. All the above examples used either a leapfrog-like method or iterative Crank-Nicholson for the evolution scheme, were unconstrained, and used only second-order spatial difference operators. The remainder of this chapter will investigate mesh refinement using Adams-Moulton as the evolution scheme in both unconstrained and constrained evolutions with fourth-order spatial difference operators. Only very simple interpolation conditions will be

used.

7.2   Examples

Two examples of mesh refined evolutions are presented in this section: the first unconstrained and the second constrained. The refinement and restriction operations proceed as outlined in section 4.4. The simulation *methods* are identical to one another: fourth order Lagrangian interpolation is used for the refinement interpolation and cubic spline interpolation is used in the restriction operation. The simulations are cell centered with a single refined region consisting of a cube extending in each spatial direction from $[-5M \ldots 5M]$ nested on a coarse global grid of $[-10M \ldots 10M]$. Figures 7.1 and 7.2 show the mesh structure. The Hamiltonian and momentum constraints in the constrained and unconstrained evolutions are shown in Figure 7.3. The stability of these runs can be compared to the analogous unigrid case already presented in Figure 5.9.

Neither the constrained nor the unconstrained simulation duplicates the stability seen in the unigrid case. This may be due to the simplicity of the interpolation schemes for refinement and restriction, presented in section 4.4. Fourth order finite differencing requires two or more interpolated boundary points, which can be a source of noise if using Lagrangian interpolation. Another explanation may be that the refinement volume was too small and the global grid resolution too coarse to adequately evolve the hole. However, in spite of an apparently poor interpolation strategy and perhaps inadequate coarse grid resolution, the constrained case prevented error from growing at the coarse-fine interface. Those interpolation conditions that are so critical for stability in solving hyperbolic equations with mesh refinement are not nearly so exacting in solving elliptic equations with mesh refinement. The constraint solver can then considerably enhance a mesh refined evolution in spite of poor interpolation conditions. Figures 7.4, 7.5, and 7.6 show 2-D slices of

the error in g_{xx} at different times in the unconstrained evolution. For comparison, Figures 7.7, 7.8, and 7.9 show 2-D slices of the error in g_{xx} at different times in the constrained evolution.

7.3 Performance Notes

Considerable performance benefits continue to encourage investigation into mesh refinement. The speedup for the constrained evolution mesh refined case in section 7.2 is shown in Figure 7.10. Figure 7.11 shows the memory requirements for simulations evolving domains of $[-20M \ldots 20M]$ on different numbers of processors, comparing the mesh refined case with the unigrid case.
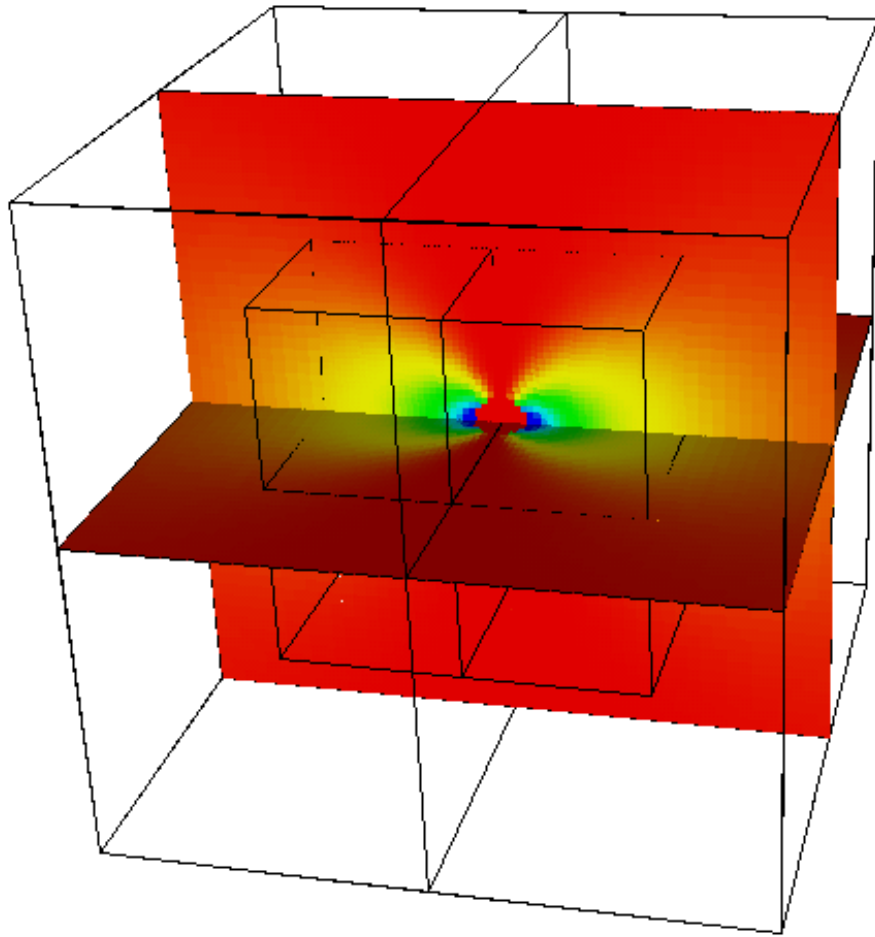
Figure 7.1: Bounding boxes for the grid used in the examples of section 7.2. The interior bounding boxes indicate where mesh refinement begins. The metric component g_{xx} is also shown for reference. A slice along the $z = 0$ plane from this grid is shown in Figure 7.2.
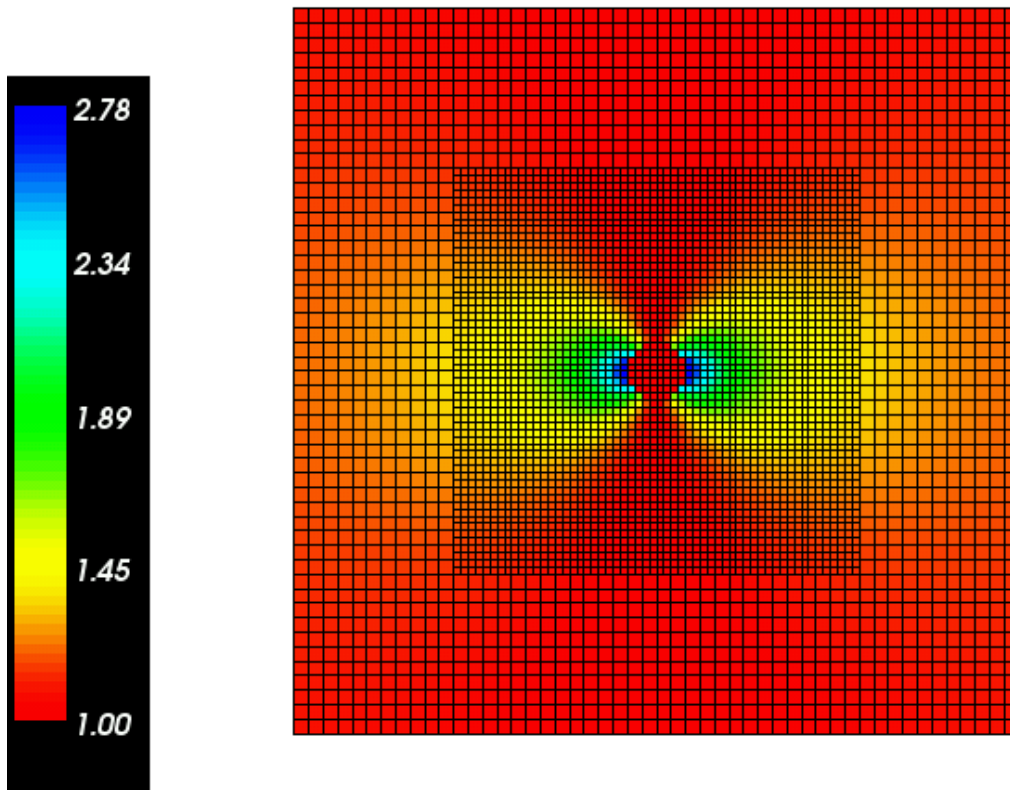
Figure 7.2: The $z = 0$ plane from the center of the 3-D mesh for the two examples presented in section 7.2. The metric component g_{xx} is also shown for reference.
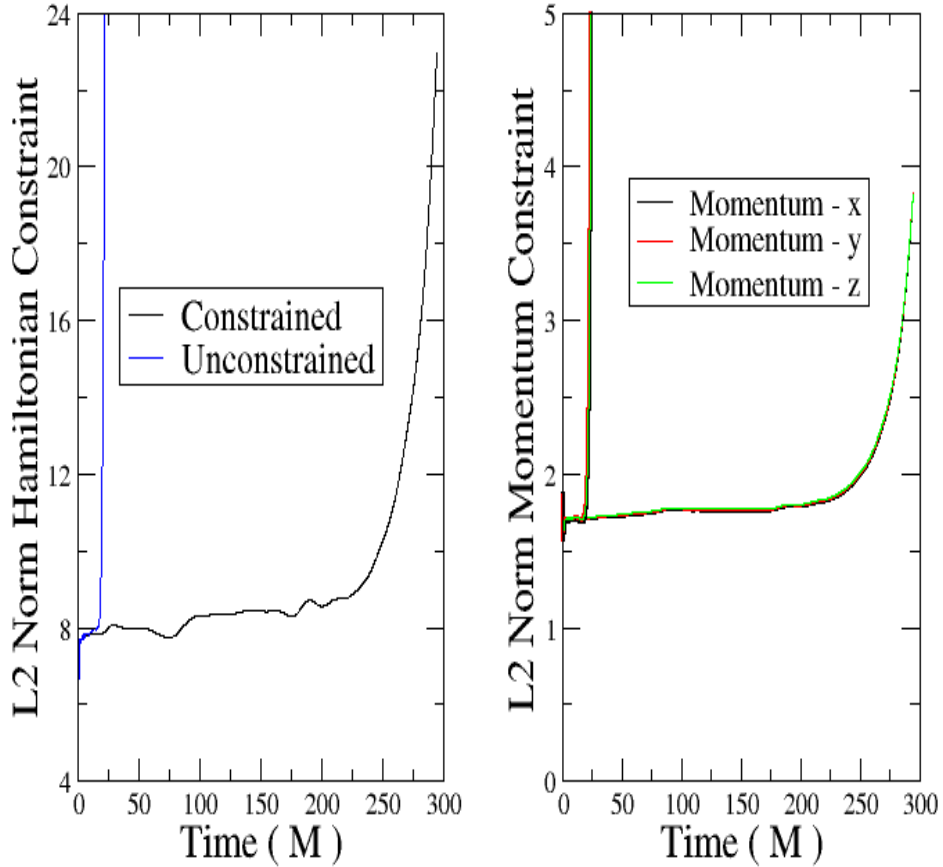
Figure 7.3: The l_2-norm of the Hamiltonian and momentum constraints for constrained and unconstrained mesh refined simulations. A single nonrotating Kerr-Schild black hole using ADM is evolved in these case. One level of refinement was employed in each simulation. The resolution for the coarse global grid was $M/2.5$ and for the fine $M/5$. The coarse global grid extended over a domain of $[-10M \ldots 10M]$. The fine grid extended over a domain of $[-5M \ldots 5M]$. The excision radius was at $r = 0.85$. The analytic lapse was used in both cases, as was the constraint subtraction specified in Eq. (5.1). For the constrained case, the solver only solved those points where $r > 4M$ every $0.1M$. The unigrid analogue of these runs is seen in Figure 5.9, where substantially longer run times are achieved.
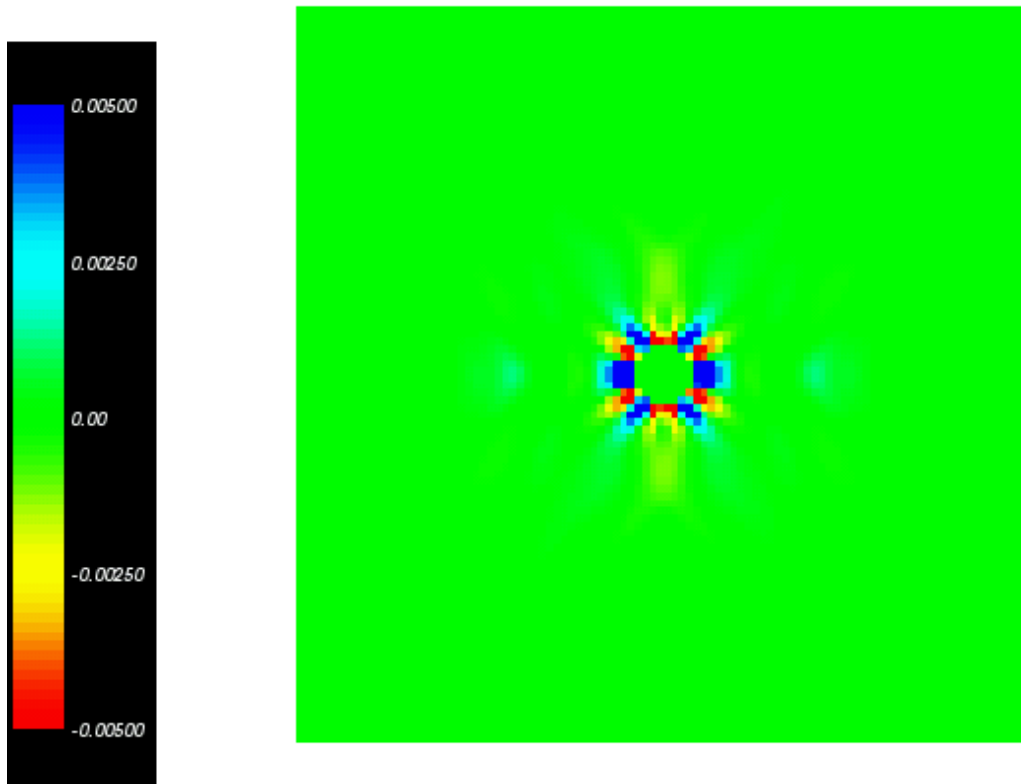
Figure 7.4: The $z = 0$ plane showing the error in g_{xx} at time $10M$ for the unconstrained simulation in Figure 7.3. Small but noticeable errors are already appearing at the coarse-fine interface.
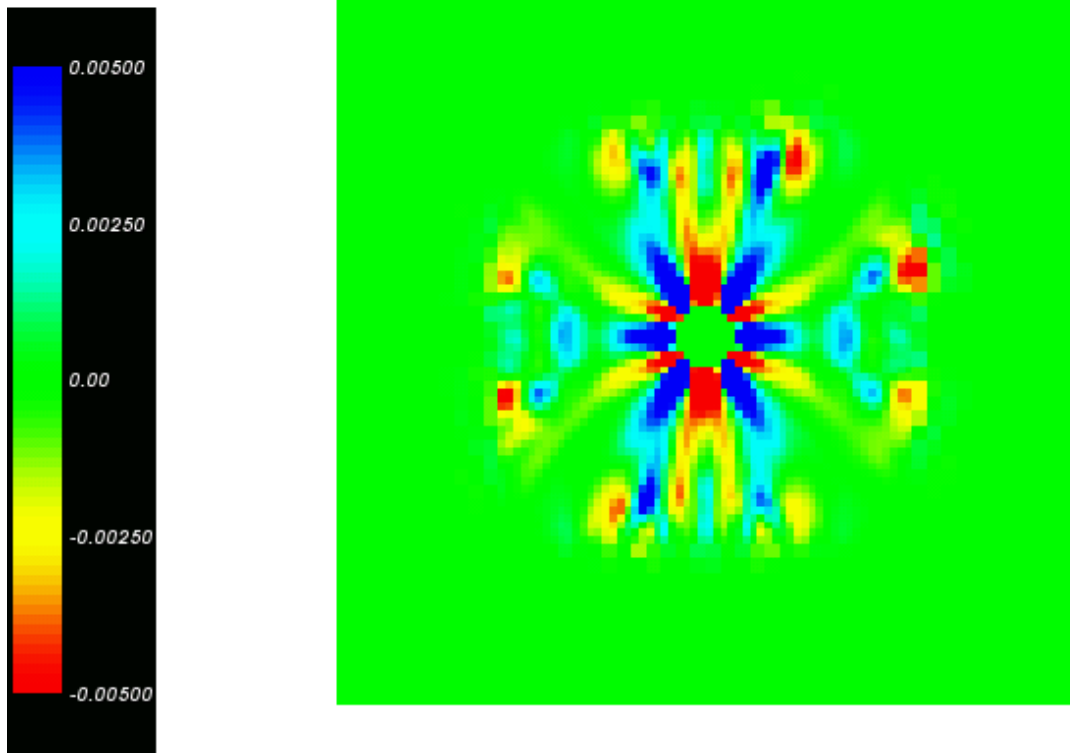
Figure 7.5: The $z = 0$ plane showing the error in g_{xx} at time $20M$ for the unconstrained simulation in Figure 7.3. The errors at the coarse-fine interface are very significant at this point.
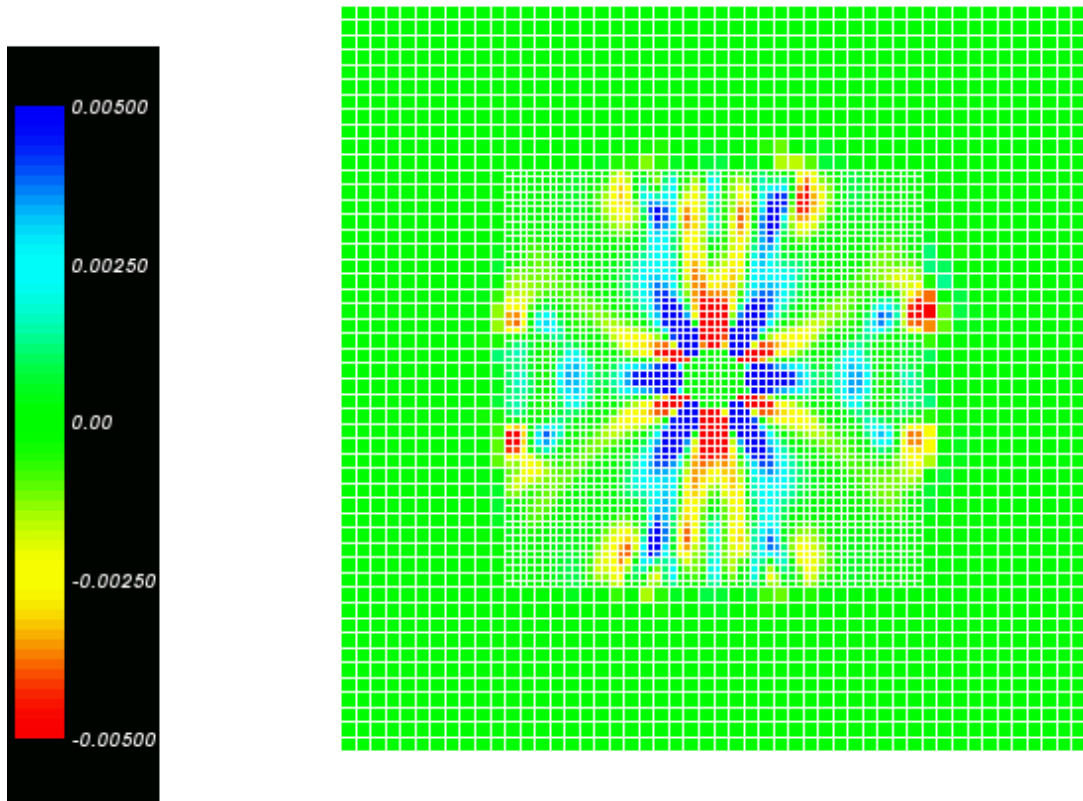
Figure 7.6: The $z = 0$ plane showing the error in g_{xx} at time $20M$ for the unconstrained simulation in Figure 7.3. This plot is the same as Figure 7.5 except the grid is included for reference.
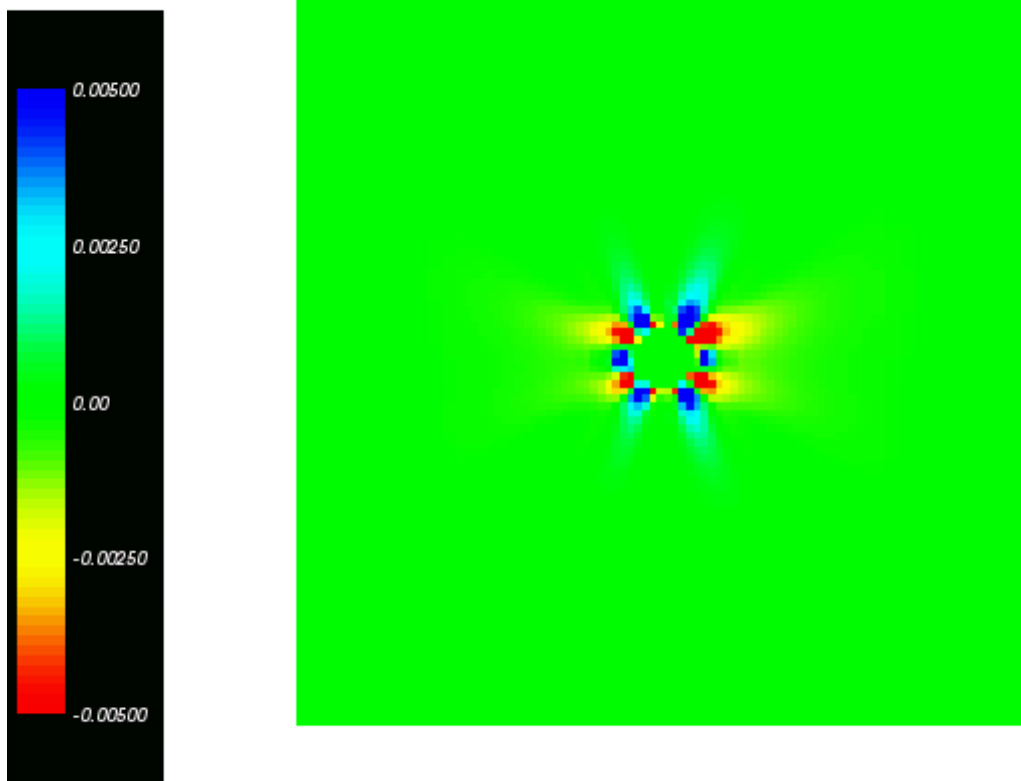
Figure 7.7: The $z = 0$ plane showing the error in g_{xx} at time $50M$ for the constrained simulation in Figure 7.3.
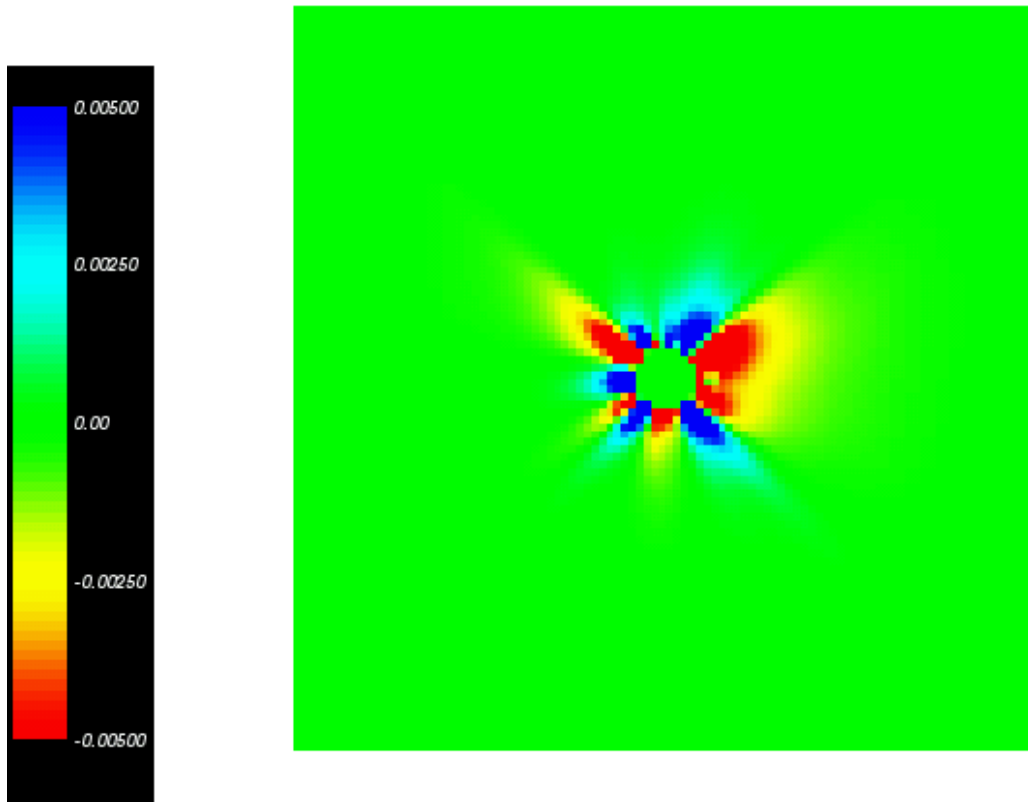
Figure 7.8: The $z = 0$ plane showing the error in g_{xx} at time $150M$ for the constrained simulation in Figure 7.3.
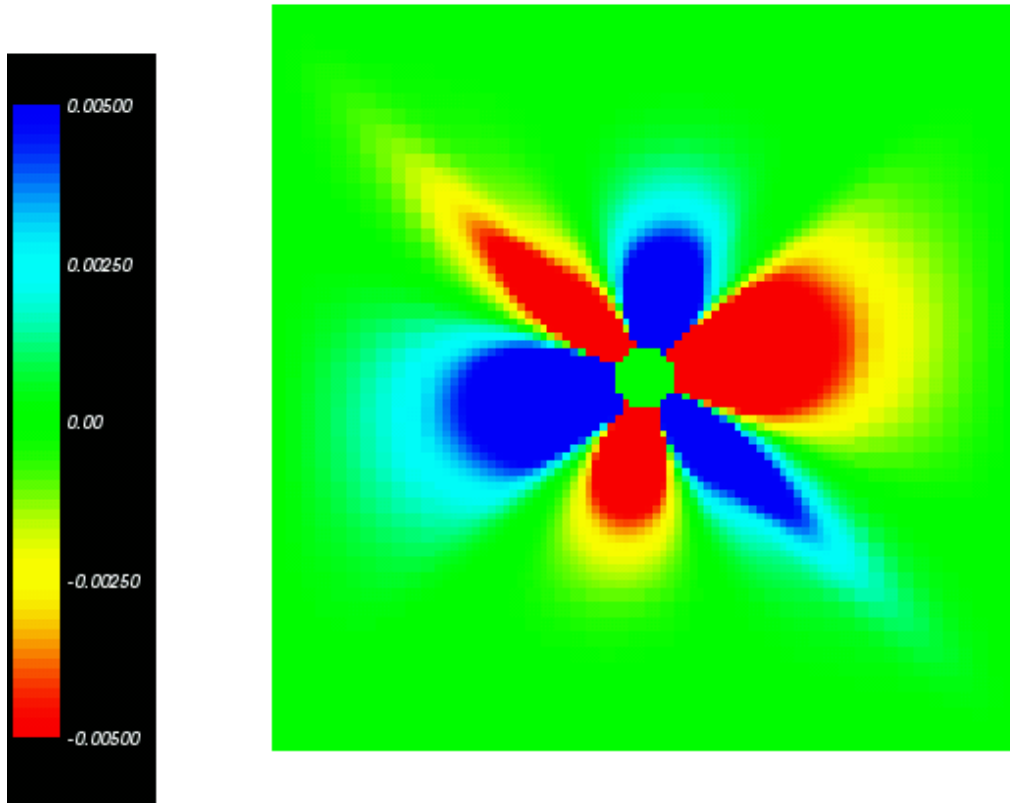
Figure 7.9: The $z = 0$ plane showing the error in g_{xx} at time $250M$ for the constrained simulation in Figure 7.3. The simulation at this point is going unstable, though no obvious coarse-fine interface errors ever appear.
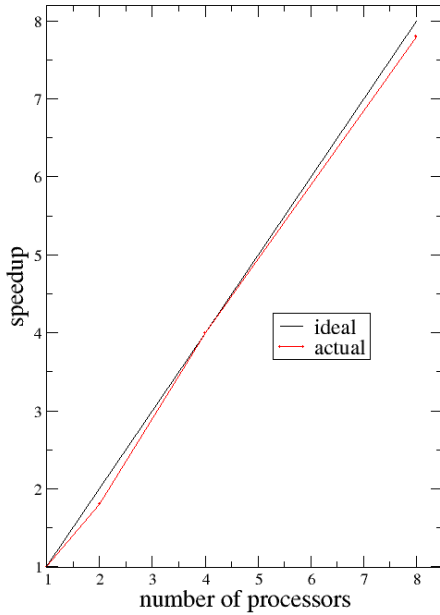
Figure 7.10: The speedup for a mesh refined simulation as a function of number of processors. The test case used to calculate the speedup was the constrained evolution example presented in section 7.2.
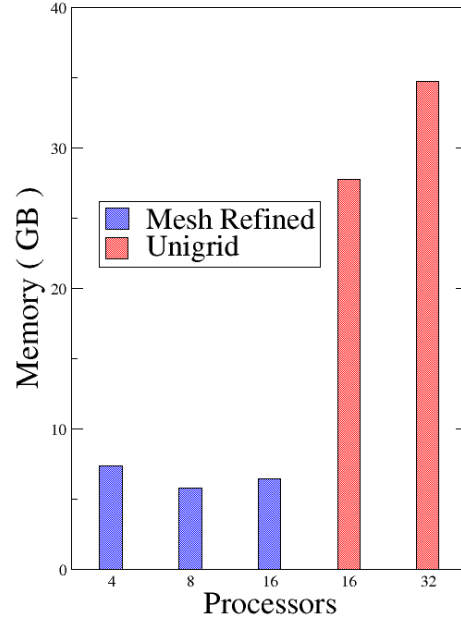
Figure 7.11: The total memory requirements for a Kerr-Schild black hole simulation with global domain $[-20M \ldots 20M]$ and finest resolution of $M/5$, comparing mesh refined and unigrid cases on selected numbers of processors. The mesh refined cases use one level of refinement extending from $[-5M \ldots 5M]$. The memory benefits alone warrant further study into mesh refinement.

Chapter 8

Constrained Evolution with Overlapping Grids

Improving the treatment of the black hole inner boundary is crucial to successfully evolving binary black holes with excision. Up to this point, I have discussed only Cartesian computational grids. Their concomitant nonsmooth excision regions have caused some difficulties in full $3 + 1$ simulations. This chapter looks at the effects of using smooth excision surfaces, accomplished by means of overlapping computational grids built from different coordinate systems. The motivations for this approach are given first, followed by the specific implementation details and results for stationary, nonrotating black holes. Next, the overlapping grid method is generalized for boosted black holes. Results from a variety of full $3 + 1$ simulations using ADM are presented to illustrate the stability benefits of smooth excision regions.

8.1 Motivation for Overlapping Grids

Excising the singularity from a black hole spacetime creates several computational difficulties. For a spherical mask function on a Cartesian grid, the excision region
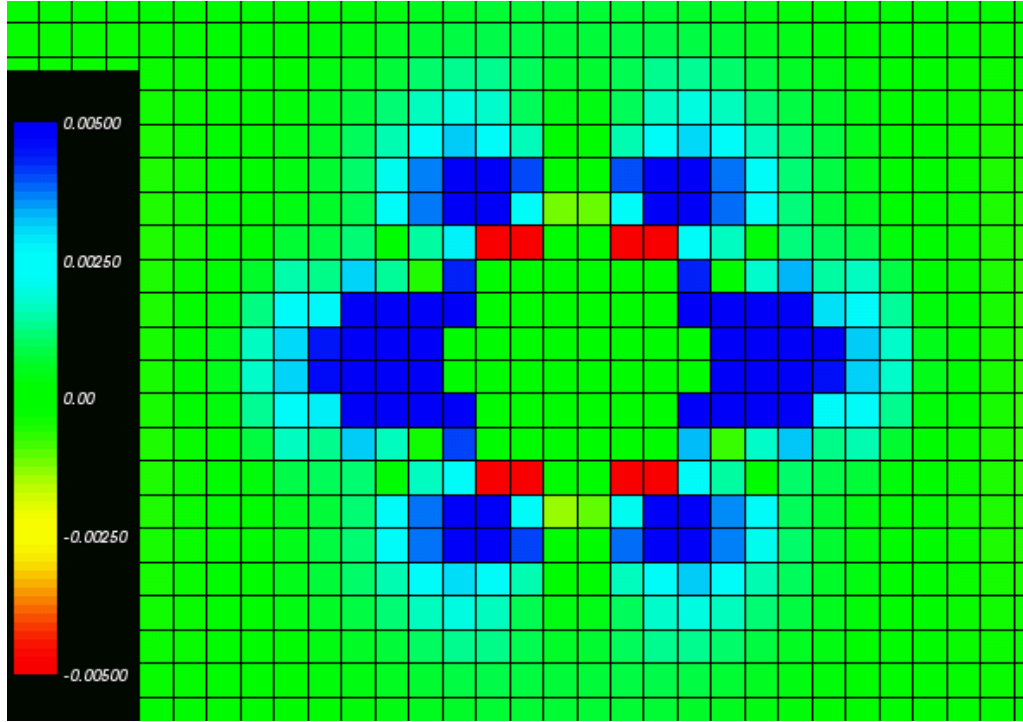
Figure 8.1: A close-up of the error in g_{xx} at $t = 50M$ along the $z = 0$ plane in the constrained evolution with resolution $M/7.5$ shown in Figure 6.15. The grid is shown to better display the influence of the jagged mask shape on the error pattern. The data is cell-centered.

appears rough and jagged. The jagged inner boundary of the simulation contributes to instabilities in an evolution. Figures 8.1 and 8.2 provide close-up views of the error in g_{xx} near the excision region for simulations at two different resolutions. The jagged shape of the mask distinctly contributes to the error pattern in g_{xx}, where alternating positive and negative errors are observed. The error pattern is influenced by inner boundary roughness less as the mask becomes better resolved and less jagged.

Causality problems may result due to the jagged shape of the excision region. Several researchers have already noted that cubical excision regions present causal-
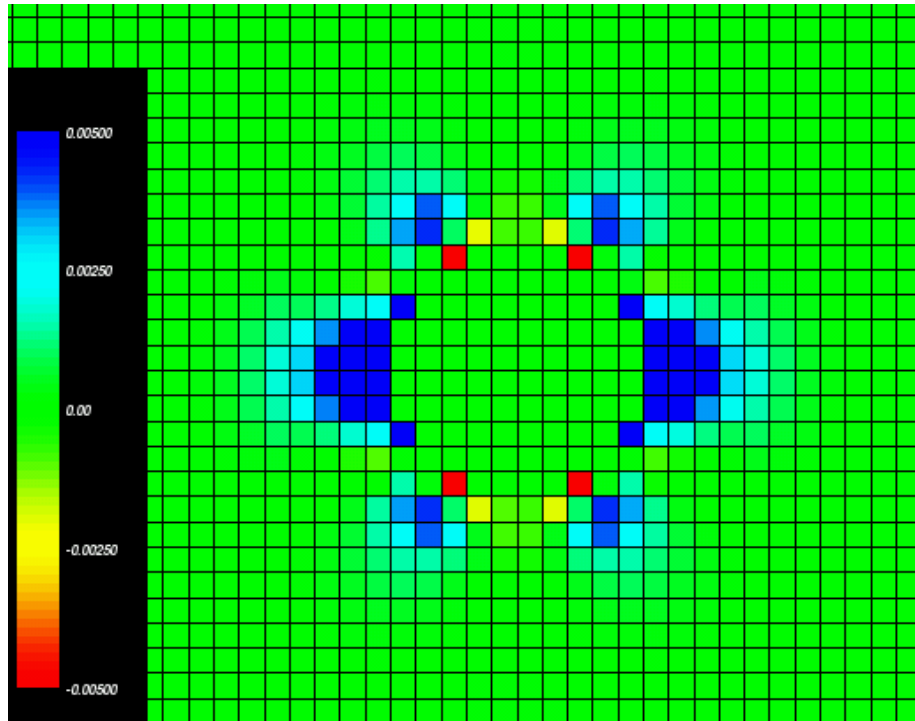
Figure 8.2: A close-up of the error in g_{xx} at $t = 50M$ along the $z = 0$ plane in the constrained evolution with resolution $M/10$ shown in Figure 6.15. The grid is shown to better display the influence of the jagged mask shape on the error pattern. The data is cell-centered. This higher resolution example shows an improvement in error compared to the $M/7.5$ case in Figure 8.1.

ity problems if the excision region is too large [63] [72]. The spatial extent of an acceptable cubical excision region is much smaller than the analytical radius within which events are causally disconnected from the rest of the slice. For instance, cubical excision in a Schwarzschild black hole must have sides less than $0.7698M$ in length to avoid causality problems [72]. This means that the entire cube must fit inside a sphere of radius $0.544M$ to avoid problems, a radius much smaller than the expected horizon radius of $2.0M$. Such small excision regions require high resolution to resolve the large gradients near a singularity. They also make it more difficult to keep the excision region centered on the singularity when evolving a boosted black hole spacetime. Concerns about cubical excision are not entirely irrelevant when discussing spherical excision on a Cartesian grid: the jagged edges of a Cartesian discretized sphere are cubes. Results presented in section 6.3 showed distinct improvements in constrained evolution by simply making the spherical excision region smaller, consistent with that predicted by analysis for cubical excision.

The ideal shape for the excision region is a smooth 2-sphere. This removes both the finite-differencing and causality problems associated with a jagged inner boundary. However, the spherical coordinates necessary for smooth spherical excision introduce two major obstacles: first, it is difficult to generalize spherical coordinate grids for multiple black hole spacetimes; and second, spherical coordinates possess coordinate singularities at the poles.

A solution to the first obstacle is given by G. Calabrese and D. Neilsen, who overlapped a spherical grid on a Cartesian grid to evolve a scalar field on a boosted black hole background in 2-D/axisymmetry [63]. This same approach can be used to evolve single and multiple boosted black hole spacetimes: each black hole excision region is a smooth 2-sphere accomplished with a spherical grid; the spherical grid overlaps a Cartesian grid in order to follow the trajectory of the singularity. This approach also eliminates the difficult extrapolation necessary to move an excision

123

region across a Cartesian grid. Further background on this is found in section 8.4.

A solution to the second obstacle consists of overlapping several different spherical grids so that the polar regions are never evolved. Various versions of this approach have been tried before by others in treating black hole spacetimes with excision [73] [74] [75]. The approach used here most closely resembles the overlapping grid approach of J. Thornburg [75], though six overlapping grids were used in his approach, while only two are used here. Specifics of the overlapping spherical grid approach used for the investigations in this chapter are given in section 8.2.

Overlapping a spherical grid with another spherical grid and a Cartesian grid comprises a unique way of achieving mesh refinement in numerical relativity. The overlapping spherical grids can use higher resolution than the global Cartesian grid. The overlapping spherical grids also possess the capability to follow the movement of a black hole across the Cartesian grid. While not true adaptive mesh refinement, the approach is more robust than the fixed mesh refinement presented in chapter 7.

8.2 Overlapping Spherical Grids

Coordinate singularities at the poles of spherical coordinate grids are avoided by overlapping two different spherical grids each with a different coordinate system. The first spherical grid uses standard spherical coordinates:

$$
\begin{aligned}
x &= r \sin \theta \cos \phi \\
y &= r \sin \theta \sin \phi \\
z &= r \cos \theta
\end{aligned}
\tag{8.1}
$$

for

$$r \in [r_{\min}, r_{\max}], \theta \in [\theta_{\min}, \pi - \theta_{\min}], \phi \in [0, 2\pi),$$

where x,y,z are the standard Cartesian coordinates, and $r_{\min}$, $r_{\max}$, and $\theta_{\min}$ are user specified parameters. Periodic boundary conditions are used in the ϕ direction.

The second spherical coordinate system

$$x = r\cos\theta$$
$$y = r\sin\theta\sin\phi$$
$$z = r\sin\theta\cos\phi \qquad (8.2)$$

for

$$r \in [r_{\min}, r_{\max}], \theta \in [\theta_{\min}, \pi - \theta_{\min}], \phi \in [0, 2\pi),$$

has its poles rotated by $\frac{\pi}{2}$ from the first spherical grid. The overlap region between the two grids eliminates the need to include the polar regions of either coordinate system in a simulation while still covering the entire sphere. Figures 8.3 and 8.4 show computational grids built using the two spherical coordinates systems. Figures 8.5 and 8.6 show how the two grids overlap at a fixed radius.

While the idea of overlapping spherical grids is simple enough, its implementation is not. Overlapping grids requires additional complexity to keep the codes parallel and highly scalable. Only minor modifications to the SAMRAI library were necessary to add multiple overlapping grid functionality. The interpolation between the two spherical grids is 6th order polynomial. Constraint solving capability across both spherical grids is also accomplished by using overlapping grid interpolation.

In addition to interpolation between the different grids, a coordinate transformation on the metric and extrinsic curvature tensors is also required. Originally, the spherical overlapping grids evolved the metric in Cartesian coordinates on the spherical grids. No transformation was needed with such an approach, but all derivatives with respect to spherical coordinates had to be converted by the chain rule to derivatives with respect to Cartesian coordinates. However, that approach proved to be unstable. Much better results were achieved by evolving the dynamical variables in same the coordinate system as the computational grid. Consequently, interpolated values between patches also have to undergo the usual transformation between

125
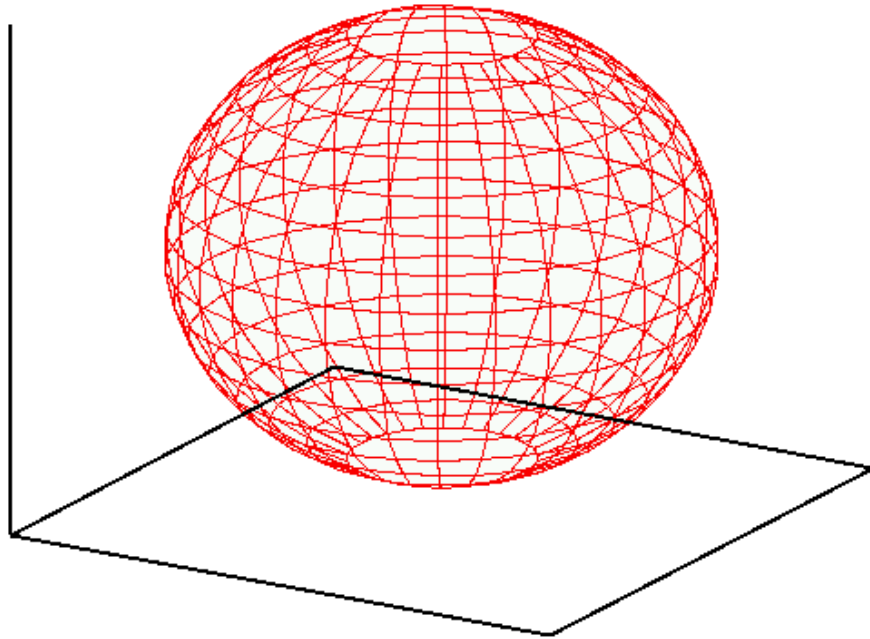
Figure 8.3: The first type of spherical grid used for black hole excision. This grid uses standard spherical coordinates. The polar regions are not included in the grid; $\theta_{\min}$ is 0.35.
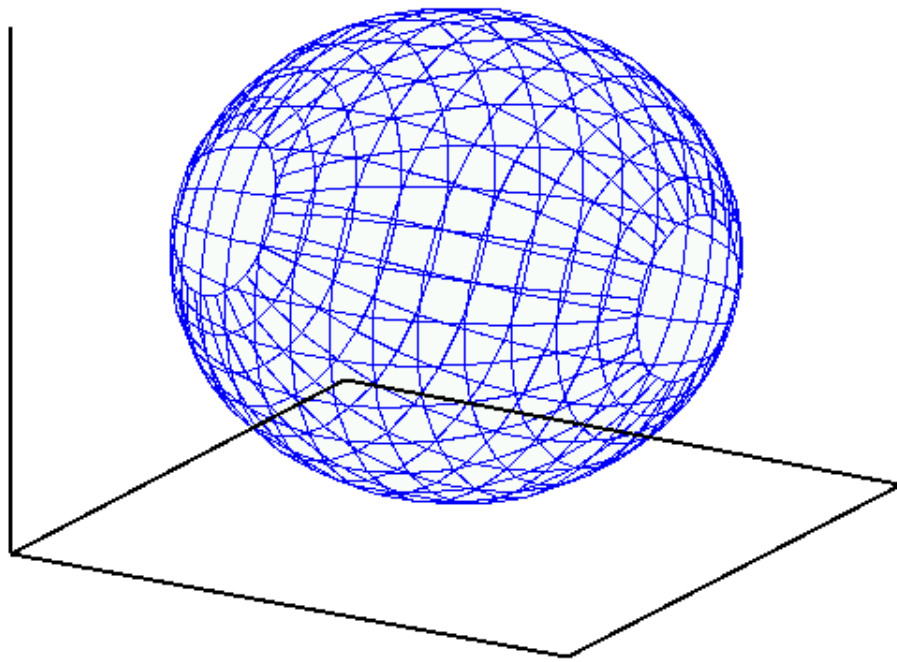
Figure 8.4: The second type of spherical grid used for black hole excision. The poles of this grid are rotated by $\frac{\pi}{2}$ from the poles of the first overlapping grid in Figure 8.3. The polar regions are not included in the grid; $\theta_{\min}$ is 0.35.
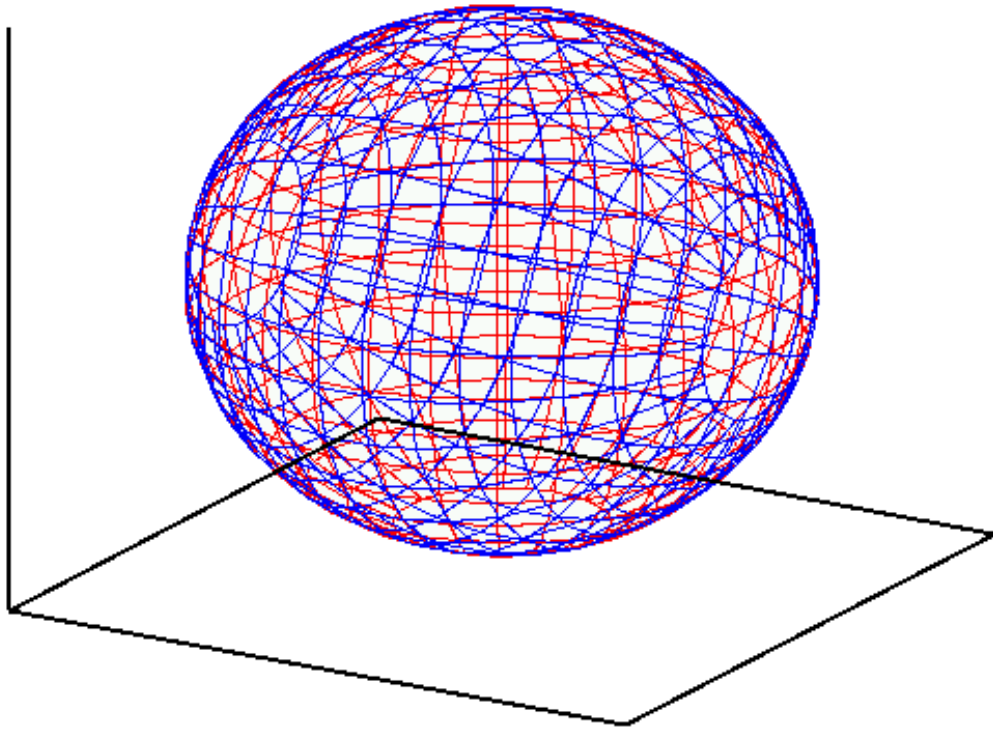
Figure 8.5: Two overlapping spherical grids at a fixed radius using $\theta_{\min} = 0.35$. The polar regions of the red grid are covered by blue grid, and vice versa. Neither computational grid includes its own poles; however, by overlapping both grids the entire sphere is modelled.
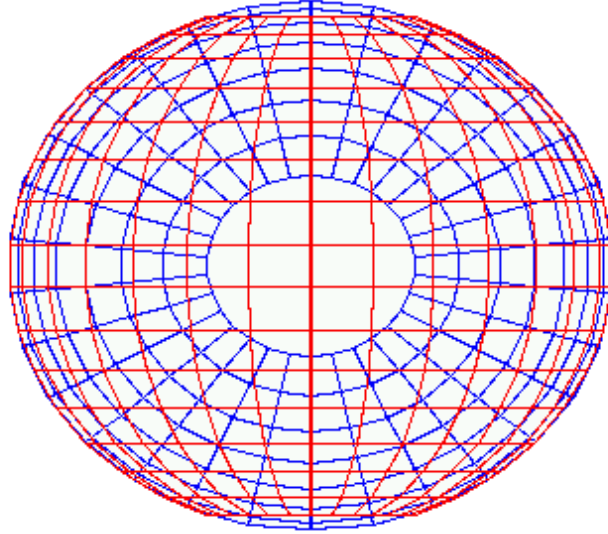
Figure 8.6: The north pole of the blue grid, which is modelled by the red grid. Both grids use $\theta_{\min} = 0.35$.

coordinate systems for covariant tensors:

$$X'_{ij} = \frac{\partial x^m}{\partial x'^i} \frac{\partial x^n}{\partial x'^j} X_{mn}. \tag{8.3}$$

8.3 Overlapping Spherical/Cartesian Grids

Overlapping two spherical grids on a Cartesian grid adds considerable complexity to a simulation. The process bears several resemblances to the refinement and restriction operations described in chapter 7 for use with mesh refinement. In this case, however, the interpolation is followed by a transformation between coordinate systems for the metric and extrinsic curvature tensors.

The outer boundary of the overlapping spherical grids is supplied field values from the Cartesian grid. The inner boundary of the Cartesian grid is supplied field values from the appropriate overlapping spherical grid. For successful interpolation,

the spherical grid uses a smaller excision radius than that used by the Cartesian grid. The spatial extent of interpolation from the spherical grid to the Cartesian grid is a parameter choice supplied by the user. The interpolation process is illustrated in Figure 8.7.

Overlapping spherical and Cartesian grids easily eliminates features due to the jagged shape of a Cartesian grid mask, shown in Figures 8.1 and 8.2. Figure 8.8 shows the error in g_{xx} at time $50M$ in a simulation similar to those in Figures 8.1 and 8.2, but with a lower resolution and using overlapping spherical–Cartesian grids.

To the knowledge of the author, only one other toolkit is publicly available which is capable of overlapping multiple Cartesian and spherical grids, each of different size. That toolkit, Overture [76], is not yet fully parallelized. While it is clear that the standard SAMRAI toolkit was not intended to provide Cartesian–spherical overlapping grid support, SAMRAI with minor enhancements comprises a robust parallel framework for successfully overlapping various grids built with different coordinate systems.

8.4   Boosted Black Holes with Overlapping Grids

Evolving boosted black holes adds two major complications to the technique of overlapping spherical and Cartesian grids. At the same time, however, overlapping spherical and Cartesian grids solve a very major problem inherent to evolving boosted black holes with Cartesian grids alone.

8.4.1   Lorentz Contracted Excision Surfaces

The first major complication of evolving boosted black holes with overlapping spherical grids relates to the shape of the excision surface. Boosted black holes experience a coordinate Lorentz contraction in the direction of the boost. A spherical excision
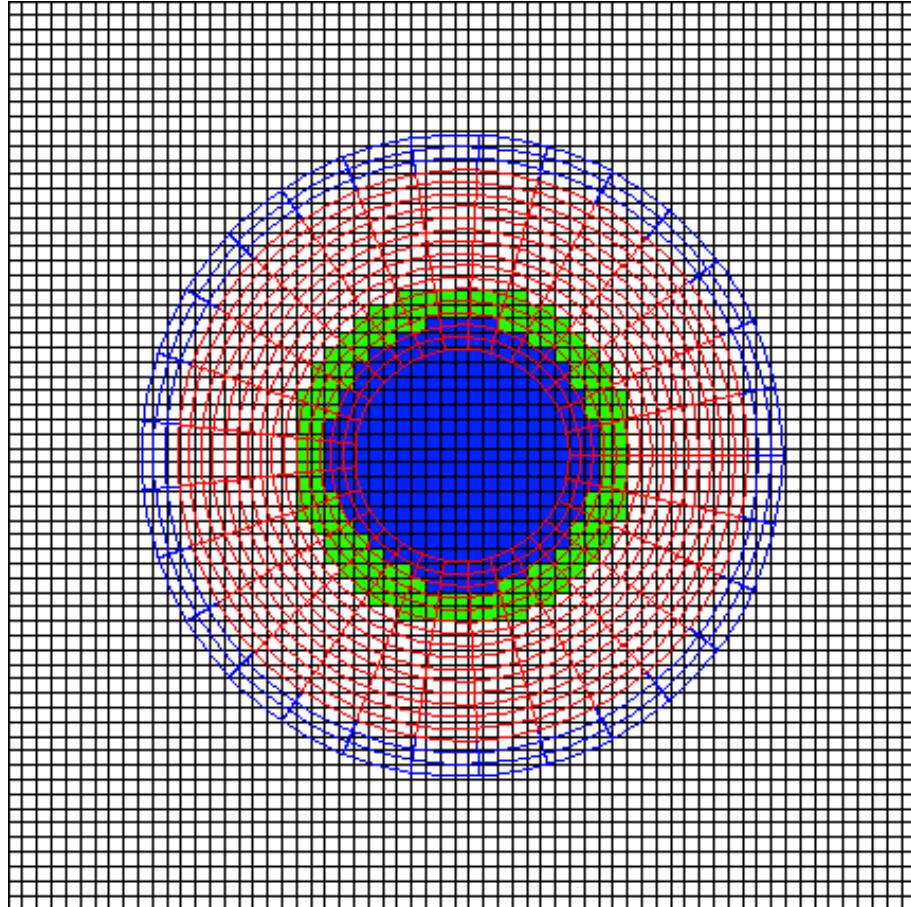
Figure 8.7: A 2-D slice of the Cartesian–spherical overlapping grids for a nonrotating, stationary black hole. The Cartesian excision region is colored blue. The Cartesian cells colored green adjacent to the Cartesian excision region are provided field values by interpolation and transformation from the overlapping spherical grid. The outer boundary of the spherical grid, colored blue, is supplied field values by interpolation and transformation from the Cartesian grid. Note that the spherical grid excision radius is smaller than the Cartesian grid excision radius.
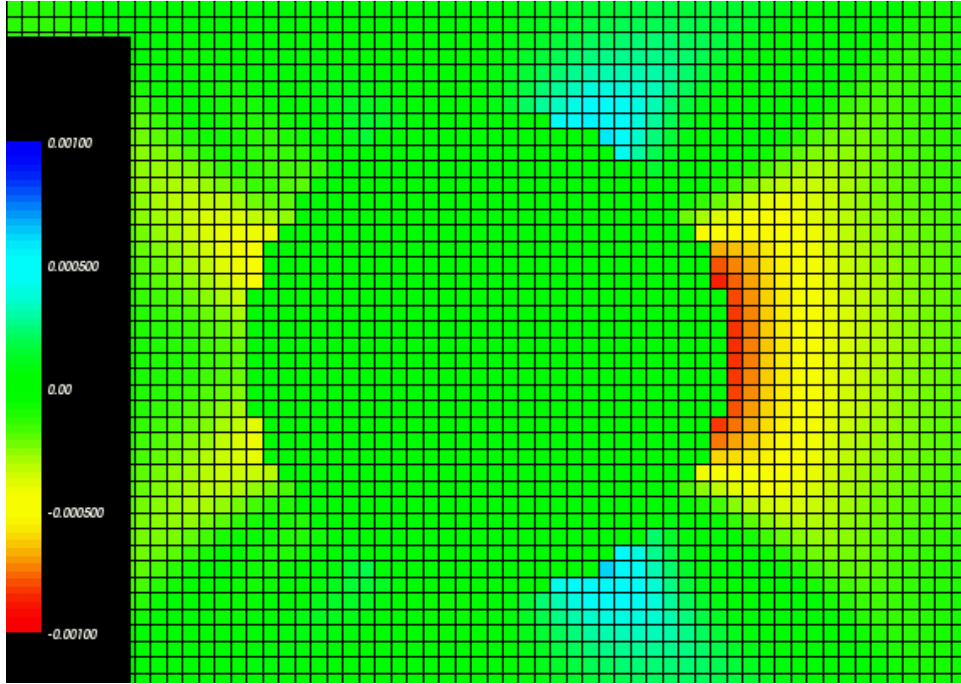
Figure 8.8: A close-up of the error in g_{xx} on a Cartesian grid along the $z = 0$ plane at time $50M$ for a nonrotating, stationary black hole simulation using overlapping spherical and Cartesian grids. The Cartesian grid domain was $[-10M \ldots 10M]$ with resolution $M/5$. The Cartesian excision radius was $2.0M$. The spherical domain extended from radius $1.5M$ to $4.0M$, using $(26, 30, 50)$ zones in the (r, θ, ϕ) direction. The $\theta_{\min}$ parameter was 0.6. The constraints were solved on all three grids every $0.05M$. The overlapping spherical grids in this simulation have eliminated the features evident in Figures 8.1 and 8.2 resulting from the jagged shape of the Cartesian mask. While the error appears slightly more asymmetrical here than in Figures 8.1 and 8.2, the size of the error is also five times smaller than in those Figures. Also, the solution had not yet relaxed to a stationary value at $50M$ in the overlapping grids case.

surface is not ideal for evolving a naturally spheroidal surface. To address this concern, overlapping ellipsoidal coordinates are used instead of spherical coordinates for the overlapping grids immediately surrounding the excision region. They are related to Cartesian coordinates as follows:

$$
\begin{aligned}
x &= a \cosh r \sin \theta \cos \phi \\
y &= a \cosh r \sin \theta \sin \phi \\
z &= a \sinh r \cos \theta
\end{aligned}
$$

(8.4)

for

$$
r \in [r_{\min}, r_{\max}] , \theta \in [\theta_{\min}, \pi - \theta_{\min}] , \phi \in [0, 2\pi) ,
$$

where a is a parameter related to the mask radius and the boost velocity in the z direction. Note that this parameter 'a' is not the same as the 'a' that appears in the Kerr solution, though a stationary Kerr hole does have a spheroidal horizon. To avoid coordinate singularities at the poles, a second coordinate system is used with poles rotated $\pi/2$ from the previous set of ellipsoidal coordinates:

$$
\begin{aligned}
x &= a \cosh r \cos \theta \\
y &= a \cosh r \sin \theta \sin \phi \\
z &= a \sinh r \sin \theta \cos \phi
\end{aligned}
$$

(8.5)

for

$$
r \in [r_{\min}, r_{\max}] , \theta \in [\theta_{\min}, \pi - \theta_{\min}] , \phi \in [0, 2\pi) ,
$$

These coordinates describe the excision surface of a boosted black hole in the z direction. For boosts in arbitrary directions, the axes are redefined.

The ellipsoidal coordinates given in Eq. (8.4) and (8.5) become more spherical as the radius from the center increases. As the radius decreases, the coordinates

become more elliptical. See Figure 8.9. The coordinate parameter a allows the inside surface of the coordinates to exactly replicate the Lorentz contracted inner excision surface of an arbitrarily boosted black hole. The excision surface is the spheroidal surface with the ellipsoidal r coordinate given by:

$$r_{\min} = \tanh^{-1} \frac{1}{\gamma},\tag{8.6}$$

where $\gamma \equiv (1 - v^2)^{-1/2}$. The coordinate parameter a is related to the specified mask radius in the nonboosted direction and $r_{\min}$:

$$a = \frac{\text{mask radius}}{\cosh r_{\min}}.\tag{8.7}$$

The resulting surface at $r = r_{\min}$ is

$$x^2 + y^2 + \frac{z^2}{1/\gamma^2} = (\text{mask radius})^2.\tag{8.8}$$

This exactly coincides with the excision surface, which is a sphere in the rest frame of the hole. In particular, it coincides with the non-spinning boosted black hole horizon when the mask radius is $2M$. The correct Lorentz contraction ratio between the semi-major and semi-minor axis of the excision surface is preserved regardless of the specified mask radius. Notice, however, that other black hole frame spherical surfaces do not map to constant spheroidal r surfaces. The excision surface grids for a black hole boosted with velocity 0.9 are shown Figures 8.10, 8.11, and 8.12.

8.4.2   Keeping the Singularity Centered

The second major complication of evolving boosted black holes with overlapping spherical grids is how to move the hole. In a Cartesian grid, the excision region moves with the singularity as the boosted black hole moves across the grid. However, for spherical grids, the excision region must remain in the center of the grids. G. Calabrese and D. Neilsen dealt with this problem by using special relativity: they boosted the frame of their spherical grid so that the black hole was stationary on that

Oblate Spheroidal Coordinates
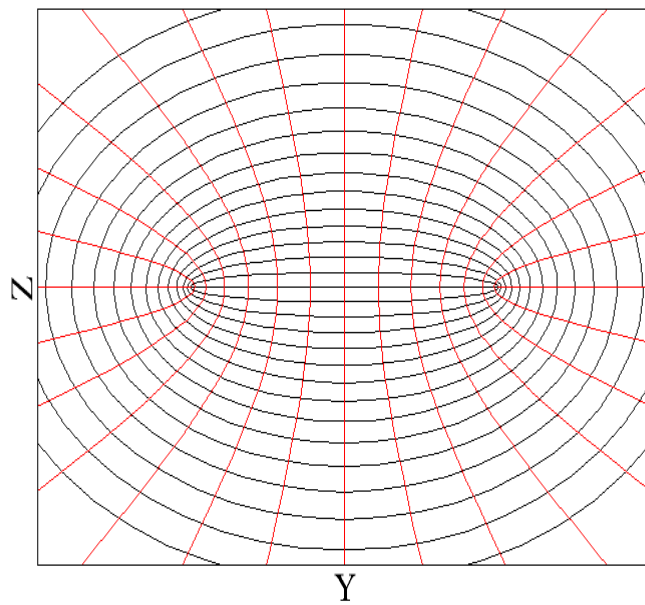
Figure 8.9: Oblate spheroidal coordinates–the ellipsoidal coordinates given in Eq (8.4). Lines of constant r are black; lines of constant θ are red. The coordinates become more elliptical as the radius becomes smaller.
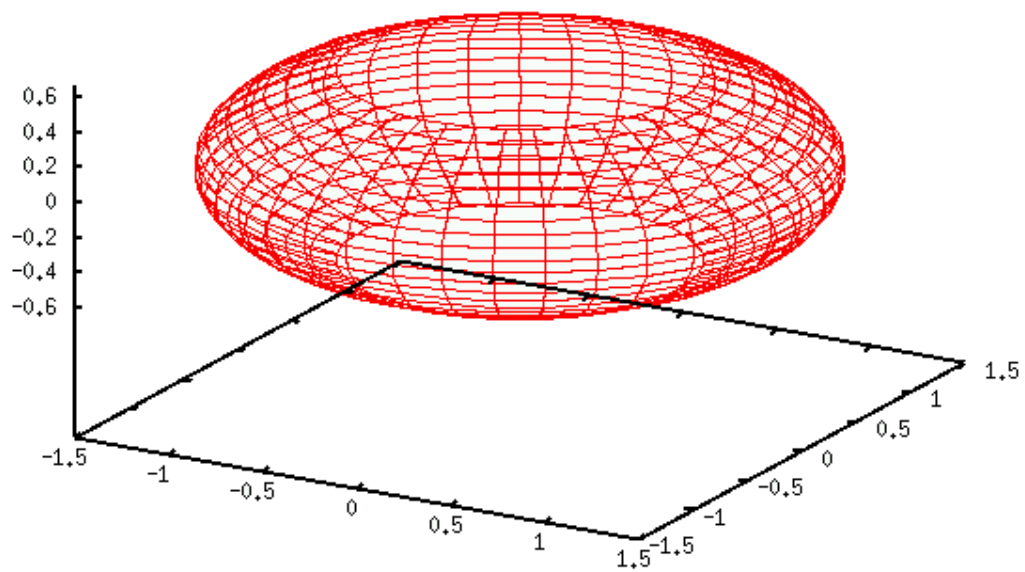
Figure 8.10: First of two overlapping grids at the excision surface for a black hole boosted with velocity 0.9 in the z direction. The mask radius in the nonboosted direction is $1.5M$. $\theta_{\min}$ is 0.6.
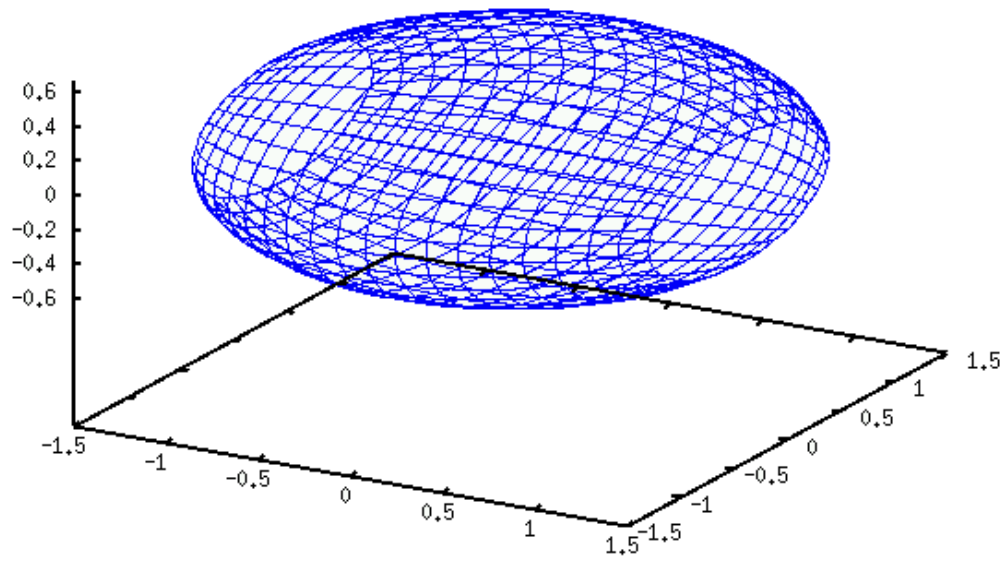
Figure 8.11: Second of two overlapping grids at the excision surface for a black hole boosted with velocity 0.9 in the z direction. The mask radius in the nonboosted direction is $1.5M$. $\theta_{\min}$ is 0.6.
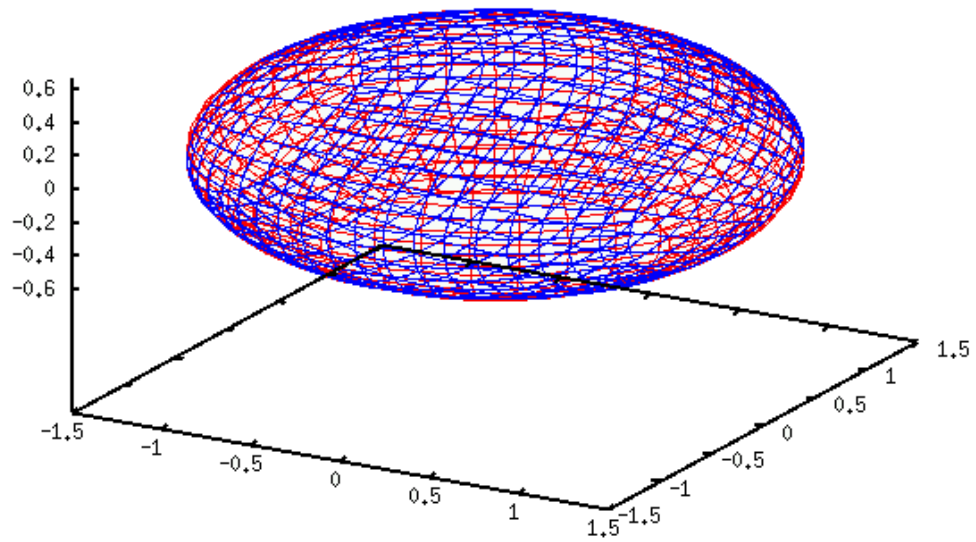
Figure 8.12: Two overlapping grids at the excision surface for a black hole boosted with velocity 0.9 in the z direction. The mask radius in the nonboosted direction is $1.5M$. $\theta_{\min}$ is 0.6.

grid [63]. This approach poses immediate difficulties for binary black hole evolutions, where individual black hole trajectories are not known. A simpler approach is to use the shift vector, β^i, to move the hole on the spherical grid while keeping the excision region in the same place.

As pointed out in section 2.2, the shift vector describes the time evolution of the spatial coordinates in a simulation. Every timestep there is an offset in the spatial coordinates of size $\beta^i dt$ (recall Figure 2.1). For black hole evolutions, this offset is radially away from the black hole and keeps points from falling into the hole. Modifying the shift vector can ensure that a boosted black hole remains in the center of a simulation grid.

To ensure that a black hole boosted with velocity V^i remains in the center of a pair of overlapping spherical grids, the shift vector is increased by the boost velocity:

$$\beta^i_{\text{new}} = \beta^i + V^i. \tag{8.9}$$

Using the new shift vector in evolving fields on the spherical grids constitutes a coordinate transformation that ensures the black hole remains centered in the overlapping grids.

To illustrate this, consider the following example developed by R. Matzner [77]. Begin by examining the metric components for a nonrotating Kerr-Schild black hole boosted with speed v in the $+x$ direction. For simplicity, consider only those components along the x axis which are nonconstant: g_{xx}, g_{tt}, and g_{tx}. It will be shown that the time derivative of g_{xx} for the boosted black hole vanishes when using the modified shift vector, Eq. (8.9), assuring that the black hole remains where it started on the computational grid, regardless of the boost.

The nonconstant x–t metric components for a nonrotating, stationary Kerr-

139

Schild black hole along the x axis are:

$$\alpha = \frac{1}{\sqrt{1 + \frac{2M}{|x|}l_t^2}} \tag{8.10}$$

$$\beta_x = \frac{2M}{|x|}l_t l_x \tag{8.11}$$

$$g_{tt} = -\alpha^2 + \beta^i \beta_i \tag{8.12}$$

$$g_{tx} = \beta_x \tag{8.13}$$

$$g_{xx} = 1 + \frac{2M}{|x|}l_x^2, \tag{8.14}$$

where $(l_t, l_x) = (1, 1)$ if $x > 0$ and $(l_t, l_x) = (1, -1)$ if $x < 0$. Now perform a Lorentz transformation:

$$x' = \gamma(x + vt) \tag{8.15}$$

$$t' = \gamma(t + vx), \tag{8.16}$$

where $\gamma \equiv (1 - v^2)^{-1/2}$. The primed frame is one in which the hole is moving with speed v in the $+x'$ direction. The inverse transformation is given by:

$$x = \gamma(x' - vt') \tag{8.17}$$

$$t = \gamma(t' - vx'). \tag{8.18}$$

Boosting the null vector l_μ,

$$l'_t = \Lambda_t{}^t l_t + \Lambda_t{}^x l_x \tag{8.19}$$

$$l'_x = \Lambda_x{}^t l_t + \Lambda_x{}^x l_x, \tag{8.20}$$

results in the following:

for $x > 0$,

$$l'_t = \gamma(1 + v) \tag{8.21}$$

$$l'_x = \gamma(1 + v); \tag{8.22}$$

for $x < 0$,

$$l'_t = \gamma(1-v) \tag{8.23}$$

$$l'_x = -\gamma(1-v). \tag{8.24}$$

Using these relations, the boosted fields are:

for $x > 0$,

$$\alpha = \frac{1}{\sqrt{1 + \frac{2M}{|\gamma(x'-vt')|}\gamma^2(1+v)^2}} \tag{8.25}$$

$$\beta_{x'} = \frac{2M}{|\gamma(x'-vt')|}\gamma^2(1+v)^2 \tag{8.26}$$

$$g_{x'x'} = 1 + \frac{2M}{|\gamma(x'-vt')|}\gamma^2(1+v)^2 ; \tag{8.27}$$

for $x < 0$,

$$\alpha = \frac{1}{\sqrt{1 + \frac{2M}{|\gamma(x'-vt')|}\gamma^2(1-v)^2}} \tag{8.28}$$

$$\beta_{x'} = -\frac{2M}{|\gamma(x'-vt')|}\gamma^2(1-v)^2 \tag{8.29}$$

$$g_{x'x'} = 1 + \frac{2M}{|\gamma(x'-vt')|}\gamma^2(1-v)^2. \tag{8.30}$$

Note that the expression for $g_{x'x'}$ can be simplified considerably by writing it in terms of $\beta_{x'}$:

for $x > 0$,

$$g_{x'x'} = 1 + \beta_{x'} \tag{8.31}$$

for $x < 0$,

$$g_{x'x'} = 1 - \beta_{x'}. \tag{8.32}$$

The general definition of the extrinsic curvature tensor was given in Eq. (2.22):

$$-2\alpha K_{ij} = \dot{g}_{ij} - \left(\beta^k g_{ij,k} + g_{kj}\beta^k_{,i} + g_{ik}\beta^k_{,j}\right). \tag{8.33}$$

141

Along the x' axis, this simplifies considerably:

$$-2\alpha K_{x'x'} = \partial_{t'} g_{x'x'} - \left[\beta^{x'} \partial_{x'} g_{x'x'} + 2g_{x'x'} \partial_{x'} \beta^{x'}\right] \tag{8.34}$$

$$= \partial_{t'} g_{x'x'} - \left[g^{x'x'} \beta_{x'} \partial_{x'} g_{x'x'} + 2g_{x'x'} \partial_{x'} \left(g^{x'x'} \beta_{x'}\right)\right] \tag{8.35}$$

$$= \partial_{t'} g_{x'x'} - \left[2\partial_{x'} \left(g^{x'x'} g_{x'x'} \beta_{x'}\right) - g^{x'x'} \beta_{x'} \partial_{x'} g_{x'x'}\right] \tag{8.36}$$

$$= \partial_{t'} g_{x'x'} - \left[2\partial_{x'} \beta_{x'} - g^{x'x'} \beta_{x'} \partial_{x'} g_{x'x'}\right]. \tag{8.37}$$

Consider the case for $x > 0$. Using Eq. (8.31) to further simplify Eq. (8.37):

$$-2\alpha K_{x'x'} = \partial_{t'} g_{x'x'} - \left(2\partial_{x'} \beta_{x'} - g^{x'x'} \beta_{x'} \partial_{x'} \beta_{x'}\right) \tag{8.38}$$

$$= \partial_{t'} g_{x'x'} - \partial_{x'} \beta_{x'} \left(2 - g^{x'x'} \beta_{x'}\right) \tag{8.39}$$

$$= \partial_{t'} g_{x'x'} - \partial_{x'} \beta_{x'} \left(2 - \frac{\beta_{x'}}{1 + \beta_{x'}}\right) \tag{8.40}$$

$$= \partial_{t'} g_{x'x'} + \frac{\beta_{x'}}{|x' - vt'|} \left(\frac{2 + \beta_{x'}}{1 + \beta_{x'}}\right). \tag{8.41}$$

The t' derivative of $g_{x'x'}$, found using Eq. (8.26) and (8.31), is:

$$\partial_{t'} g_{x'x'} = \beta_{x'} \frac{v}{|x' - vt'|}. \tag{8.42}$$

Using Eq. (8.42), Eq. (8.41) now becomes:

$$-2\alpha K_{x'x'} = \frac{\beta_{x'}}{|x' - vt'|} \left(v + \frac{2 + \beta_{x'}}{1 + \beta_{x'}}\right). \tag{8.43}$$

An essential feature is that the term proportional to v here arises from the metric t' derivative.

Now introduce a new spatial coordinate ξ and corresponding time coordinate η. ξ coincides with x' for each $t' = $ constant slice. Also, use the modified shift vector:

$$\beta^\xi = \beta^{x'} + V \tag{8.44}$$

where V is a constant. While $-2\alpha K_{\xi\xi}$ is equal to $-2\alpha K_{x'x'}$ for each $t' = $ constant slice, $\partial_\eta g_{\xi\xi}$ is not equal to $\partial_{t'} g_{x'x'}$. To find the value of $\partial_\eta g_{\xi\xi}$, start with the expression for $-2\alpha K_{\xi\xi}$ using Eq. (8.34):

$$-2\alpha K_{\xi\xi} = \partial_\eta g_{\xi\xi} - \left[\beta^\xi \partial_\xi g_{\xi\xi} + 2g_{\xi\xi} \partial_\xi \beta^\xi\right] \tag{8.45}$$

142

$$-2\alpha K_{x'x'} = \partial_\eta g_{\xi\xi} - \left[\left(\beta^{x'} + V\right)\partial_{x'}g_{x'x'} + 2g_{x'x'}\partial_{x'}\left(\beta^{x'} + V\right)\right]. \quad (8.46)$$

Using the results already derived in Eq. (8.41), Eq. (8.46) becomes:

$$-2\alpha K_{x'x'} = \partial_\eta g_{\xi\xi} + \frac{\beta_{x'}}{|x' - vt'|}\left(\frac{2 + \beta_{x'}}{1 + \beta_{x'}}\right) - V\partial_{x'}g_{x'x'} \quad (8.47)$$

$$= \partial_\eta g_{\xi\xi} + \frac{\beta_{x'}}{|x' - vt'|}\left(\frac{2 + \beta_{x'}}{1 + \beta_{x'}}\right) - V\partial_{x'}\beta_{x'} \quad (8.48)$$

$$= \partial_\eta g_{\xi\xi} + \frac{\beta_{x'}}{|x' - vt'|}\left(\frac{2 + \beta_{x'}}{1 + \beta_{x'}}\right) + V\frac{\beta_{x'}}{|x' - vt'|}. \quad (8.49)$$

A comparison of Eq. (8.49) and Eq. (8.43) immediately leads to the conclusion that if $V = v$, i.e. if V is the magnitude and sign of the hole velocity, then

$$\partial_\eta g_{\xi\xi} = 0. \quad (8.50)$$

Similar analysis leads to the same conclusion in the case for $x < 0$. Using a shift vector that has been increased by the boost velocity, as specified in Eq. (8.9), ensures that a boosted black hole remains stationary on a computational grid regardless of the boost velocity.

8.4.3 Avoiding Extrapolation

The most significant benefit of evolving boosted black holes with overlapping spherical grids is freedom from sensitive extrapolation. When evolving a boosted black hole on a Cartesian grid alone, the mask follows the singularity as the black hole moves across the grid. As the excision region moves, points that were formerly masked are filled in with field values via extrapolation. See Figure 8.13. This extrapolation tends to be extremely sensitive and a source of considerable instability in boosted black hole evolutions. With overlapping spherical grids next to the excision region, points once masked but now evolved can be filled in with values interpolated from the overlapping grids. See Figure 8.14.
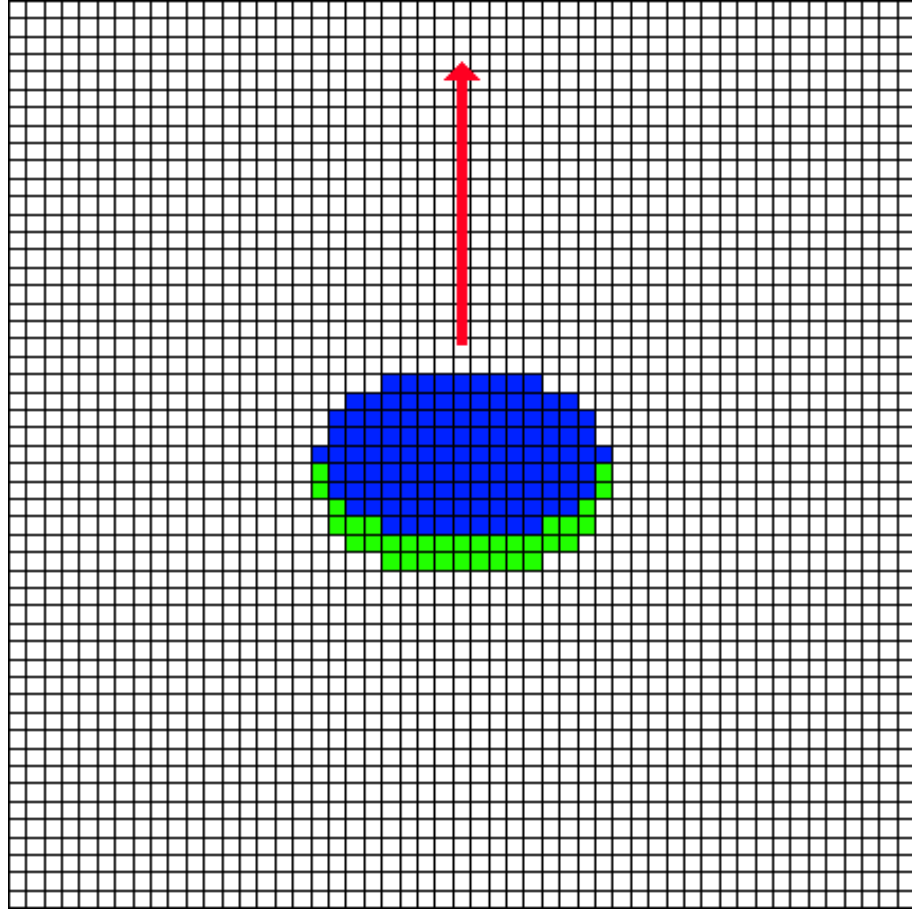
Figure 8.13: A 2-D slice of the Cartesian grid for a nonrotating black hole boosted with velocity 0.9. The excision region is colored blue. The cells colored green, which had been excised but were subsequently returned to the computation due to the motion of the mask, are provided field values by extrapolation from neighboring non-excised points. This approach is generally very sensitive to the extrapolation technique chosen and almost always troublesome.
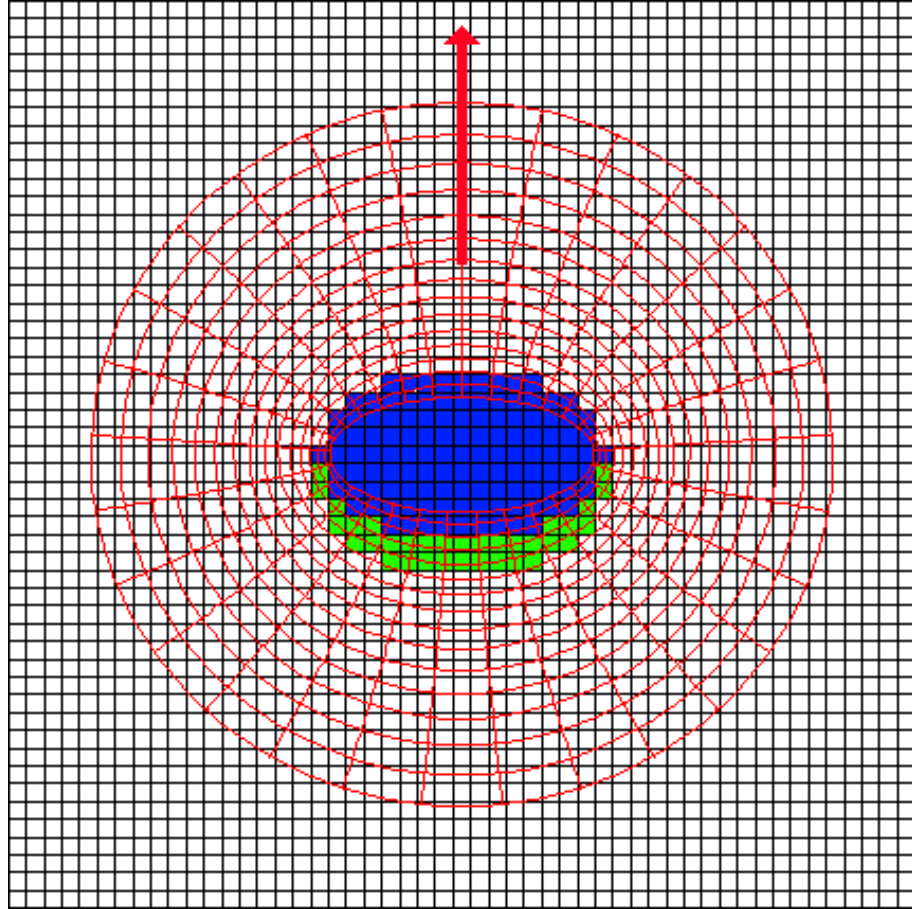
Figure 8.14: A 2-D slice of the Cartesian–spheroidal overlapping grids for a nonrotating black hole boosted with velocity 0.9. The Cartesian excision region is colored blue. The Cartesian cells colored green, which had been excised but were subsequently returned to the computation due to the motion of the mask, are provided field values by interpolation and transformation from the overlapping spheroidal grid. This approach avoids the sensitive extrapolation illustrated in Figure 8.13.

Constrained evolution figures prominently in successfully evolving a boosted black hole with overlapping spheroidal grids. Figure 8.15 shows the log of the rms-norm for the Hamiltonian constraint in simulations evolving a nonrotating black hole boosted with velocity 0.5 in the z direction. Results for constrained and unconstrained attempts at two different resolutions are displayed. These simulations used overlapping spheroidal grids to evolve the boosted black hole. The black hole was kept in the center of the grids by means of modifying the shift vector according to Eq. (8.9). The interpolation used between the two spheroidal grids was sixth order polynomial. These particular cases did not employ an overlapping Cartesian grid; the outer boundary of the grids was supplied the analytic values for a boosted black hole. Regardless of this simplification, the unconstrained cases were unstable after $\sim 40M$. The constrained cases, however, never went unstable.

8.4.4 Spheroidal-Cartesian Overlap results

The best test of the overlapping grid strategy is to evolve a boosted black hole with overlapping spheroidal *and* Cartesian computational grids. Figures 8.16–8.21 show 2-D slices at various times from a 3-D simulation evolving a boosted black hole with speed 0.5 in the z direction on a Cartesian domain of $[-10M \ldots 10M]$ with overlapping spheroidal grids. Owing to the small domain size and simple boundary condition employed (Dirichlet), errors from the boundary appear as the hole moves across the grid. However, the fields next to the singularity, which normally experience oscillations when using a Cartesian grid alone, here appear well-behaved and stable as the hole moves across the Cartesian grid. The max-norm of the Hamiltonian constraint is shown in Figure 8.22.
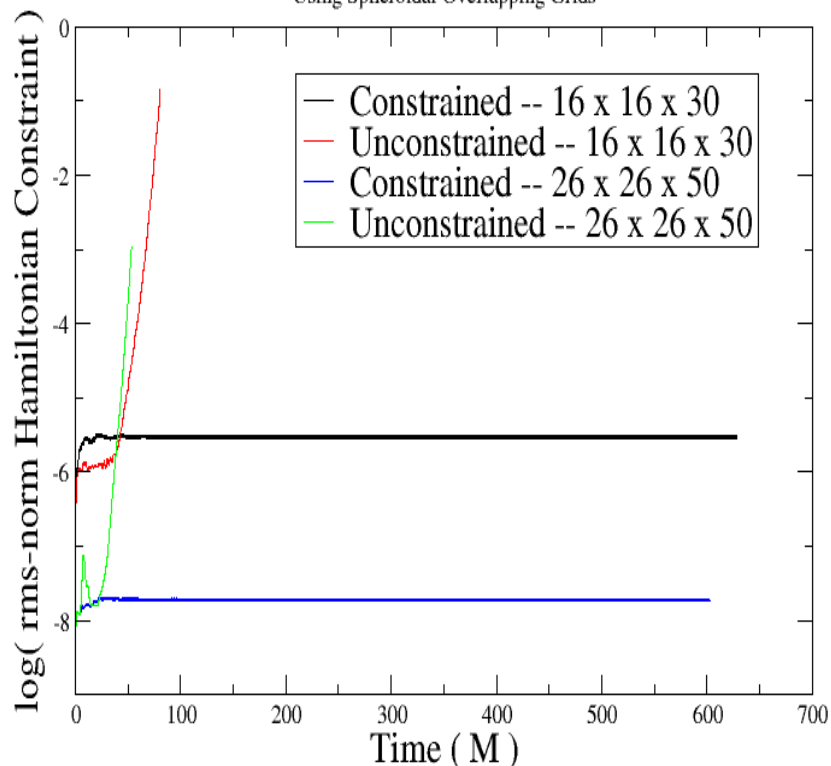
Figure 8.15: The log of the rms-norm for the Hamiltonian constraint violation in simulations evolving a nonrotating black hole boosted with velocity 0.5 in the z direction using the analytic lapse. The simulations only employed overlapping spheroidal grids; no Cartesian overlapping grid was used in this series of experiments. The outer boundary of the spheroidal grids was supplied the analytic values for boosted black hole fields. The boosted hole was kept in the center of the spheroidal grids throughout the simulation by means of the modified shift vector, Eq. (8.9). The excision radius was $1.5M$ in the nonboosted direction ($1.3M$ in the boosted direction). The outer boundary was at radius $3M$. In the constrained cases the constraints were solved over the entire domain except for those points which were within radius $1.76M$ in the nonboosted direction and $1.6M$ in the boosted direction. The number of (r,θ,ϕ) zones in the grid was either $(16, 16, 30)$ or $(26, 26, 50)$. $\theta_{\min}$ was 0.6. There is a high-frequency oscillation in the rms-norm of the Hamiltonian constraint for the constrained cases, resulting in the thicker linewidths evident after $t = 50M$.
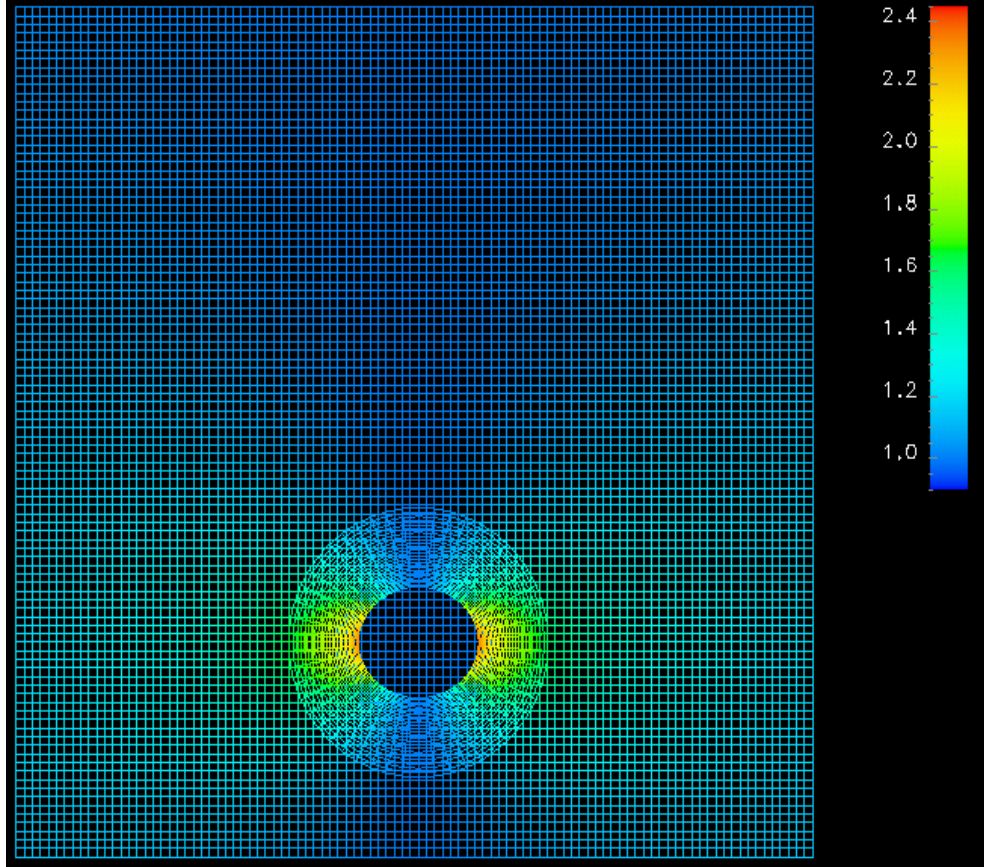
Figure 8.16: The $x = 0$ plane for g_{yy} at the initial time in a simulation boosting a nonrotating Kerr-Schild black hole in the z direction with speed 0.5. The simulation used both overlapping spheroidal and Cartesian computational grids, shown here, to ensure a smooth excision surface and avoid extrapolation. The Cartesian computational domain was $[-10M \ldots 10M]$ with resolution $M/5$. The Cartesian excision radius was $2.0M$. The spheroidal domain excision radius was $1.5M$ in the nonboosted direction ($1.3M$ in the boosted direction). The spheroidal domain extended out to a radius of $3.25M$ and used $(26, 30, 50)$ zones in the (r, θ, ϕ) direction. $\theta_{\min}$ was 0.6. The hole was placed initially at $z = -5M$ on the Cartesian grid. The lapse was analytic. Interpolation between the three grids was 6th order polynomial. The constraints on all three grids were solved every $0.05M$.
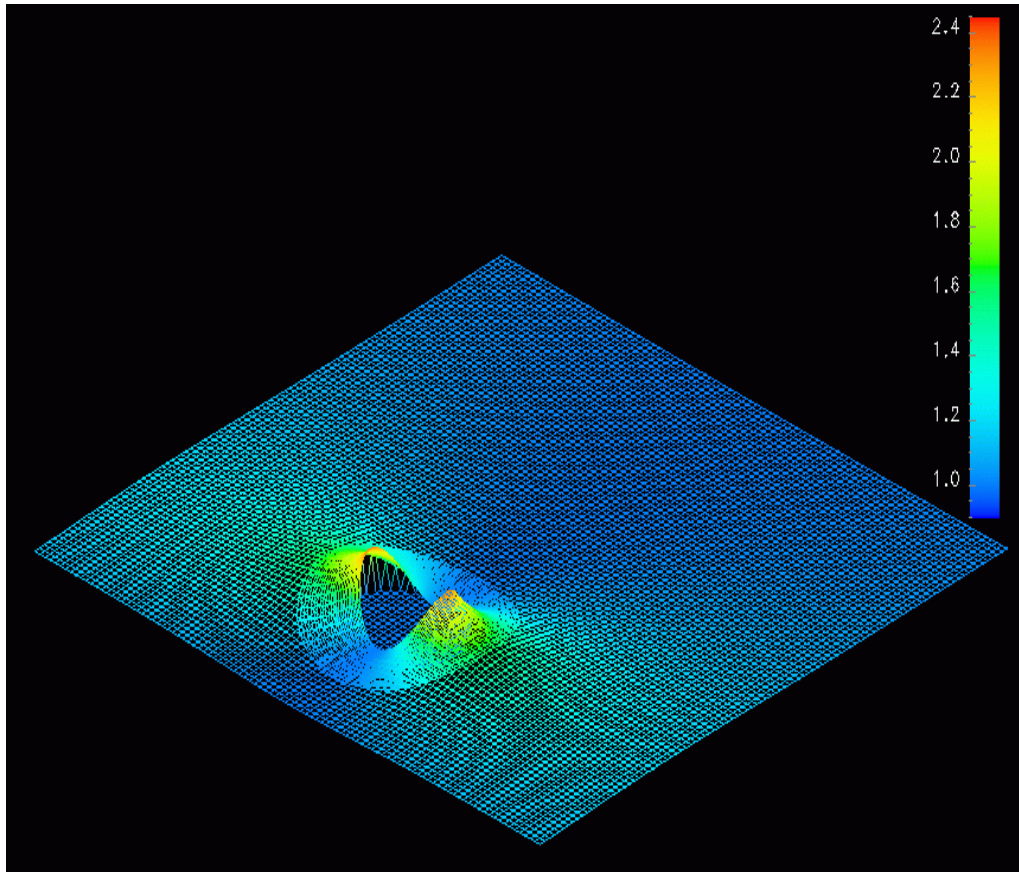
Figure 8.17: The $x = 0$ plane for g_{yy} at the initial time in a simulation boosting a nonrotating Kerr-Schild black hole in the z direction with speed 0.5, described in Figure 8.16.
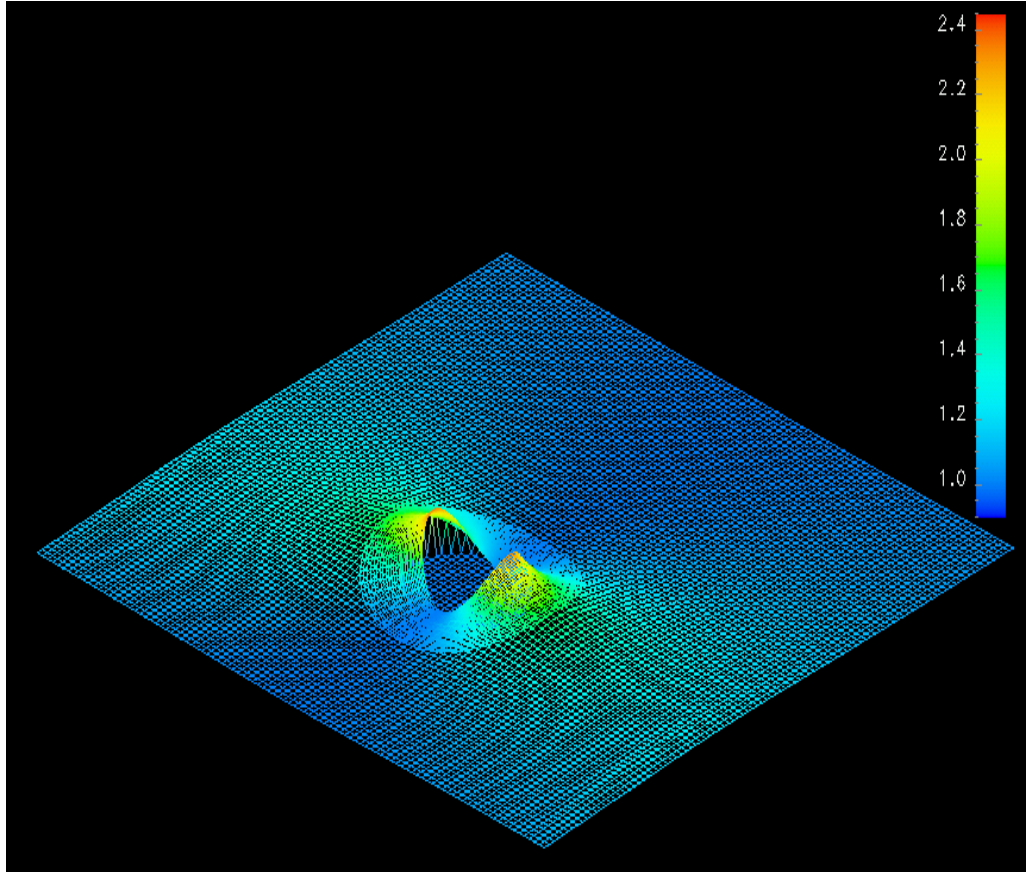
Figure 8.18: The $x = 0$ plane for g_{yy} at time $5M$ in a simulation boosting a nonrotating Kerr-Schild black hole in the z direction with speed 0.5, described in Figure 8.16.
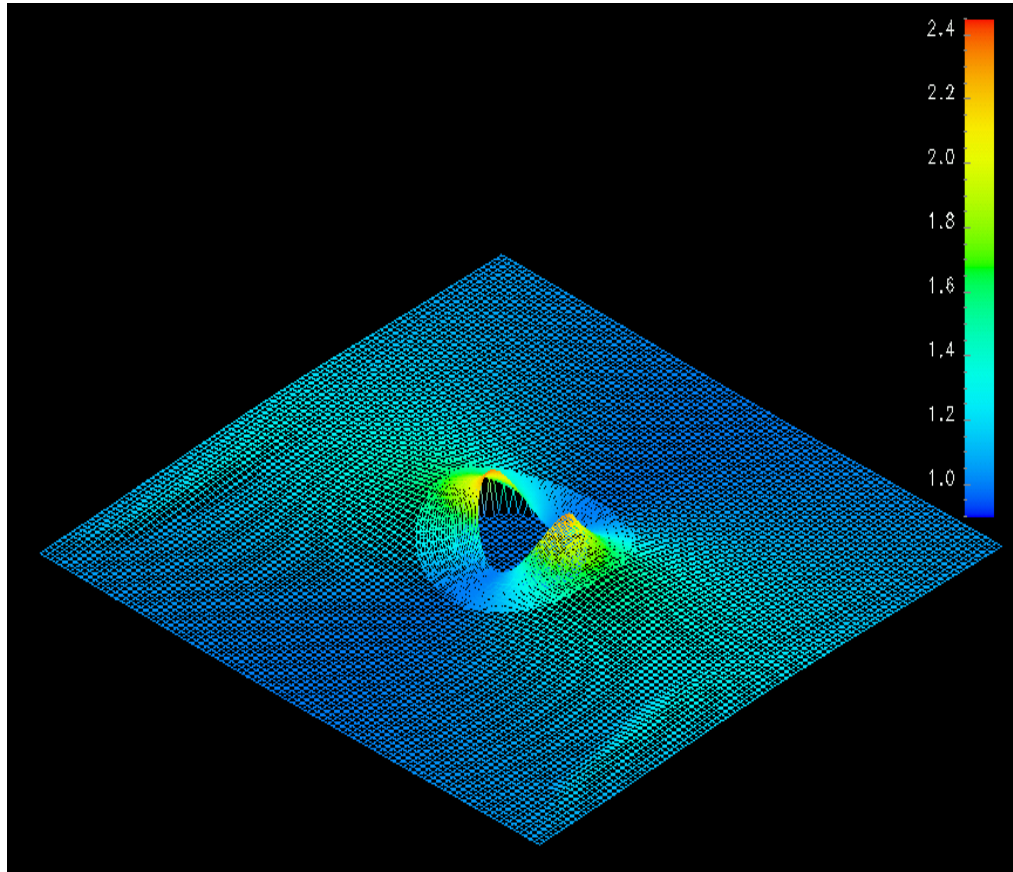
Figure 8.19: The $x = 0$ plane for g_{yy} at time $10M$ in a simulation boosting a nonrotating Kerr-Schild black hole in the z direction with speed 0.5, described in Figure 8.16. The Dirichlet boundary condition and small domain size of the simulation give rise to the boundary errors visible at this point.
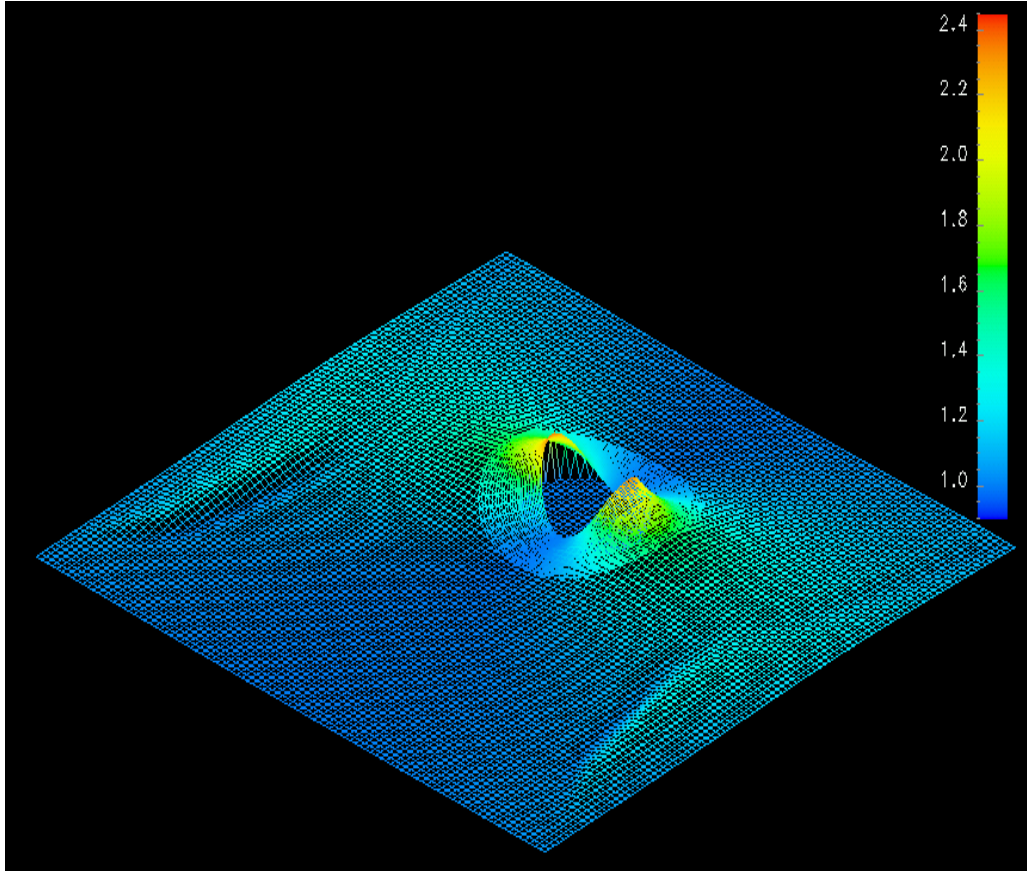
Figure 8.20: The $x = 0$ plane for g_{yy} at time $15M$ in a simulation boosting a nonrotating Kerr-Schild black hole in the z direction with speed 0.5, described in Figure 8.16.
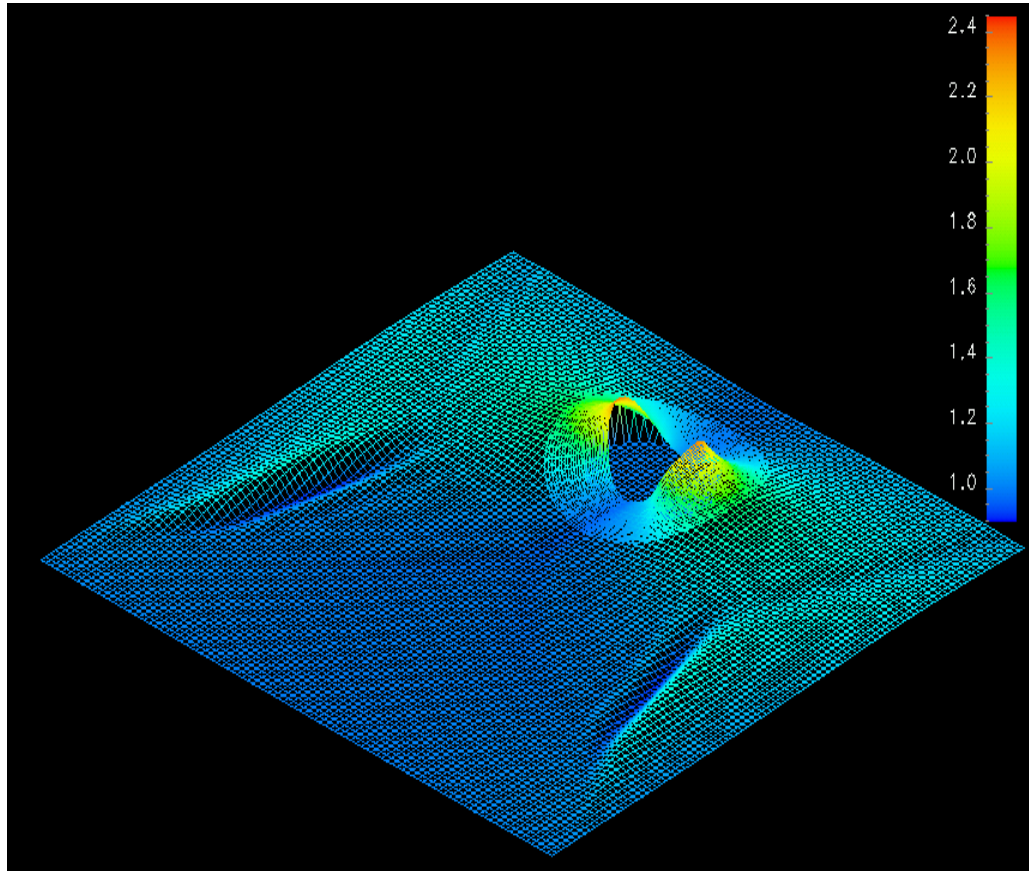
Figure 8.21: The $x = 0$ plane for g_{yy} at time $20M$ in a simulation boosting a nonrotating Kerr-Schild black hole in the z direction with speed 0.5, described in Figure 8.16. While there are clearly boundary problems due to the small domain size of the simulation and the Dirichlet boundary condition, the fields next to the singularity are well-behaved and evidently stable.

Boosted Black Hole
with overlapping grids
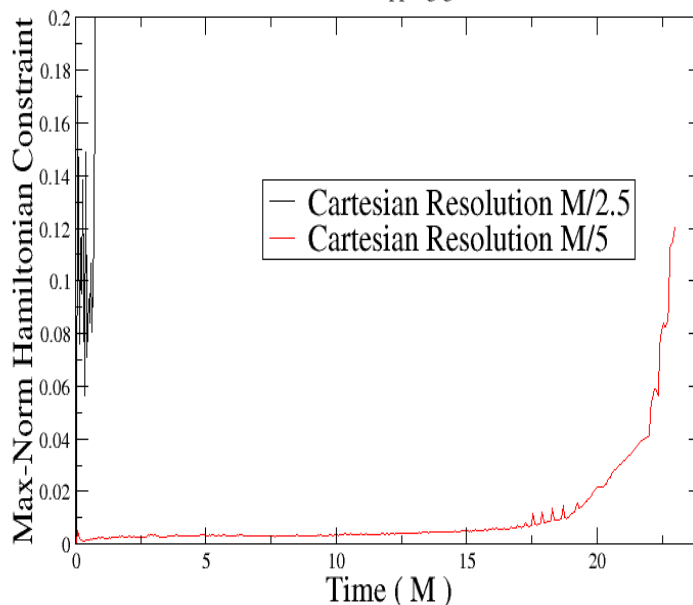
Figure 8.22: The max-norm of the Hamiltonian constraint violation for a nonrotating Kerr-Schild black hole boosted with speed 0.5 in the z direction, performed at two different resolutions. The simulations used both overlapping spheroidal and Cartesian computational grids to ensure a smooth excision surface and avoid extrapolation. The Cartesian computational domain was $[-10M \ldots 10M]$ with resolution of either $M/5$ or $M/2.5$. The Cartesian excision radius was $2.0M$. The spheroidal excision radius was $1.5M$ in the nonboosted direction ($1.3M$ in the boosted direction). The spheroidal domain extended out to a radius of $3.25M$ and used either $(26, 30, 50)$ or $(16, 30, 50)$ zones in the (r, θ, ϕ) direction. $\theta_{\min}$ was 0.6. The hole was placed initially at $z = -5M$ on the Cartesian grid. The lapse was analytic. Interpolation between the three grids was 6th order polynomial. The constraints on all three grids were solved every $0.05M$. The lower resolution case went immediately unstable after only $1M$. The higher resolution case is the same as that described in Figure 8.16. The hole hit the edge of the computational domain at $t = 23M$ (a radial distance of $\sim 1M$ outside the spheroidal grids is necessary for the spheroidal outer boundary interpolation to proceed). The Cartesian boundary adversely affects the solution as the hole approaches the edge of the computational domain, as evident in Figures 8.19–8.21.

154

Chapter 9

Conclusion

Constrained evolution is the principal innovation of this thesis. The generality of the technique enabled its application to various numerical methods and equation formulations. The results presented indicate that by solving *all* the Einstein equations throughout a simulation, definite stability benefits result.

Solving the constraint equations throughout a simulation evolving a black hole spacetime shows promise in controlling the growth of the constraints and improving the lifetime of the simulation. Constrained evolution works especially well for the simplest test cases: simulations in 1-D/spherical symmetry or simulations in full 3-D but with relatively small domains. The many results presented here suggest that constrained evolution alone may not be sufficient to ensure stability of full 3-D simulations on very large domains. Even so, constrained evolution can significantly improve the lifetime of such large domain simulations.

Remarkably stable unconstrained evolutions using the ADM equations modified by constraint subtraction suggest that the specific formulation of the Einstein equations has a significant impact on the stability of a simulation. Since constrained evolution is formulation independent, future work should examine constrained evolution in those formulations which have already demonstrated highly successful un-

constrained results.

In preparation for binary black hole evolutions, several promising numerical techniques were examined in conjunction with constrained evolution: mesh refinement and overlapping computational grids. Constrained evolution proved to be critical for both of these techniques. A host of innovations were presented to achieve constrained evolutions for stationary and boosted black hole spacetimes with smooth 2-sphere excision regions.

The use of publicly available computational toolkits figured prominently in this thesis. By combining independent but robust, parallel toolkits in addressing the demanding tasks of simultaneous elliptic and hyperbolic solves, even across overlapping spheroidal and Cartesian computational grids, constrained evolution becomes a manageable technique in full 3-D simulations. While constrained evolution has already been employed many times in 1-D/spherical symmetry and 2-D/axisymmetry, this thesis demonstrates that the computational demands of constrained evolution in full 3-D can be met successfully.

Appendix A

The Finite Differencing Core

Black hole excision introduces irregular boundaries into the computational domain. Requiring 4th order finite difference stencils only exacerbates the problem. This challenge was addressed by creating a set of 27 general 4th order finite difference stencils that form the finite differencing core of the black hole codes studied in this thesis.

The method used to obtain these finite difference stencils is described here. Several Taylor Series expansions are made around a point in a proposed stencil. For one dimension, either 4 or 5 coefficients are needed for a 4th order stencil (e.g. $f(x + h)$, $f(x + 2h)$, $f(x - h)$, $f(x - 2h)$). In two dimensions, either 23 or 24 coefficients are needed. An over-determined system of equations results from the requirement that all but the sought after derivative in the Taylor Series expansions vanish. The over-determined matrix is reduced to a square matrix by performing a least squares fit of the system. The system is then solved and the customized stencil coefficients are tested for accuracy.

The method of least-squares solution of an over-determined system is summarized here [78] [79]. Consider an over-determined system:

$$A_{ij}x_j = y_i \qquad (A.1)$$

where $i > j$. This system is made into a scalar quantity, S, and then minimized:

$$S = (A_{ij}x_j - y_i)(A_{ik}x_k - y_i) \tag{A.2}$$

$$\frac{\partial S}{\partial x_n} = A_{in}(A_{ik}x_k - y_i) = 0. \tag{A.3}$$

The statement that $A_{in}A_{ik}x_k = A_{in}y_i$ from Eq. (A.3) can be rewritten in vector notation as

$$\mathbf{A^t A x} = \mathbf{A^t y}, \tag{A.4}$$

where $\mathbf{A^t}$ is the transpose of matrix $\mathbf{A}$. This simple relation can be used to turn an over-determined matrix into a square matrix. The method is exact if an exact solution to the system of equations exists; if not, the solution will be a least squares fit.

The finite differencing core consists of 21 stencils built for irregular boundaries and 6 widely used simple stencils, all of which are precisely fourth order. All of the first derivative stencils and the centered second derivative stencil are widely used and have been employed in numerical relativity codes before [80]. The finite differencing core is as follows:

First Derivatives: $\partial_h = \frac{1}{12h}[\cdots] + O(h^4)$

i-4	i-3	i-2	i-1	i	i+1	i+2	i+3	i+4
+3	-16	+36	-48	+25				
	-1	+6	-18	+10	+3			
		+1	-8	0	+8	-1		
			-3	-10	+18	-6	+1	
				-25	+48	-36	+16	-3

Second Derivatives: $\partial_{hh} = \frac{1}{12h^2}[\cdots] + O(h^4)$

i-5	i-4	i-3	i-2	i-1	i	i+1	i+2	i+3	i+4	i+5
-10	+61	-156	+214	-154	+45					
	+1	-6	+14	-4	-15	+10				
			-1	+16	-30	+16	-1			
				+10	-15	-4	+14	-6	+1	
					+45	-154	+214	-156	+61	-10

Mixed Derivatives: $\partial_{h_i h_j} = \frac{1}{72 h_i h_j}[\cdots] + O(h^4)$. There are 17 options.

Option 1:

	j-2	j-1	j	j+1	j+2
i+2	0	+2	+3	-6	+1
i+1	+2	-24	-12	+40	-6
i	+3	-12	+18	-12	+3
i-1	-6	+40	-12	-24	+2
i-2	+1	-6	+3	+2	0

Option 2:

	j-1	j	j+1	j+2	j+3
i+3	0	-11	+18	-9	+2
i+2	+3	+54	-90	+42	-9
i+1	-18	-126	+216	-90	+18
i	+9	+74	-126	+54	-11
i-1	+6	+9	-18	+3	0

Option 3:

	j-3	j-2	j-1	j	j+1
i+3	-2	+9	-18	+11	0
i+2	+9	-42	+90	-54	-3
i+1	-18	+90	-216	+126	+18
i	+11	-54	+126	-74	-9
i-1	0	-3	+18	-9	-6

Option 4:

	j-3	j-2	j-1	j	j+1
i+1	0	+3	-18	+9	+6
i	-11	+54	-126	+74	+9
i-1	+18	-90	+216	-126	-18
i-2	-9	+42	-90	+54	+3
i-3	+2	-9	+18	-11	0

Option 5:

	j-1	j	j+1	j+2	j+3
i+1	-6	-9	+18	-3	0
i	-9	-74	+126	-54	+11
i-1	+18	+126	-216	+90	-18
i-2	-3	-54	+90	-42	+9
i-3	0	+11	-18	+9	-2

Option 6:

	j	j+1	j+2	j+3	j+4
i+4	0	+78	-171	+126	-33
i+3	-50	-216	+612	-472	+126
i+2	+225	+36	-702	+612	-171
i+1	-450	+552	+36	-216	+78
i	+275	-450	+225	-50	0

Option 7:

	j-4	j-3	j-2	j-1	j
i+4	+33	-126	+171	-78	0
i+3	-126	+472	-612	+216	+50
i+2	+171	-612	+702	-36	-225
i+1	-78	+216	-36	-552	+450
i	0	+50	-225	+450	-275

Option 8:

	j-4	j-3	j-2	j-1	j
i	0	-50	+225	-450	+275
i-1	+78	-216	+36	+552	-450
i-2	-171	+612	-702	+36	+225
i-3	+126	-472	+612	-216	-50
i-4	-33	+126	-171	+78	0

Option 9:

	j	j+1	j+2	j+3	j+4
i	-275	+450	-225	+50	0
i-1	+450	-552	-36	+216	-78
i-2	-225	-36	+702	-612	+171
i-3	+50	+216	-612	+472	-126
i-4	0	-78	+171	-126	+33

Option 10:

	j-2	j-1	j	j+1	j+2
i+4	0	+6	+9	-18	+3
i+3	+2	-40	-36	+88	-14
i+2	-9	+108	+54	-180	+27
i+1	+18	-168	-36	+216	-30
i	-11	+94	+9	-106	+14

Option 11:

	j-4	j-3	j-2	j-1	j
i+2	-3	+14	-27	+30	-14
i+1	+18	-88	+180	-216	+106
i	-9	+36	-54	+36	-9
i-1	-6	+40	-108	+168	-94
i-2	0	-2	+9	-18	+11

Option 12:

	j-2	j-1	j	j+1	j+2
i	+11	-94	-9	+106	-14
i-1	-18	+168	+36	-216	+30
i-2	+9	-108	-54	+180	-27
i-3	-2	+40	+36	-88	+14
i-4	0	-6	-9	+18	-3

Option 13:

	j	j+1	j+2	j+3	j+4
i+2	+14	-30	+27	-14	+3
i+1	-106	+216	-180	+88	-18
i	+9	-36	+54	-36	+9
i-1	+94	-168	+108	-40	+6
i-2	-11	+18	-9	+2	0

Option 14:

	j-2	j-1	j	j+1	j+2
i+3	0	-2	-3	+6	-1
i+2	-1	+16	+12	-32	+5
i+1	+6	-60	-18	+84	-12
i	-3	+32	+12	-48	+7
i-1	-2	+14	-3	-10	+1

Option 15:

	j-3	j-2	j-1	j	j+1
i+2	+1	-5	+12	-7	-1
i+1	-6	+32	-84	+48	+10
i	+3	-12	+18	-12	+3
i-1	+2	-16	+60	-32	-14
i-2	0	+1	-6	+3	+2

Option 16:

	j-2	j-1	j	j+1	j+2
i+1	+2	-14	+3	+10	-1
i	+3	-32	-12	+48	-7
i-1	-6	+60	+18	-84	+12
i-2	+1	-16	-12	+32	-5
i-3	0	+2	+3	-6	+1

Option 17:

	j-1	j	j+1	j+2	j+3
i+2	+1	+7	-12	+5	-1
i+1	-10	-48	+84	-32	+6
i	-3	+12	-18	+12	-3
i-1	+14	+32	-60	+16	-2
i-2	-2	-3	+6	-1	0

Appendix B

Kerr-Schild Data for

Non-Spinning Holes

The Kerr-Schild data for an isolated non-spinning black hole with mass M are provided here in spherical and Cartesian coordinates. Evolving this data served as a test case in this thesis for examining the stability properties of constrained evolution, mesh refinement, and overlapping grids.

In spherical coordinates:

$$
g_{ij} = \begin{bmatrix} 1 + \frac{2M}{r} & 0 & 0 \\ 0 & r^2 & 0 \\ 0 & 0 & r^2 \sin^2 \theta \end{bmatrix} \tag{B.1}
$$

$$
K_{ij} = \begin{bmatrix} -\frac{2M}{r^3} \sqrt{\frac{r}{r+2M}} \, (r + M) & 0 & 0 \\ 0 & 2M \sqrt{\frac{r}{r+2M}} & 0 \\ 0 & 0 & 2M \sqrt{\frac{r}{r+2M}} \sin^2 \theta \end{bmatrix} \tag{B.2}
$$

$$
\alpha = \sqrt{\frac{r}{r + 2M}} \tag{B.3}
$$

$$\beta^i = \begin{bmatrix} \frac{2M}{r+2M} & 0 & 0 \end{bmatrix} \tag{B.4}$$

In Cartesian coordinates (using $r = \sqrt{x^2 + y^2 + z^2}$):

$$g_{ij} = \begin{bmatrix} 1 + \frac{2Mx^2}{r^3} & \frac{2Mxy}{r^3} & \frac{2Mxz}{r^3} \\ \frac{2Mxy}{r^3} & 1 + \frac{2My^2}{r^3} & \frac{2Myz}{r^3} \\ \frac{2Mxz}{r^3} & \frac{2Myz}{r^3} & 1 + \frac{2Mz^2}{r^3} \end{bmatrix} \tag{B.5}$$

Using $Q = -2\, M r^{-4} \frac{1}{\sqrt{1 + 2\frac{M}{r}}}$,

$$K_{ij} = \begin{bmatrix} \left[\left(\frac{M}{r} + 2 \right) x^2 - r^2 \right] Q & \left(\frac{M}{r} + 2 \right) xyQ & \left(\frac{M}{r} + 2 \right) xzQ \\ \left(\frac{M}{r} + 2 \right) xyQ & \left[\left(\frac{M}{r} + 2 \right) y^2 - r^2 \right] Q & \left(\frac{M}{r} + 2 \right) yzQ \\ \left(\frac{M}{r} + 2 \right) xzQ & \left(\frac{M}{r} + 2 \right) yzQ & \left[\left(\frac{M}{r} + 2 \right) z^2 - r^2 \right] Q \end{bmatrix} \tag{B.6}$$

$$\alpha = \sqrt{\frac{r}{r + 2M}} \tag{B.7}$$

$$\beta_i = \begin{bmatrix} 2\frac{Mx}{r^2} & 2\frac{My}{r^2} & 2\frac{Mz}{r^2} \end{bmatrix} \tag{B.8}$$

Bibliography

[1] Steven Weinberg. *Gravitation and Cosmology*, pages 140–142. John Wiley & Sons, 1972.

[2] L. L. Smarr and J. W. York. Radiation gauge in general relativity. *Physical Review D*, 17(8):1945–1956, 1978.

[3] J. W. York and T. Piran. The initial value problem and beyond. In Richard A. Matzner and L.C. Shepley, editors, *Spacetime and geometry: the Alfred Schild lectures*, pages 147–176. University of Texas Press, 1982.

[4] C. R. Evans and J. F. Hawley. Simulation of magnetohydrodynamic flows: A constrained transport method. *Astrophysical Journal*, 332:659–677, 1988.

[5] David L. Meier. Constrained transport algorithms for numerical relativity. I. Development of a finite difference scheme. *Astrophysical Journal*, 595:980–991, 2003.

[6] R. Arnowitt, S. Deser, and C. W. Misner. The dynamics of general relativity. In Louis Witten, editor, *Gravitation – An Introduction to Current Research*, pages 227–265. Wiley, New York, 1962.

[7] J. Hadamard. Sur les problemes aux derivees partiellies et leur signification physique. *Princeton University Bulletin*, 13(4):49–52, 1902.

[8] Heinz-Otto Kreiss and Hedwig Ulmer Busenhard. *Time-Dependent Partial Differential Equations and Their Numerical Solution.* Birkhäuser Verlag, 2001.

[9] Heinz Otto Kreiss and Omar E. Ortiz. Some mathematical and numerical questions connected with first and second order time dependent systems of partial differential equations. *Lecture Notes in Physics*, 604:359–370, 2002.

[10] Bernard Kelly, Pablo Laguna, Keith Lockitch, Jorge Pullin, Erik Schnetter, Deirdre Shoemaker, and Manuel Tiglio. Cure for unstable numerical evolutions of single black holes: Adjusting the standard ADM equations in the spherically symmetric case. *Physical Review D*, 64:084013, 2001.

[11] B. Gustaffson, H. O. Kreiss, and J. Oliger. *Time-Dependent Problems and Difference Methods*, pages 218–221. John Wiley & Sons, 1995.

[12] S. Frittelli and O. A. Reula. First-order symmetric hyperbolic Einstein equations with arbitrary fixed gauge. *Physical Review Letters*, 76:4667–4670, 1996.

[13] Simon David Hern. *Numerical Relativity and Inhomogeneous Cosmologies.* PhD thesis, University of Cambridge, 1999. arXiv:gr-qc/0004036.

[14] R. Kerr and A. Schild. Some algebraically degenerate solutions of Einstein's gravitational field equations. In *Applications of Nonlinear Partial Differential Equations in Mathematical Physics*, Symposium in Applied Mathematics Proceedings, v. 17., pages 199–209. American Mathematical Society, 1965. Symposium held in New York City, 1964.

[15] N. Ó. Murchadha and J. W. York, Jr. Initial-value problem of general relativity. *Physical Review D*, 10:428–436,437–446, 1974.

[16] E. Gourgoulhon, P. Grandclement, and S. Bonazzola. Binary black holes in circular orbits. *Physical Review D*, 65:044020, 2002.

[17] Erin Bonning, Pedro Marronetti, David Neilsen, and Richard A. Matzner. Physics and initial data for multiple black hole spacetimes. *Physical Review D*, 68(4):044019, 2003.

[18] Pedro Marronetti and Richard A. Matzner. Solving the initial value problem of two black holes. *Physical Review Letters*, 85(26):5500–5503, 2000.

[19] R. Courant, K. O. Friedrichs, and H. Lewy. Über die partiellen differenzengleichungen der mathematischen physik. *Mathematische Annalen*, 100:32–74, 1928. English translation in IBM *Journal of Research and Development* 11 (1967).

[20] Vidar Thomée. A short history of numerical analysis of partial differential equations. *Journal of Computational and Applied Mathematics*, 128:1–54, Mar 2001.

[21] William H. Press, Brian P. Flannery, Saul A. Teukolsky, and William T. Vetterling. *Numerical Recipes*, pages 623–635. Cambridge University Press, 1989.

[22] P. N. Brown and A. C. Hindmarsh. PVODE, an ODE solver for parallel computers. *International Journal of High Performance Computing Applications*, 13(4):354–365, 1999.

[23] George D. Byrne and Alan C. Hindmarsh. User documentation for PVODE, an ODE solver for parallel computers. Technical Report UCRL-ID-130884, Center for Applied Scientific Computing, May 1998.

[24] Alan Hindmarsh, Radu Serban, and Carol Woodward. SUNDIALS home page. http://www.llnl.gov/CASC/sundials, 2003.

[25] Lee W. Johnson and R. Dean Riess. *Numerical Analysis*, pages 304–326. Addison-Wesley Publishing Company, 1977.

[26] Lee W. Johnson and R. Dean Riess. *Numerical Analysis*, pages 158–162. Addison-Wesley Publishing Company, 1977.

[27] Henk A. Van der Vorst. Iterative methods for linear systems and implementation on parallel computers. In Raymond H. Chan, Tony F. Chan, and Gene H. Golub, editors, *Iterative Methods in Scientific Computing*, pages 1–44. Springer, 1997.

[28] Gábor Tóth. The $\nabla \cdot \mathbf{B} = 0$ constraint in shock-capturing magnetohydrodynamics codes. *Journal of Computational Physics*, 161:605–652, 2000.

[29] Satish Balay, Kris Buschelman, William D. Gropp, Dinesh Kaushik, Matt Knepley, Lois Curfman McInnes, Barry F. Smith, and Hong Zhang. PETSc home page. http://www.mcs.anl.gov/petsc, 2001.

[30] Satish Balay, Kris Buschelman, William D. Gropp, Dinesh Kaushik, Matt Knepley, Lois Curfman McInnes, Barry F. Smith, and Hong Zhang. PETSc users manual. Technical Report ANL-95/11 - Revision 2.1.5, Argonne National Laboratory, 2002.

[31] Satish Balay, William D. Gropp, Lois Curfman McInnes, and Barry F. Smith. Efficient management of parallelism in object oriented numerical software libraries. In E. Arge, A. M. Bruaset, and H. P. Langtangen, editors, *Modern Software Tools in Scientific Computing*, pages 163–202. Birkhauser Press, 1997.

[32] Allan G. Taylor and Alan C. Hindmarsh. User documentation for KINSOL, a nonlinear solver for sequential and parallel computers. Technical Report UCRL-ID-131185, Center for Applied Scientific Computing, July 1998.

[33] Richard Hornung, Scott Kohn, Noah Elliott, Steve Smith, Andy Wissink, Brian Gunney, and David Hysom. SAMRAI home page. http://www.llnl.gov/CASC/SAMRAI, 2002.

[34] Richard Hornung and Scott Kohn. Managing application complexity in the SAMRAI object-oriented framework. *Concurrency and Computation: Practice and Experience*, 14:347–368, 2002. Also LLNL technical report UCRL–JC–141749.

[35] A. M. Wissink, R. D. Hornung, S. R. Kohn, S. G. Smith, and N. Elliott. Large-scale structured amr calculations using the SAMRAI framework. In *Proceedings of SC '01 Conference on High Performance Networking and Computing*, Denver, Colorado, November 10–16 2001. Also LLNL technical report UCRL–JC–144755.

[36] Mark Galassi, Jim Davies, James Theiler, Brian Gough, Gerard Jungman, Michael Booth, and Fabrice Rossi. *GNU Scientific Library Reference Manual.* Network Theory Limited, 2003.

[37] Mark Galassi, Jim Davies, James Theiler, Brian Gough, Gerard Jungman, Michael Booth, and Fabrice Rossi. The GNU Scientific Library development page. http://sources.redhat.com/gsl/, 2003.

[38] The National Center for Supercomputing Applications University of Illinois at Urbana-Champaign. HDF5 home page. http://hdf.ncsa.uiuc.edu/HDF5/, 2003.

[39] Mathematics and Computer Science Division Argonne National Laboratory. The MPI standard home page. http://www-unix.mcs.anl.gov/mpi/, 2003.

[40] Applied Numerical Algorithms Group Lawrence Berkeley National Laboratory. ChomboVis home page. http://seesar.lbl.gov/anag/chombo/chombovis.html, 2003.

[41] Waterloo Maple Inc. Maple home page. http://www.maplesoft.com/.

[42] Jonathan Thornburg. Coordinate and boundary conditions for the general relativistic initial data problem. *Classical and Quantum Gravity*, 4:1119–1131, 1987.

[43] Steve Brandt, Randall Correll, Roberto Gomez, Mijan Huq, Pablo Laguna, Luis Lehner, Pedro Marronetti, Richard A. Matzner, David Neilsen, Jorge Pullin, Erik Schnetter, Deirdre Shoemaker, and Jeffrey Winicour. Grazing collisions of black holes via the excision of singularities. *Physical Review Letters*, 85:5496–5499, 2000.

[44] Mijan Huq. *Apparent Horizon Location in Numerical Spacetimes*. PhD thesis, The University of Texas at Austin, 1996.

[45] Mijan F. Huq, Matthew W. Choptuik, and Richard A. Matzner. Locating boosted Kerr and Schwarzschild apparent horizons. *Physical Review D*, 66:084024, 2002.

[46] David Garrison. *Testing Binary Black Hole Codes in Strong Field Regimes*. PhD thesis, Pennsylvania State University, 2002.

[47] Patrick Knupp and Kambiz Salari. *Verification of Computer Codes in Computational Science and Engineering*. Discrete Mathematics and its Applications. Chapman & Hall/CRC, 2003.

[48] Gen Yoneda and Hisa aki Shinkai. Advantages of a modified ADM formulation: Constraint propagation analysis of the Baumgarte-Shapiro-Shibata-Nakamura system. *Physical Review D*, 66:124003, 2002.

[49] Gioel Calabrese. A remedy for constraint growth in numerical relativity. arXiv:gr-qc/0404036, 2004.

[50] Mark A. Scheel, Lawrence E. Kidder, Lee Lindblom, Harald P. Pfeiffer, and

Saul A. Teukolsky. Toward stable 3d numerical evolutions of black-hole space-times. *Physical Review D*, 66:124005, 2002.

[51] Hwei-Jang Yo, Thomas W. Baumgarte, and Stuart L. Shapiro. Improved numerical stability of stationary black hole evolution calculations. *Physical Review D*, 66:084026, 2002.

[52] Richard A. Stark and Tsvi Piran. Gravitational-wave emission from rotating gravitational collapse. *Physical Review Letters*, 55:891–894, 1985. Only the Hamiltonian constraint is solved in this work.

[53] Andrew M. Abrahams and Charles R. Evans. Trapping a geon: Black hole formation by an imploding gravitational wave. *Physical Review D*, 46:R4117–R4121, 1992. Only the Hamiltonian constraint is solved in this work.

[54] Charles R. Evans. Calculating axisymmetric gravitational collapse. In Joan Centrella, editor, *Dynamical Spacetimes and Numerical Relativity*, pages 3–39. Cambridge University Press, 1986.

[55] Charles R. Evans. Enforcing the momentum constraints during axisymmetric spacelike simulations. In Charles R. Evans, Lee S. Finn, and David W. Hobill, editors, *Frontiers in Numerical Relativity*, pages 194–205. Cambridge University Press, 1989.

[56] Andrew M. Abrahams and Charles R. Evans. Critical behavior and scaling in vacuum axisymmetric gravitational collapse. *Physical Review Letters*, 70:2980–2983, 1993.

[57] Andrew M. Abrahams, Gregory B. Cook, Stuart L. Shapiro, and Saul A. Teukolsky. Solving Einstein's equations for rotating spacetimes: Evolution of relativistic star clusters. *Physical Review D*, 49:5153–5164, 1994.

[58] Frans Pretorius. *Numerical Simulations of Gravitational Collapse*. PhD thesis, The University of British Columbia, 2002.

[59] Matthew W. Choptuik, Eric W. Hirschmann, Steven L. Liebling, and Frans Pretorius. An axisymmetric gravitational collapse code. *Classical and Quantum Gravity*, 20(9):1857–1878, 2003.

[60] Matthew Choptuik. Personal communication, 2003.

[61] Erik Schnetter. *Gauge fixing for the simulation of black hole spacetimes*. PhD thesis, Universität zu Tübingen, 2003.

[62] S. Bonazzola, E. Gourgoulhon, P. Grandclement, and J. Novak. A constrained scheme for Einstein equations based on Dirac gauge and spherical coordinates. arXiv:gr-qc/0307082, 2003.

[63] Gioel Calabrese and David Neilsen. Spherical excision for moving black holes and summation by parts for axisymmetric systems. *Physical Review D*, 69:044020, 2004.

[64] M. J. Berger and J. Oliger. Adaptive mesh refinement for hyperbolic partial differential equations. *Journal of Computational Physics*, 53:484–512, 1984.

[65] B. Brügmann. Adaptive mesh and geodesically sliced Schwarzschild spacetime in $3+1$ dimensions. *Physical Review D*, 54:7361–7372, 1996.

[66] Bernd Brügmann, Wolfgang Tichy, and Nina Jansen. Numerical simulation of orbiting black holes. arXiv:gr-qc/0312112, 2003.

[67] The Cactus home page. http://www.cactuscode.org.

[68] Erik Schnetter, Scott H. Hawley, and Ian Hawke. Evolutions in 3d numerical relativity using fixed mesh refinement. *Classical and Quantum Gravity*, 21(6):1465–1488, 2004.

[69] Breno Imbiriba, John Baker, Dae-Il Choi, Joan Centrella, David Fiske, J. David Brown, James R. van Meter, and Kevin Olson. Evolving a puncture black hole with fixed mesh refinement. arXiv:gr-qc/0403048, 2004.

[70] P. MacNeice, K. Olson, C. Mobarry, R. de Fainchtein, and C. Packer. PARAMESH: A parallel adaptive mesh refinement community toolkit. *Computer Physics Communications*, 126:330–354, 2000.

[71] Dae-Il Choi, J. David Brown, Breno Imbiriba, Joan Centrella, and Peter Mac-Neice. Interface conditions for wave propagation through mesh refinement boundaries. *Journal of Computational Physics*, 193:398–425, 2004.

[72] G. Calabrese, L. Lehner, D. Neilsen, J. Pullin, O. Reula, O. Sarbach, and M. Tiglio. Novel finite-differencing techniques for numerical relativity: application to black-hole excision. *Classical and Quantum Gravity*, 20(20):L245–L252, 2003.

[73] Nigel T. Bishop, Roberto Gómez, Paulo R. Holvorcem, Richard A. Matzner, Philippos Papadopoulos, and Jeffrey Winicour. Cauchy-characteristic matching: A new approach to radiation boundary conditions. *Physical Review Letters*, 76(23):4303–4306, 1996.

[74] R. Gómez, L. Lehner, P. Papadopoulos, and J. Winicour. The eth formalism in numerical relativity. *Classical and Quantum Gravity*, 14(4):977–990, 1997.

[75] Jonathan Thornburg. Black hole excision with multiple grid patches. arXiv:gr-qc/0404059, 2004.

[76] William Henshaw, Daniel J. Quinlan, and David L. Brown. Overture home page. http://www.llnl.gov/CASC/Overture/, 2002.

[77] Richard Matzner. Personal communication, 2004.

[78] Lee W. Johnson and R. Dean Riess. *Numerical Analysis*, pages 61–65. Addison-Wesley Publishing Company, 1977.

[79] Ross L. Spencer. Personal communication, 1998.

[80] Jonathan Thornburg. A $3+1$ computational scheme for dynamic spherically symmetric black hole spacetimes – II: Time evolution. arXiv:gr-qc/9906022, 1999.

Vita

Matthew William Anderson was born in West Valley City, Utah on March 17, 1976, the son of William Stewart Anderson and Judy King Anderson. After completing his work at Granger High School, West Valley, Utah, in 1994, he entered Brigham Young University in Provo, Utah. He graduated with a Bachelor of Science in Physics in August 1999. In September 1999 he entered the Graduate School at the University of Texas.

Permanent Address: 3807 West 3240 South

West Valley City, UT 84120

This dissertation was typeset with LaTeX 2_ε by the author.